# NASA TECHNICAL NOTE

COMPARISONS OF
TURBULENT-BOUNDARY-LAYER MEASUREMENTS
AT MACH NUMBER 19.5 WITH THEORY
AND AN ASSESSMENT OF PROBE ERRORS

*by Ivan E. Beckwith, William D. Harvey,
and Frank L. Clark*

*Langley Research Center
Hampton, Va. 23365*

| 1. Report No. NASA TN D-6192 | 2. Government Accession No. | 3. Recipient's Catalog No. |
|---|---|---|
| 4. Title and Subtitle COMPARISONS OF TURBULENT-BOUNDARY-LAYER MEASUREMENTS AT MACH NUMBER 19.5 WITH THEORY AND AN ASSESSMENT OF PROBE ERRORS | | 5. Report Date June 1971 |
| | | 6. Performing Organization Code |
| 7. Author(s) Ivan E. Beckwith, William D. Harvey, and Frank L. Clark | | 8. Performing Organization Report No. L-7020 |
| | | 10. Work Unit No. 124-07-18-03 |
| 9. Performing Organization Name and Address NASA Langley Research Center Hampton, Va. 23365 | | 11. Contract or Grant No. |
| | | 13. Type of Report and Period Covered Technical Note |
| 12. Sponsoring Agency Name and Address National Aeronautics and Space Administration Washington, D.C. 20546 | | 14. Sponsoring Agency Code |

| 15. Supplementary Notes |
|---|
| With appendix A by Ivan E. Beckwith, William D. Harvey, and Christine M. Darden and appendix B by William D. Harvey, Lemuel E. Forrest, and Frank L. Clark |

16. Abstract

Measurements of total temperature and pitot pressure have been made across the boundary layer on the test-section wall of an axisymmetric contoured nozzle at Mach 19.5 in nitrogen. The ratio of wall temperature to stagnation temperature was about 0.17. The Reynolds number based on momentum thickness varied from about 3500 to 4800 and the boundary-layer thickness varied from 8.6 to 11.2 centimeters (3.4 to 4.4 in.). A general review and assessment of probe errors is included. Mach number, velocity, and temperature profiles through the boundary layer are compared with previous data and with predictions from finite-difference procedures for calculating compressible turbulent and laminar boundary layers. These comparisons indicated that the boundary layer on the test-section wall was turbulent or transitional, whereas in the throat region of the nozzle the boundary layer may have been laminar for the present test conditions. The analysis includes estimates of skin friction, heat transfer, velocity fluctuations through the boundary layer, and the exponent in the power-law velocity profile.

| 17. Key Words (Suggested by Author(s)) Turbulent boundary layer Nozzle wall Probe errors Turbulent theory | | 18. Distribution Statement Unclassified – Unlimited | | |
|---|---|---|---|---|
| 19. Security Classif. (of this report) Unclassified | 20. Security Classif. (of this page) Unclassified | | 21. No. of Pages 90 | 22. Price* $3.00 |

# COMPARISONS OF TURBULENT-BOUNDARY-LAYER MEASUREMENTS

## AT MACH NUMBER 19.5 WITH THEORY AND AN

## ASSESSMENT OF PROBE ERRORS

By Ivan E. Beckwith, William D. Harvey, and Frank L. Clark
Langley Research Center

## SUMMARY

Measurements of total temperature and pitot pressure have been made across the boundary layer on the wall of an axisymmetric contoured nozzle. Data were obtained at one station near the exit of the nozzle where the nominal stream Mach number was 19.5. The test gas was nitrogen and the ratio of wall temperature to settling-chamber temperature was about 0.17. The Reynolds numbers based on momentum thickness varied from about 3500 to 4800. The corresponding boundary-layer thicknesses were 11.2 to 8.6 centimeters (4.4 and 3.4 in.).

The relatively low Reynolds numbers and high temperatures in the present tests necessitated large corrections to pressure and temperature measurements. A bare-wire thermocouple probe was used to obtain the total-temperature data which have been corrected for heat conduction and radiation losses. The pitot-pressure measurements have been corrected for viscous and rarefaction effects based on data obtained during the present and previous investigations. Static-pressure measurements in the boundary layer were corrected for viscous interaction effects.

Comparisons have been made of the resulting Mach number, velocity, and temperature profiles through the boundary layer with previous data and with predictions from finite-difference procedures for calculating compressible turbulent boundary layers. The agreement between predictions and the present data indicated that turbulent Prandtl numbers may be considerably less than unity and that the boundary layer in the throat region of the nozzle may have been laminar for the present test conditions.

Values for the exponent in the power-law velocity profile and estimated values of viscous sublayer thicknesses from the present data are compared with values from previous data. Estimates of skin friction and heat transfer from the slopes of the profiles at the wall have been made and compared with predictions. Static-pressure measurements across the boundary layer indicated that the pressure increases as the wall is approached. Estimates of root-mean-square velocity fluctuations through the boundary layer from a simple mixing-length relation are compared with values obtained from the normal momentum equation and the static-pressure variation across the boundary layer.

# INTRODUCTION

There is increasing interest in cold-wall turbulent-boundary-layer flows at hypersonic speeds because of their occurrence on high performance vehicles. Theories available for calculation of turbulent boundary layers depend on empirical relations between the mean and fluctuating flow. For hypersonic flow these relations may be altered by the effects of density and pressure fluctuations. Advancements in the theoretical treatment of incompressible turbulent boundary layers were reported in reference 1. Several numerical methods, developed primarily for calculation of incompressible turbulent boundary layers, have been extended to compressible flows (see, for example, refs. 2 to 4). A recent method (ref. 5) provides acceptable predictions of nonequilibrium and hypersonic boundary layers with cold walls and with blowing for a few investigations where experimental data were available. In a review of prediction methods for compressible turbulent boundary layers (ref. 6) the author concluded that finite-difference procedures offer the greatest potential for future uses. However, development of these methods and extension of their range of applicability requires detailed experimental measurements of both mean and fluctuating flow properties for a wide range of conditions.

The lack of reliable and detailed data for compressible boundary layers has led to the development of transformation methods such as those presented in references 7 and 8. These methods transform a given compressible-flow problem to a corresponding incompressible-flow problem, where the data are more accurate and plentiful. Experimental measurements of both pitot pressures and stagnation temperatures in compressible boundary layers are required to assess the accuracy and range of applicability of the transformations.

Experimental data for hypersonic turbulent boundary layers are available in references 9 to 29. References 9 to 11 are for nearly adiabatic wall conditions. Data for conditions of large heat transfer with ratios of wall temperature to settling-chamber temperature $T_W/T_O < 0.4$ are reported in references 12 to 19. Detailed profile data (including measured total temperatures) for large heat-transfer conditions are available in references 12 to 16. Detailed profile data for $0.4 < T_W/T_O < 0.5$ are also available in references 21, 23, 24, and 25.

Experimental studies of the boundary layer on the walls of a hypersonic nozzle are useful not only for direct applications to nozzle flow and nozzle design problems but also in the assessment and development of theoretical methods. In particular, these studies are of interest where upstream effects may be present (ref. 5). Also, since the boundary layers on nozzle walls are generally much thicker than on typical wind-tunnel models, more accurate and detailed measurements can be obtained in the wall boundary layer than

on models at comparable stream conditions. For Mach numbers greater than about 12, the boundary layers on wind-tunnel models will usually be laminar, whereas the nozzle-wall boundary layers will often be turbulent because of the much larger momentum thickness Reynolds numbers on the nozzle wall.

The results reported herein are based on measurements of pitot and static pressure and total temperature in the turbulent boundary layer on the wall of a contoured nozzle at a nominal stream Mach number of 19.5 with large heat-transfer rates to the wall $\left(T_W/T_O \approx 0.2\right)$. The boundary layers were about 10.2 centimeters (4 in.) thick and the data were obtained with test duration times on the order of 2 hours. Wall skin friction was inferred from the slope of the Mach number profiles at the wall. Surface heat transfer was estimated from the slope of the total-temperature profile at the surface. No direct measurements of wall skin friction or heat transfer were made.

Comparisons are made of the present test results with previous data at lower Mach numbers in air and nitrogen and with data in helium for Mach numbers up to 37. The present test data are also compared with results from several theoretical solutions by the finite-difference method of reference 5. By this means, the possible effects of laminarization and turbulent Prandtl number have been investigated. Some preliminary results from the present investigation were compared with theoretical predictions in reference 5. For the final results presented herein, the pitot pressure data have been corrected for viscous and rarefaction effects, the corrections for heat conduction and radiation losses from the temperature probe have been improved, and the free-stream conditions have been modified slightly due to new measurements of static pressure. Some comparisons between the preliminary data as presented in reference 5 and the final corrected data are included in this report. Complete tabulations of the original uncorrected data and the final corrected data are also given in the present report.

## SYMBOLS

| A | constant in static-pressure distribution, equation (1) |
|---|---|
| $A^*$ | constant in equation (11), 26 except for wall blowing cases |
| A, B, C | functions of time in relation for wire temperature, equation (A2) |
| a | speed of sound |
| D | exponent in relation between $N$, $N_{Re,\theta}$, and $T_W/T_O$ |

$\overline{c}$      specific heat of wire

$c_f$      local skin friction coefficient, $\tau_w \Big/ \left(\frac{1}{2} \rho_e u_e^2\right)$

$c_p$      specific heat at constant pressure, generally assumed constant except in determination of $k_t$ from $N_{Pr,t}$

$d$      diameter of wire

$E$      voltage drop over specified length of wire

$e$      voltage drop per unit length

$F$      velocity profile, $u/u_e$

$f$      mixing length function, equation (11)

$H$      probe outside height

$H_i^*$      incompressible form factor, $\displaystyle\int_0^\delta (1 - F)\,dy \Big/ \int_0^\delta F(1 - F)\,dy$

$h$      probe inside height

$I$      electric current

$K$      laminarization parameter, $\dfrac{\mu_e}{\rho_e u_e^2}\dfrac{du_e}{dx}$

$k$      thermal conductivity

$L$      exposed wire length

$l$      mixing length

$M$      Mach number

$N$      reciprocal of exponent in power-law velocity relation, equation (15)

$N_{Nu,t}$      Nusselt number, $\dot{q}d\Big/\left(T_{aw} - T_w\right)k_t$

$N_{Pr}$           Prandtl number,   $c_p\mu/k$

$N_{Pr,T}$         turbulent Prandtl number based on total-temperature gradients

$N_{Re}/m$         unit Reynolds number,   $\rho u/\mu$, per meter

$N_{Re}/ft$        unit Reynolds number,   $\rho u/\mu$, per foot

$N_{Re,x}$         local Reynolds number based on streamwise distance from flow origin

$N_{Re,1}$         pitot-probe Reynolds number based on local conditions ahead of probe
                   shock,   $\rho_1 u_1 H/\mu_1$

$N_{Re,\delta}$    boundary-layer-thickness Reynolds number,   $\rho_e u_e \delta/\mu_e$

$N_{Re,\theta}$    momentum-thickness Reynolds number,   $\rho_e u_e \theta/\mu_e$

$N_{St}$           Stanton number,   $\dfrac{\dot{q}_w}{\rho_e u_e c_p (T_{aw} - T_w)}$

$p$               pressure

$\dot{q}$          heat-transfer rate

$R$               ideal gas constant, 296.5 $m^2/sec^2$-K $\left(1770\ ft^2/sec^2\text{-}{}^{o}R\right)$ used for present
                   data

$r$               radius from axis of symmetry

$\hat{r}$          recovery factor,   $T_{aw}/T_t$

$T$               absolute temperature

$t$               time

$u$               velocity parallel to wall in direction of free-stream flow

$v$               velocity normal to wall

$W$               probe outside width

| x | axial distance from nozzle throat, or distance along thermocouple wire |
|---|---|
| y | normal distance from wall |
| $\beta$ | local wall angle with respect to nozzle center line |
| $\Gamma$ | intermittency function |
| $\gamma$ | ratio of specific heats, 1.4 used for present data |
| $\delta$ | boundary-layer thickness at point where $M \approx 0.995 M_e$ unless otherwise noted |
| $\delta^*$ | displacement thickness, equation (5) |
| $\epsilon$ | eddy viscosity or total hemispherical emissivity |
| $\theta$ | momentum thickness, equation (6) |
| $\bar{\theta}$ | normalized total-temperature parameter, $\left(T_t - T_w\right)\big/\left(T_{t,e} - T_w\right)$ |
| $\mu$ | viscosity |
| $\rho$ | density |
| $\sigma$ | Stephan-Boltzmann constant |
| $\tau$ | shear stress |
| $\bar{\chi}$ | viscous interaction parameter, $M_e{}^3\left(\dfrac{\mu_w}{\mu_e}\dfrac{T_e}{T_w}\dfrac{1}{N_{Re,x}}\right)^{1/2}$ |

Subscripts:

| A | alumel |
|---|---|
| a | ambient |
| av | average |

| | |
|---|---|
| aw | adiabatic temperature of wall or of bare-wire probe |
| C | chromel |
| c | longitudinal curvature |
| e | at "edge" of boundary layer |
| f | far-wall region |
| F.M. | free molecule |
| i | affected by wall interference |
| M | thermocouple junction |
| max | maximum |
| meas | measured |
| n | near-wall region |
| o | settling chamber |
| p | probe tip |
| ref | reference continuum value |
| S | wire temperature at $x = \pm L/2$ |
| s | viscous sublayer edge |
| T | turbulent or based on total-temperature profiles |
| t | local total or stagnation conditions |
| w | surface; or wire when applied to bare-wire probe |

| | |
|---|---|
| x | x-direction |
| y | y-direction |
| 1 | local undisturbed flow (ahead of normal shock caused by probe) |
| 2 | behind normal shock |
| $\theta$ | based on momentum thickness |

A primed symbol denotes a time fluctuating quantity and a superscript bar, except where otherwise noted, indicates a time mean value or correlation of the product of fluctuating quantities.

## APPARATUS AND TEST PROCEDURES

### Wind Tunnel

The experimental data were obtained in the Langley hypersonic nitrogen tunnel. A detailed description of the facility and its operation is given in reference 30. This facility has a water-cooled axisymmetric contoured nozzle with an exit diameter of 40.6 centimeters (16 in.) and an open-jet test section. The nozzle is about 3.2 meters (10.5 ft) in length (at the exit, x = 2.248 meters (88.5 in.)) and has wall static-pressure ports approximately every 0.3048 meter (1 ft) along the nozzle length. The facility can be operated for sustained periods of time (run times in excess of 2 hours) at stagnation pressures up to 6849 $N/cm^2$ (10 000 $lb/in^2$) and stagnation temperatures up to 2220 K (4000° R). The test gas is nitrogen with less than 5 parts per million of oxygen.

The nominal free-stream conditions for the present tests were at a Mach number of 19.5 and over a range of Reynolds numbers per meter of $1.9 \times 10^6$ to $3.0 \times 10^6$ $\left(5.8 \times 10^5 \text{ to } 9.2 \times 10^5 \text{ per ft}\right)$. The nominal total temperature was 1780 K (3200° R) and the wall-to-stagnation temperature ratio was approximately 0.17 at the boundary-layer-survey station which is 2.083 meters (82 in.) downstream of the throat. The variation in Mach number across the free-stream flow region is shown in reference 30. The axial variation in Mach number was found to be about 1.64 per meter (0.5 per ft) in the vicinity of the present survey station.

### Instrumentation

The pressure in the settling chamber was measured with a strain-gage transducer. The nominal accuracy of this gage, according to the manufacturer, is ±1 percent of full scale which is $10.3 \times 10^7$ $N/m^2$ (15 000 psia). The lowest stagnation pressure used in the present investigation was $2.7 \times 10^7$ $N/m^2$ (4000 psia) and by careful calibration procedures, the accuracy for this pressure range was held to ±2 percent of the indicated reading.

8

The stagnation temperature was measured in the settling chamber with a platinum-platinum 13 percent rhodium thermocouple attached to the tip of a 0.32-centimeter (1/8-in.) diameter, swaged, thin-wall tube that enclosed the thermocouple wire and high temperature insulation. The tube, or total-temperature probe, was mounted within the settling chamber just upstream of the approach section to the nozzle. (See ref. 30.) Corrections for heat conduction losses were neglected because of the construction and location of the probe. Estimated corrections due to radiation were from 3 to 5 percent of the measured probe temperature depending on the temperature assumed for surrounding surfaces. However, no radiation corrections were used because of uncertainties in the surrounding surface temperatures.

An independent check of the stagnation temperature was obtained from a heat balance based on the known mass-flow rate, the measured power input to the tungsten heater element, the measured air temperature at the inlet of the settling chamber, and estimated radiation and conduction losses. Values of total temperature obtained from this heat balance were generally about 3 percent higher than the measured values. However, because of uncertainties in radiation and conduction losses, temperatures shown or used in the present report are the measured values with no corrections. This procedure was justified partly on the basis of the aforementioned uncertainties in radiation and conduction effects and partly due to the relatively small effect of a nominal increase in $T_O$ on the normalized total-temperature profiles. Thus, the maximum effect of a 5-percent increase in $T_O$ on the values of $T_t/T_O$ was about 6 percent.

Sketches of the boundary-layer probes and water-cooled strut support are given in figure 1. Most of the pitot-pressure data reported herein were obtained with the flattened stainless-steel tube mounted on the end of the strut next to the wall as indicated in the figure. This flattened tube had external dimensions at the mouth of 0.381 centimeter (0.15 in.) wide by 0.028 centimeter (0.011 in.) high. The total-temperature probe was a chromel-alumel bare-wire thermocouple of 0.025-centimeter (0.01-in.) diameter placed normal to the flow. The length-to-diameter ratio of the portion of the thermocouple normal to the flow was 25.

The location of the survey probes normal to the wall surface and in the streamwise direction was controlled by a precision boundary-layer-survey mechanism accurate to 0.0025 centimeter (0.001 in.). The probes were traversed normal to the nozzle wall by remote control and a low voltage contact indicator stopped the movement at the wall surface. The data were continuously monitored during the tests and were not used until the pressure or temperature readings reached a constant level for a selected position in the boundary layer.

Both the static and the pitot pressures were measured with absolute pressure transducers. The basic pressure sensor is a high precision, stable capacitive bridge, the

Nozzle wall

Flow

.144 (.366)

.005
(.013)

.011
(.028)

.15 (.381)

End view of
flattened tube

1.25
(3.18)

5°

Interchange
with temp. probe

1.00
(2.54)

1.00
(2.54)

Temperature probe

Chromel

$L = \begin{cases} (.635) \\ .25 \end{cases}$

(.025)
.010 } = diam.

Alumel

15°

57.5°

Flow

1.5 (3.81)

Flow

L/d = 25

Round tubes:
Inside diam. = .09 (.23)
Outside diam. = .125 (.318)

Top view of total temperature
probe

.5
(1.27)

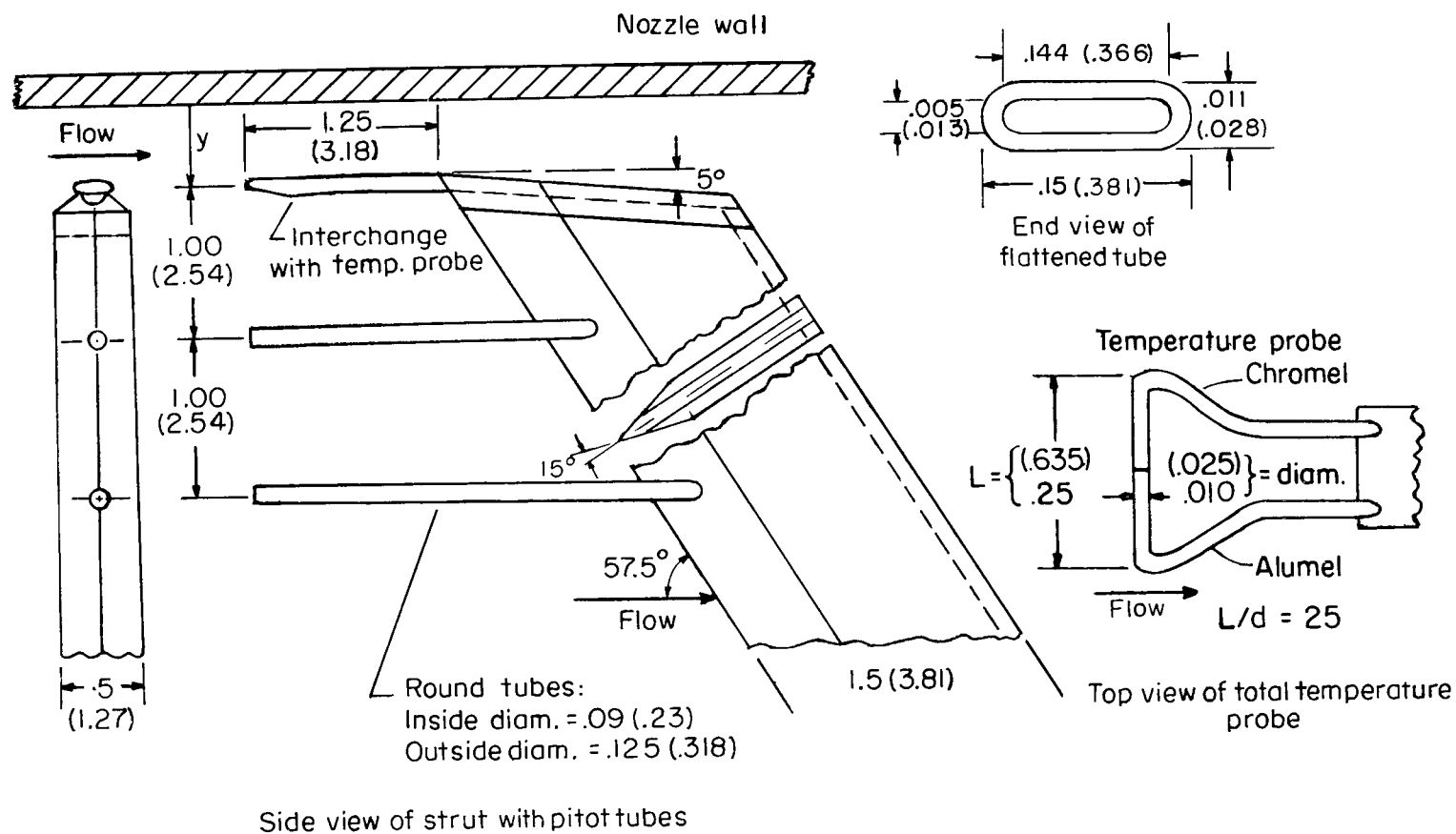Side view of strut with pitot tubes

,Figure 1.- Schematic sketch of probe and strut. Dimensions in inches (parenthetically in centimeters).

variable element of which is a thin, prestressed metallic diaphragm. The diaphragm is positioned between fixed capacitor plates, and its deflection is directly proportional to the magnitude of the pressure input. A regulated carrier voltage is applied across the capacitive bridge and the deflection of the diaphragm modulates the carrier voltage to provide an electrical output. The instruments used during this investigation have a range selection feature that provided seven ranges with full-scale readout on each range. Static pressures were measured with instruments which have a 0- to 50-torr scale on their highest range and a 0- to 0.5-torr scale on their lowest range. Pitot pressures were measured with instruments of 100-torr full scale on the highest range and 1-torr scale on the lowest range. Continuing checks of the calibrations indicate that accuracies of ±2 percent, or better, of full-scale readout were obtained.

## Test Conditions

A summary of the nominal test conditions for the experimental program is provided in table I. The temperature surveys were obtained during different runs than the pitot surveys, and the corresponding test conditions were somewhat different as indicated in the table. For the duration of a run (up to about 2 hours), the nominal settling-chamber conditions varied a maximum of about 9 percent. Hence, all boundary-layer probe data have been normalized by the appropriate stagnation values recorded at the same time as the probe data.

The nominal free-stream conditions at the survey station (x = 2.083 meters (82 in.)) where $r_w$ = 19.70 centimeters (7.758 in.) as given in table I were calculated by assuming isentropic expansion to the measured pitot pressures of an ideal gas with $\gamma$ = 1.4. The ideal gas properties of nitrogen (R = 296.5 $m^2/sec^2$-K (1770 $ft^2/sec^2$-°R)) have been used in all boundary-layer data-reduction procedures in the present investigation. The use of real gas properties, as obtained, for example, from reference 31, would affect computed flow properties by, at most, only a few percent. In view of other uncertainties in corrections for boundary-layer probe data, the use of real gas properties was not warranted for the present range of conditions. The viscosity for nitrogen was computed from equation (44) of reference 32.

TABLE I.- NOMINAL STAGNATION AND TEST CONDITIONS AT  x = 2.083 METERS (82 IN.)  AND  $T_w$ = 300 K (540° R)

[First and second sets of values for any given condition are for pitot-pressure and stagnation-temperature runs, respectively]

| Symbol | Condition | $T_o$ | | $p_o$ | | $p_{t,2,e}/p_o$ | $M_e$ | $N_{Re}/m$ | $N_{Re}/ft$ | $p_e/p_o$ | $\rho_e/\rho_o$ | $p_w/p_o$ |
|---|---|---|---|---|---|---|---|---|---|---|---|---|
| | | K | °R | N/cm² | lb/in² | | | | | | | |
| O | 1 | 1680 | 3020 | 2970 | 4300 | $0.1291 \times 10^{-3}$ | 19.28 | $2.02 \times 10^6$ | $6.18 \times 10^5$ | $0.269 \times 10^{-6}$ | $0.203 \times 10^{-4}$ | $0.391 \times 10^{-6}$ |
| | | 1695 | 3050 | 2830 | 4100 | | | 1.90 | 5.78 | | | |
| □ | 2 | 1780 | 3200 | 4310 | 6250 | .1245 | 19.42 | 2.62 | 7.98 | .256 | .1958 | .389 |
| | | 1695 | 3050 | 4380 | 6350 | | | 2.90 | 8.84 | | | |
| ◇ | 3 | 1835 | 3300 | 5550 | 8050 | .1175 | 19.65 | 2.98 | 9.08 | .236 | .1848 | .390 |
| | | 1835 | 3300 | 5590 | 8100 | | | 3.00 | 9.16 | | | |

A complete tabulation of the uncorrected pitot pressures and total temperatures measured in the boundary layer and normalized with their respective settling-chamber values is given in table II. Also included in table II for comparison are the corresponding corrected values. The final corrected data are also given in table III together with the resulting profiles of Mach number, velocity, static temperatures, and total temperature. The various sources of errors in probe data and the procedures used herein to determine the corrections will now be discussed in detail.

TABLE II.- UNCORRECTED AND CORRECTED VALUES OF PITOT PRESSURES AND TOTAL TEMPERATURES

AT   x = 2.083 METERS (82 IN.)

(a) Condition 1,   $M_e = 19.28$

| | | $p_o \approx 2970$ N/cm² (4300 lb/in²) | | | | | | $p_o \approx 2830$ N/cm² (4100 lb/in²) | | | | | |
|---|---|---|---|---|---|---|---|---|---|---|---|---|---|
| y | | $p_{t,2}/p_o$ | | y | | $p_{t,2}/p_o$ | | y | | $T_t/T_o$ | | $T_o$ | |
| cm | in. | Uncorrected | Corrected | cm | in. | Uncorrected | Corrected | cm | in. | Uncorrected | Corrected | K | °R |
| 0.2743 | 0.108 | 1.059 × 10⁻⁶ | 0.580 × 10⁻⁶ | 10.180 | 4.008 | 125.2 × 10⁻⁶ | 126.37 × 10⁻⁶ | 0.2019 | 0.0795 | 0.226 | 0.225 | 1678 | 3020 |
| .7823 | .308 | 1.261 | .639 | 10.434 | 4.108 | 127.1 | 127.10 | .7099 | .2795 | .227 | .349 | 1689 | 3040 |
| 1.0363 | .408 | 1.419 | .690 | 10.688 | 4.208 | 128.3 | 128.30 | 1.2179 | .4795 | .309 | .423 | 1694 | 3050 |
| 1.2903 | .508 | 1.820 | .866 | 10.942 | 4.308 | 128.5 | 128.50 | 1.7259 | .6795 | .347 | .515 | 1706 | 3070 |
| 1.5443 | .608 | 2.316 | 1.092 | 11.196 | 4.408 | 128.5 | 129.10 | 2.2339 | .8795 | .392 | .625 | 1706 | 3070 |
| 1.7983 | .708 | 2.740 | 1.282 | 11.450 | 4.508 | 131.0 | 131.0 | 2.7419 | 1.0795 | .4375 | .735 | 1717 | 3090 |
| 2.0523 | .808 | 3.927 | 1.853 | 11.704 | 4.608 | 131.0 | No correction | 3.2499 | 1.2795 | .489 | .755 | 1667 | 3000 |
| 2.3063 | .908 | 4.996 | 2.393 | 11.958 | 4.708 | 131.0 | | 3.7579 | 1.4795 | .521 | .772 | 1700 | 3060 |
| 2.5603 | 1.008 | 6.159 | 2.994 | 12.212 | 4.808 | 132.0 | | 4.2695 | 1.6795 | .549 | .795 | 1694 | 3050 |
| 2.8143 | 1.108 | 7.368 | 3.644 | 12.466 | 4.908 | 131.0 | | 4.7739 | 1.8795 | .574 | .792 | 1689 | 3040 |
| 3.0683 | 1.208 | 9.016 | 4.566 | 12.720 | 5.008 | 131.0 | | 5.2819 | 2.0795 | .591 | .805 | 1689 | 3040 |
| 3.5763 | 1.408 | 13.380 | 7.378 | 12.974 | 5.108 | 130.0 | | 5.7899 | 2.2795 | .608 | .825 | 1706 | 3070 |
| 3.8303 | 1.508 | 16.370 | 9.466 | 13.228 | 5.208 | 129.9 | | 6.2979 | 2.4795 | .623 | .862 | 1711 | 3080 |
| 4.0843 | 1.608 | 19.920 | 11.918 | 13.736 | 5.408 | 124.5 | | 6.8059 | 2.6795 | .636 | .885 | 1722 | 3100 |
| 4.3383 | 1.708 | 23.250 | 14.143 | 13.990 | 5.508 | 124.5 | | 7.3139 | 2.8795 | .649 | .899 | 1739 | 3130 |
| 4.5923 | 1.808 | 25.280 | 15.347 | 14.244 | 5.608 | 124.7 | | 7.8219 | 3.0795 | .653 | .919 | 1761 | 3170 |
| 4.8463 | 1.908 | 29.68 | 18.008 | 14.498 | 5.708 | 127.0 | | 8.3299 | 3.2795 | .661 | .932 | 1772 | 3190 |
| 5.1003 | 2.008 | 33.28 | 21.965 | 14.752 | 5.808 | 128.5 | | 8.8379 | 3.4795 | .672 | .950 | 1778 | 3200 |
| 5.3543 | 2.108 | 37.74 | 27.570 | 15.006 | 5.908 | 129.0 | | 9.3459 | 3.6795 | .677 | .959 | 1789 | 3220 |
| 5.6083 | 2.208 | 41.49 | 32.803 | 15.260 | 6.008 | 126.5 | | 9.8539 | 3.8795 | .684 | .971 | 1794 | 3230 |
| 5.8623 | 2.308 | 45.51 | 38.315 | 15.551 | 6.108 | 128.5 | | 10.362 | 4.0795 | .690 | .980 | 1794 | 3230 |
| 6.1163 | 2.408 | 49.84 | 43.734 | 15.768 | 6.208 | 130.0 | | 10.87 | 4.2795 | .694 | .990 | 1794 | 3230 |
| 6.3703 | 2.508 | 54.34 | 49.124 | 16.022 | 6.308 | 132.0 | | 11.378 | 4.4795 | .698 | 1.00 | 1794 | 3230 |
| 6.6243 | 2.608 | 58.31 | 53.796 | 16.276 | 6.40J | 133.0 | | 11.863 | 4.6705 | .700 | 1.00 | 1794 | 3230 |
| 6.8783 | 2.708 | 63.40 | 59.598 | 16.530 | 6.508 | 136.5 | | 12.394 | 4.8795 | .700 | 1.00 | 1794 | 3230 |
| 7.3863 | 2.908 | 74.58 | 72.298 | 16.784 | 6.608 | 138.0 | | | | | | | |
| 7.6403 | 3.008 | 80.4 | 78.648 | 17.038 | 6.708 | 139.0 | | | | | | | |
| 7.8943 | 3.108 | 85.76 | 84.487 | 17.546 | 6.908 | 138.5 | | | | | | | |
| 8.1483 | 3.208 | 90.96 | 90.115 | 17.800 | 7.008 | 136.0 | | | | | | | |
| 8.4023 | 3.308 | 95.23 | 94.741 | | | | | | | | | | |
| 8.6563 | 3.408 | 99.8 | 99.599 | | | | | | | | | | |
| 8.9103 | 3.508 | 104.0 | 104.11 | | | | | | | | | | |
| 9.1643 | 3.608 | 109.6 | 110.15 | | | | | | | | | | |
| 9.4183 | 3.708 | 114.3 | 115.06 | | | | | | | | | | |
| 9.6723 | 3.808 | 119.6 | 120.57 | | | | | | | | | | |
| 9.9263 | 3.908 | 123.1 | 124.29 | | | | | | | | | | |

# Probe Interference Effects

The question always arises as to whether or not the flow field is affected by the presence of survey probes. Various investigators have recognized the wall-interference problem and considered possible effects on pitot- or temperature-probe measurements (see, for example, refs. 19 and 33 to 35). Most investigators eliminate or discount data

TABLE II.- UNCORRECTED AND CORRECTED VALUES OF PITOT PRESSURES AND TOTAL TEMPERATURES

AT $x = 2.083$ METERS (82 IN.) — Continued

(b) Condition 2, $M_e = 19.42$

| \multicolumn{4}{c}{$p_o = 4310$ N/cm$^2$ (6250 lb/in$^2$)} | \multicolumn{6}{c}{$p_o = 4380$ N/cm$^2$ (6350 lb/in$^2$)} |
| y | | \multicolumn{2}{c}{$p_{t,2}/p_o$} | y | | \multicolumn{2}{c}{$T_t/T_o$} | \multicolumn{2}{c}{$T_o$} |
| cm | in. | Uncorrected | Corrected | cm | in. | Uncorrected | Corrected | K | °R |
|---|---|---|---|---|---|---|---|---|---|
| 0.2743 | 0.108 | $0.765 \times 10^{-6}$ | $0.4692 \times 10^{-6}$ | 0.2019 | 0.0795 | 0.226 | 0.253 | 1700 | 3060 |
| .5283 | .208 | .9847 | .5462 | .6337 | .2495 | .274 | .325 | 1672 | 3010 |
| .7823 | .308 | 1.354 | .6748 | 1.1417 | .4495 | .335 | .438 | 1689 | 3040 |
| 1.0363 | .408 | 1.897 | .9282 | 1.6497 | .6495 | .405 | .593 | 1656 | 2980 |
| 1.2903 | .508 | 2.439 | 1.1834 | 2.1577 | .8495 | .455 | .689 | 1672 | 3010 |
| 1.5443 | .608 | 3.412 | 1.6651 | 2.6657 | 1.0495 | .520 | .751 | 1644 | 2960 |
| 1.7983 | .708 | 4.578 | 2.2888 | 3.1737 | 1.2495 | .555 | .782 | 1667 | 3000 |
| 2.0523 | .808 | 5.903 | 3.0163 | 3.6817 | 1.4495 | .585 | .787 | 1667 | 3000 |
| 2.3063 | .908 | 6.815 | 3.5255 | 4.1897 | 1.6495 | .605 | .795 | 1678 | 3020 |
| 2.5603 | 1.008 | 8.749 | 4.7361 | 4.6977 | 1.8495 | .621 | .814 | 1689 | 3040 |
| 2.8143 | 1.108 | 10.71 | 6.0718 | 5.2057 | 2.0495 | .640 | .819 | 1656 | 2980 |
| 3.0683 | 1.208 | 13.11 | 7.8149 | 5.7137 | 2.2495 | .659 | .841 | 1644 | 2960 |
| 3.3223 | 1.308 | 16.39 | 10.306 | 6.2217 | 2.4495 | .680 | .882 | 1694 | 3050 |
| 3.5763 | 1.408 | 20.05 | 13.079 | 6.7297 | 2.6495 | .693 | .903 | 1700 | 3060 |
| 3.8303 | 1.508 | 22.96 | 15.142 | 7.2377 | 2.8495 | .710 | .931 | 1744 | 3140 |
| 4.0843 | 1.608 | 26.52 | 17.617 | 7.7457 | 3.0495 | .721 | .954 | 1744 | 3140 |
| 4.3383 | 1.708 | 29.03 | 20.658 | 8.2537 | 3.2495 | .730 | .966 | 1755 | 3160 |
| 4.5923 | 1.808 | 32.80 | 25.766 | 8.7617 | 3.4495 | .732 | .979 | 1800 | 3240 |
| 4.8463 | 1.908 | 36.84 | 31.378 | 9.2697 | 3.6495 | .743 | .999 | 1767 | 3180 |
| 5.1003 | 2.008 | 42.03 | 37.785 | 10.794 | 4.2495 | .750 | 1.00 | 1756 | 3160 |
| 5.3543 | 2.108 | 46.35 | 42.999 | 11.81 | 4.6495 | .732 | 1.00 | 1783 | 3210 |
| 5.6083 | 2.208 | 50.07 | 47.264 | | | | | | |
| 5.8623 | 2.308 | 55.42 | 53.411 | | | | | | |
| 6.1163 | 2.408 | 59.50 | 57.973 | | | | | | |
| 6.3703 | 2.508 | 65.95 | 65.017 | | | | | | |
| 6.6243 | 2.608 | 70.86 | 70.220 | | | | | | |
| 6.8783 | 2.708 | 76.14 | 75.891 | | | | | | |
| 7.1323 | 2.808 | 81.49 | 81.668 | | | | | | |
| 7.3863 | 2.908 | 87.41 | 87.753 | | | | | | |
| 7.6403 | 3.008 | 92.02 | 92.556 | | | | | | |
| 7.8943 | 3.108 | 96.99 | 97.686 | | | | | | |
| 8.1483 | 3.208 | 104.4 | 105.34 | | | | | | |
| 8.4023 | 3.308 | 109.8 | 110.82 | | | | | | |
| 8.6563 | 3.408 | 117.1 | 118.41 | | | | | | |
| 8.9103 | 3.508 | 119.5 | 121.31 | | | | | | |
| 9.1643 | 3.608 | 121.0 | 122.93 | | | | | | |
| 9.4183 | 3.708 | 123.2 | 124.50 | | | | | | |
| 9.6723 | 3.808 | 124.0 | No correction | | | | | | |
| 9.9263 | 3.908 | 124.2 | | | | | | | |
| 10.18 | 4.008 | 124.6 | | | | | | | |
| 10.434 | 4.108 | 126.2 | | | | | | | |
| 10.942 | 4.308 | 124.5 | | | | | | | |
| 11.45 | 4.508 | 122.0 | | | | | | | |

obtained in the region of wall interference and extrapolate trends indicated by remaining data to the wall.

In order to determine possible flow-field disturbances caused by the probes in the present tests, the wall pressure was monitored continuously as the survey probes were traversed away from the nozzle wall. Typical results are shown in figure 2 for surveys with the total-temperature probe and with the pitot-pressure probe at $x = 2.083$ meters (82 in.). The probe tips were located opposite the downstream edge of the nozzle-wall static-pressure orifice as indicated in the figure. Measured values of $p_{w,i}/p_o$ are

TABLE II.- UNCORRECTED AND CORRECTED VALUES OF PITOT PRESSURES AND TOTAL TEMPERATURES

AT $x = 2.083$ METERS (82 IN.) – Concluded

(c) Condition 3, $M_e = 19.65$

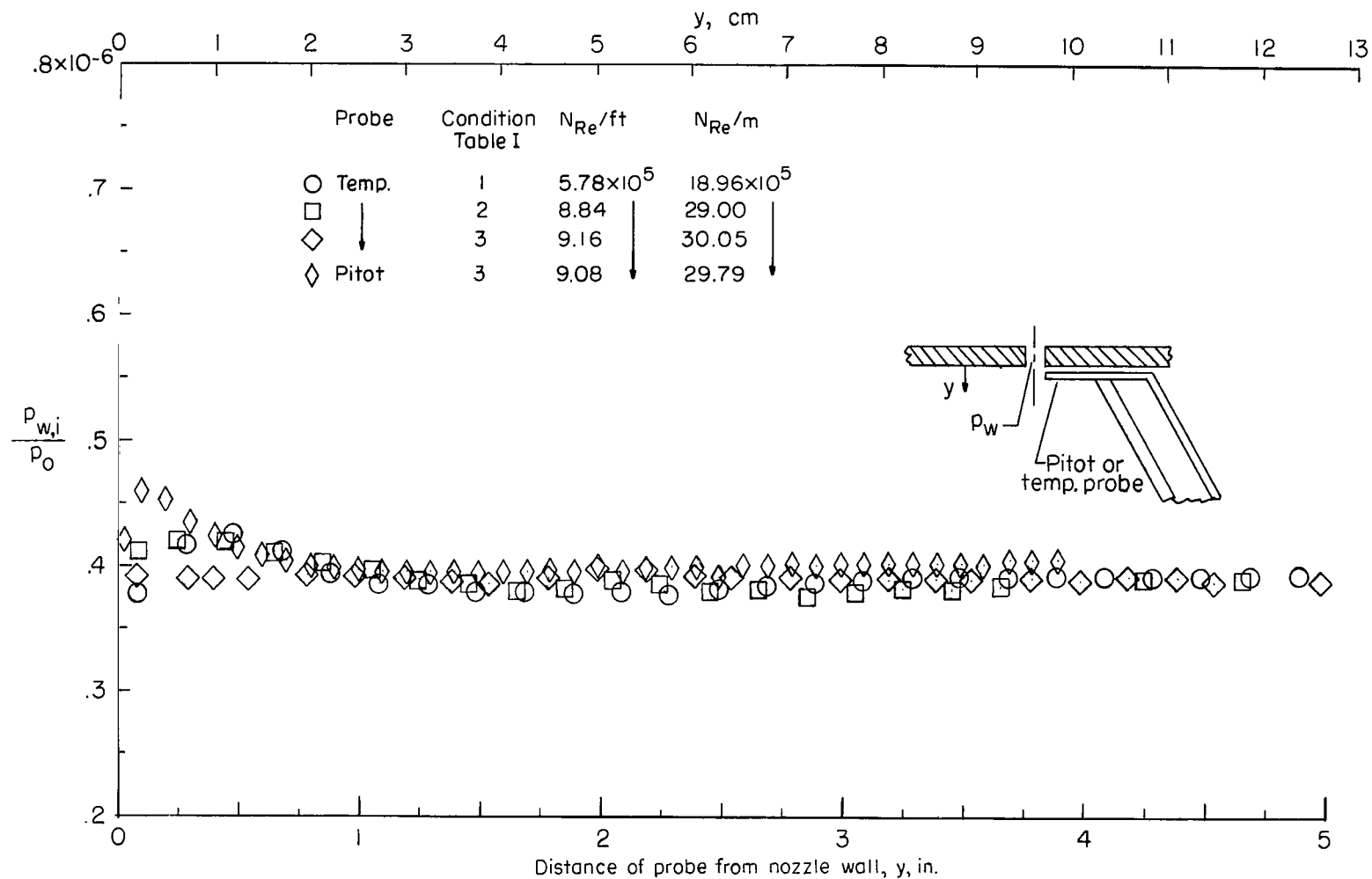| \multicolumn{6}{c}{$p_o = 5550$ N/cm² ( 8050 lb/in²)} | | | | | \multicolumn{6}{c}{$p_o \approx 5590$ N/cm² (8100 lb/in²)} | | | | | |
| y | | $p_{t,2}/p_o$ | | y | | $p_{t,2}/p_o$ | y | | $T_t/T_o$ | | $T_o$ | |
| cm | in. | Uncorrected | Corrected | cm | in. | | cm | in. | Uncorrected | Corrected | K | °R |
|---|---|---|---|---|---|---|---|---|---|---|---|---|
| 0.2743 | 0.108 | $0.735 \times 10^{-6}$ | $0.4591 \times 10^{-6}$ | 10.434 | 4.108 | $127.0 \times 10^{-6}$ | 0.2019 | 0.0795 | 0.208 | 0.227 | 1833 | 3300 |
| .5283 | .208 | 1.12 | .5992 | 10.688 | 4.208 | 125.5 | .7099 | .2795 | .290 | .385 | 1833 | 3300 |
| .7823 | .308 | 1.68 | .8286 | 10.942 | 4.308 | 122.0 | .9639 | .3795 | .361 | .501 | 1822 | 3280 |
| 1.0363 | .408 | 2.44 | 1.2026 | 11.196 | 4.408 | 119.0 | 1.4719 | .5795 | .428 | .641 | 1850 | 3330 |
| 1.2903 | .508 | 3.41 | 1.6811 | 11.45 | 4.508 | 118.0 | 1.9799 | .7795 | .500 | .762 | 1844 | 3320 |
| 1.5443 | .608 | 4.84 | 2.4515 | 11.704 | 4.608 | 113.0 | 2.4879 | .9795 | .541 | .786 | 1850 | 3330 |
| 1.7983 | .708 | 7.11 | 3.8144 | 11.958 | 4.708 | 112.0 | 2.9959 | 1.1795 | .572 | .795 | 1850 | 3330 |
| 2.0523 | .808 | 9.14 | 5.2117 | 12.212 | 4.808 | 111.0 | 3.5039 | 1.3795 | .600 | .808 | 1844 | 3320 |
| 2.3063 | .908 | 11.85 | 7.1397 | 12.466 | 4.908 | 109.0 | 4.0119 | 1.5795 | .621 | .823 | 1844 | 3320 |
| 2.5603 | 1.008 | 14.63 | 9.4464 | 12.72 | 5.008 | 107.5 | 4.5199 | 1.7795 | .636 | .834 | 1844 | 3320 |
| 2.8143 | 1.108 | 17.85 | 11.946 | 12.974 | 5.108 | 104.5 | 5.0279 | 1.9795 | .656 | .858 | 1844 | 3320 |
| 3.0682 | 1.208 | 21.0 | 14.396 | 13.228 | 5.208 | 103.5 | 5.5359 | 2.1795 | .673 | .881 | 1844 | 3320 |
| 3.3223 | 1.308 | 24.65 | 16.927 | 13.482 | 5.308 | 103.0 | 6.0439 | 2.3795 | .686 | .903 | 1844 | 3320 |
| 3.5763 | 1.408 | 28.35 | 20.962 | 13.736 | 5.408 | 105.0 | 6.6519 | 2.5795 | .707 | .929 | 1844 | 3320 |
| 3.8303 | 1.508 | 32.35 | 26.422 | 13.99 | 5.508 | 105.0 | 7.0599 | 2.7795 | .721 | .952 | 1844 | 3320 |
| 4.0843 | 1.608 | 35.45 | 32.161 | 14.244 | 5.608 | 103.5 | 7.5679 | 2.9795 | .736 | .974 | 1844 | 3320 |
| 4.3383 | 1.708 | 41.2 | 37.336 | 14.498 | 5.708 | 101.5 | 8.0759 | 3.1795 | .744 | .984 | 1844 | 3320 |
| 4.5923 | 1.808 | 46.1 | 43.167 | 14.752 | 5.808 | 102.0 | 8.5839 | 3.3795 | .751 | .999 | 1844 | 3320 |
| 4.8463 | 1.908 | 51.2 | 49.016 | 15.006 | 5.908 | 103.5 | 9.0919 | 3.5795 | .759 | 1.000 | 1844 | 3320 |
| 5.1003 | 2.008 | 55.7 | 54.360 | 15.26 | 6.008 | 105.0 | 9.5999 | 3.7795 | .756 | 1.000 | 1844 | 3320 |
| 5.3543 | 2.108 | 61.1 | 60.346 | 15.514 | 6.108 | 101.5 | 10.108 | 3.9795 | .761 | 1.000 | 1844 | 3320 |
| 5.6083 | 2.208 | 66.0 | 65.786 | 15.768 | 6.208 | 99.5 | 10.616 | 4.1795 | .759 | 1.000 | 1833 | 3300 |
| 5.8623 | 2.308 | 71.4 | 71.497 | 16.022 | 6.308 | 99.5 | 11.124 | 4.3795 | .756 | 1.000 | 1833 | 3300 |
| 6.1163 | 2.408 | 77.0 | 76.841 | 16.276 | 6.408 | 99.5 | 11.632 | 4.5795 | .753 | 1.000 | 1839 | 3310 |
| 6.3703 | 2.508 | 82.9 | 83.585 | 16.53 | 6.508 | 100.0 | 12.648 | 4.9795 | .746 | 1.000 | 1839 | 3310 |
| 6.6243 | 2.608 | 88.2 | 89.125 | 16.784 | 6.608 | 99.9 | | | | | | |
| 6.8783 | 2.708 | 94.4 | 95.385 | 17.038 | 6.708 | 95.5 | | | | | | |
| 7.1323 | 2.808 | 100.0 | 101.03 | 17.292 | 6.808 | 94.5 | | | | | | |
| 7.3863 | 2.908 | 104.0 | 105.43 | 17.546 | 6.908 | 93.0 | | | | | | |
| 7.6493 | 3.008 | 108.0 | 109.44 | | | | | | | | | |
| 7.8943 | 3.108 | 112.8 | 114.55 | | | | | | | | | |
| 8.1483 | 3.208 | 116.7 | 118.42 | | | | | | | | | |
| 8.4023 | 3.308 | 119.2 | 121.49 | | | | | | | | | |
| 8.6563 | 3.408 | 119.7 | 119.50 | | | | | | | | | |
| 8.9103 | 3.508 | 121.1 | No correction | | | | | | | | | |
| 9.1643 | 3.608 | 123.9 | | | | | | | | | | |
| .4183 | 3.708 | 125.8 | | | | | | | | | | |
| 9.6723 | 3.808 | 126.0 | | | | | | | | | | |
| 9.9263 | 3.908 | 127.5 | | | | | | | | | | |
| 10.18 | 4.008 | 127.5 | | | | | | | | | | |

Figure 2.- Wall-interference effects of temperature and pitot-pressure probes on wall static pressure at  x = 2.083 meters (82 in.).

## TABLE III.- EXPERIMENTAL BOUNDARY-LAYER PROFILES WITH ALL CORRECTIONS INCLUDED

(a) Condition 1: $\delta$ = 11.2 cm (4.4 in.); $M_e$ = 19.28; $\theta$ = 0.178 cm (0.070 in.); $\delta^*$ = 5.92 cm (2.33 in.); A = 1.0

| $y/\delta$ | $p/p_{t,2}$ | $M/M_e$ | $T/T_e$ | $T_t/T_o$ | $u/u_e$ | $\bar{\theta}$ |
|---|---|---|---|---|---|---|
| 0.018 | 708.0 $\times 10^{-3}$ | 0.0373 | 15.10 | 0.225 | 0.1451 | |
| .064 | 617.0 | .0446 | 21.15 | .349 | .2063 | 0.072 |
| .109 | 459.6 | .0581 | 24.10 | .423 | .2847 | .206 |
| .154 | 277.3 | .0804 | 24.72 | .515 | .3993 | .300 |
| .200 | 162.2 | .1089 | 23.78 | .625 | .5306 | .408 |
| .245 | 97.92 | .1426 | 21.03 | .735 | .6535 | .547 |
| .291 | 62.26 | .1805 | 16.98 | .755 | .7429 | .679 |
| .336 | 40.27 | .2256 | 12.97 | .772 | .8116 | .763 |
| .382 | 27.82 | .2723 | 9.74 | .795 | .8489 | .754 |
| .427 | 19.09 | .3294 | 6.95 | .792 | .8676 | .768 |
| .473 | 12.53 | .4072 | 4.67 | .805 | .8786 | .773 |
| .518 | 8.75 | .4876 | 3.34 | .825 | .8907 | .791 |
| .564 | 6.72 | .5576 | 2.65 | .862 | .9071 | .835 |
| .609 | 5.29 | .6276 | 2.16 | .885 | .9210 | .864 |
| .654 | 4.32 | .6950 | 1.81 | .899 | .9348 | .872 |
| .700 | 3.64 | .7573 | 1.55 | .919 | .9425 | .895 |
| .745 | 3.16 | .8117 | 1.39 | .932 | .9548 | .925 |
| .791 | 2.80 | .8640 | 1.25 | .950 | .9658 | .940 |
| .836 | 2.49 | .9150 | 1.14 | .959 | .9740 | .953 |
| .882 | 2.26 | .9611 | 1.05 | .971 | .9822 | .964 |
| .927 | 2.15 | .9865 | 1.01 | .980 | .9871 | .984 |
| .972 | 2.09 | .9984 | .99 | .990 | .9932 | .999 |
| 1.00 | 2.08 | 1.000 | 1.00 | 1.00 | 1.000 | 1.00 |

plotted against the distance of the probe from the wall. Wall static pressure was increased by a maximum of about 17 percent of the interference-free value $p_w$ (value at which the measured wall static pressure remains nearly constant with increasing distance of probe from wall) when the pitot probe was near the wall. Estimates of maximum interference effects when the local flow is supersonic were obtained by assuming that oblique shocks form in front of the pitot tube (see refs. 34 and 35) and that the static-pressure ratio across these shocks is given by $p_{w,i}/p_w$ as obtained from figure 2.

# TABLE III.- EXPERIMENTAL BOUNDARY-LAYER PROFILES WITH ALL CORRECTIONS INCLUDED – Continued

(b) Condition 2: $\delta$ = 9.4 cm (3.7 in.); $M_e$ = 19.42; $\theta$ = 0.173 cm (0.068 in.); $\delta^*$ = 4.62 cm (1.82 in.); A = 1.0

| $y/\delta$ | $p/p_{t,2}$ | $M/M_e$ | $T/T_e$ | $T_t/T_o$ | $u/u_e$ | $\bar{\theta}$ |
|---|---|---|---|---|---|---|
| 0.0213 | 859.6 $\times 10^{-3}$ | 0.0242 | 17.73 | 0.253 | 0.1023 | 0.0932 |
| .0671 | 643.0 | .0422 | 20.62 | .325 | .1924 | .1775 |
| .1211 | 359.9 | .0680 | 23.60 | .438 | .3311 | .316 |
| .1750 | 187.3 | .0999 | 24.09 | .593 | .4921 | .502 |
| .2290 | 103.6 | .1375 | 20.42 | .689 | .6236 | .621 |
| .2828 | 47.47 | .2060 | 12.63 | .751 | .7347 | .695 |
| .3368 | 29.45 | .2626 | 9.03 | .782 | .7923 | .735 |
| .3906 | 18.40 | .3332 | 6.01 | .787 | .8200 | .740 |
| .4445 | 12.22 | .4094 | 4.20 | .795 | .8424 | .751 |
| .4983 | 8.57 | .4892 | 3.10 | .814 | .8649 | .774 |
| .5520 | 6.34 | .5690 | 2.29 | .819 | .8650 | .796 |
| .6062 | 5.00 | .6411 | 1.86 | .841 | .8767 | .804 |
| .6600 | 4.13 | .7055 | 1.67 | .882 | .9142 | .856 |
| .7140 | 3.53 | .7631 | 1.47 | .903 | .9281 | .884 |
| .7680 | 3.05 | .8213 | 1.35 | .931 | .9561 | .918 |
| .8220 | 2.66 | .8795 | 1.21 | .954 | .9689 | .944 |
| .8740 | 2.37 | .9310 | 1.09 | .966 | .9789 | .958 |
| .9300 | 2.17 | .9743 | 1.04 | .979 | .998 | .975 |
| .9840 | 2.72 | .9964 | 1.01 | .999 | .999 | .998 |
| 1.000 | 2.09 | 1.000 | 1.00 | 1.00 | 1.00 | 1.00 |

The Mach number distribution downstream of the oblique shocks was obtained from the Rayleigh pitot-pressure formula using the measured pitot pressure (corrected for viscous and rarefaction effects) and the disturbed wall static pressure $p_{w,i}$, also from figure 2. The Mach number distribution upstream of the assumed oblique shocks could then be computed and these values were, at most, 0.07 larger than the downstream values. Hence, no corrections for wall-interference effects have been applied to measured values of pitot pressure and stagnation temperature, and the interference-free values of wall static pressures $p_w$ have been used in all data-reduction procedures which are discussed in subsequent sections herein.

## TABLE III.- EXPERIMENTAL BOUNDARY-LAYER PROFILES WITH ALL CORRECTIONS INCLUDED – Concluded

(c) Condition 3: $\delta$ = 8.65 cm (3.4 in.); $M_e$ = 19.65; $\theta$ = 0.155 cm (0.061 in.); $\delta^*$ = 4.31 cm (1.70 in.); A = 1.0

| $y/\delta$ | $p/p_{t,2}$ | $M/M_e$ | $T/T_e$ | $T_t/T_o$ | $u/u_e$ | $\bar{\theta}$ |
|---|---|---|---|---|---|---|
| 0.0234 | 859.6 $\times 10^{-3}$ | 0.0239 | 16.94 | 0.227 | 0.0982 | 0.0756 |
| .0822 | 498.0 | .0534 | 25.30 | .385 | .2467 | .205 |
| .1116 | 343.5 | .0692 | 28.36 | .501 | .3677 | .403 |
| .1704 | 160.8 | .1074 | 26.66 | .641 | .5531 | .571 |
| .2292 | 71.92 | .1643 | 19.38 | .762 | .7218 | .716 |
| .2881 | 38.52 | .2264 | 12.47 | .786 | .7977 | .744 |
| .3469 | 23.64 | .2901 | 8.35 | .795 | .8359 | .756 |
| .4057 | 15.30 | .3613 | 5.72 | .808 | .8619 | .773 |
| .4645 | 10.45 | .4376 | 4.09 | .823 | .8826 | .788 |
| .5233 | 7.44 | .5191 | 3.00 | .834 | .8969 | .802 |
| .5822 | 5.71 | .5929 | 2.39 | .858 | .9148 | .831 |
| .641 | 4.55 | .6641 | 1.97 | .881 | .9299 | .859 |
| .6998 | 3.72 | .7328 | 1.67 | .903 | .9441 | .883 |
| .7587 | 3.15 | .7990 | 1.45 | .929 | .9593 | .917 |
| .8175 | 2.72 | .8600 | 1.29 | .952 | .9725 | .944 |
| .8763 | 2.40 | .9160 | 1.16 | .974 | .9848 | .970 |
| .9351 | 2.15 | .9669 | 1.06 | .984 | .9907 | .981 |
| .9939 | 2.04 | .995 | 1.02 | .999 | .998 | .998 |
| 1.000 | 2.05 | 1.00 | 1.00 | 1.000 | 1.000 | 1.00 |

When the local flow is subsonic and $p_w$ is used with measured pitot pressures to compute Mach number, the only wall-interference effect would be caused by displacement of streamlines away from the wall due to local flow separation as the probe approached the wall. The subsonic data should then be plotted at smaller values of y than indicated. Since the magnitude of this effect is probably small for the present conditions, no corrections have been applied.

### Pitot-Pressure Corrections
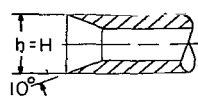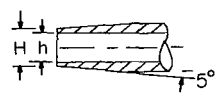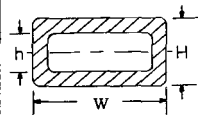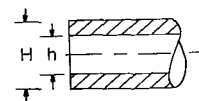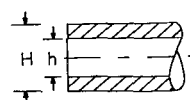
Effect of thermal diffusion.- The pressure-survey data were obtained for nominal stagnation temperatures of 1670 to 1830 K (3000° to 3300° R). Because of the resulting high temperatures near the opening of the pitot tubes, the pressure measurements could

be affected by thermal diffusion since the probe strut was water cooled. An uncooled length of pitot tube extended about 3.2 centimeters (1.25 in.) ahead of the strut support. In order to compute corrections for this effect, the temperature distribution along the pitot tube would have to be known. Even if this temperature distribution were known, accurate corrections could not be computed for the present tests because of the complex geometry of the tip of the pitot tube. (See fig. 1.) Estimates of the thermal-diffusion effect were based on the assumptions that the temperature of the pitot-probe lip is the same as the measured total temperature (uncorrected) and that a mean-effective hydraulic radius for the probe tip region of 0.043 centimeter (0.017 in.) can be used in place of the radius of a circular tube. From the method of reference 36, the maximum error was then obtained as 4 percent when the temperature of the cold end of the tube was taken as 300 K (540° R). Since these assumptions are probably conservative, no corrections for this effect have been used.

Viscous and rarefied flow effects.- Studies of viscous and rarefied flow effects on impact pressure measurements have been reported in references 33 and 37 through 43. It was concluded (ref. 43) that the interpretation of impact pressure measurements at low density or low probe Reynolds numbers (as would be the case in the near-wall region) may be uncertain. Viscous effects on flattened probes were obtained over a limited Reynolds number range during the present investigation. Impact pressures were measured in the free stream with three tubes of different sizes and width to height ratios. The reference pressure was measured with a large pitot probe of 0.84-centimeter (0.33-in.) height. The results are compared with those of references 33 and 37 to 42 in figure 3. The symbol key used for the data in this figure and information on probe geometry are given in table IV. The faired lines represent the mean of data from all sources (short dashed lines are extrapolations) and have been used for the corrections applied herein. Alternate ways of plotting these data are illustrated in references 33 and 37 to 42; however, the present plot shows the Mach number effect explicitly and appeared to correlate the data better than Knudsen number or normal-shock Reynolds number $\rho_2 u_2 H / \mu_t$.

Very little data are available for $N_{Re,1} < 10$ except at $M_1 < 2.0$. Hence, for $N_{Re,1} < 10$, the faired lines used for pitot-pressure corrections are based on trends of available data and consideration of the appropriate free-molecule limiting values computed (formula (7-6), p. 702, ref. 44) with the assumption that the reflection coefficients are completely diffuse. The results of this calculation for the free-molecule limiting values are plotted on the insert in figure 3. The maximum effect occurs at Mach number 1.0 and depends on the ratio of the probe temperature to stagnation temperature. The short-dashed-line curves in figure 3 represent arbitrary extrapolations to the free-molecule limits for $T_p / T_o \approx 1.0$.

TABLE IV.- SYMBOL KEY FOR VISCOUS AND RAREFACTION CORRECTIONS TO PITOT PRESSURES AS SHOWN IN FIGURE 3

| Symbol | $M_e$ | H, cm (in.) | h/H | W/H | Configuration | Author reference number |
|---|---|---|---|---|---|---|
| | | Supersonic and hypersonic data | | | | |
| ◯ | 1.7 to 2.0 | 0.254 to 2.54 (0.1 to 1.0) | 1.0 | 1.0 | | Sherman, 37 |
| + | 2.3 to 2.7 | ↓ | ↓ | ↓ |  | |
| △ | 2.8 to 3.4 | | | | | |
| Reference tube | | 1.52 to 2.54 (0.6 to 1.0) | | | | |
| — ·· — | 1.23 to 1.99 | 0.254 to 2.54 (0.1 to 1.0) | 0.85 to 0.90 | 1.0 |  | Kosterin et al., 38 |
| + — + — + — | 4.4 to 4.6 | ↓ | | | | |
| — ·· — — | 5.5 to 5.7 | | | | | |
| — — — | 6.3 to 6.5 | ↓ | ↓ | ↓ | | |
| Reference tube, Rayleigh formula | | | | | | |
| — · — | 1.46 | 0.0356 to 1.588 (0.014 to 0.625) | 1.0 | 1.0 | 10° external chamfered | Enkenhus, 39 |
| Reference tube, Rayleigh formula | | | | | | |
| ———— | 25.5 | 0.0584 to 1.27 (0.023 to 0.50) | ---------- | 1.0 | External chamfered + thermal trans. corrected | White, 40 |
| Reference tube | | ↓ 1.27 (0.50) | | ↓ | | |
| ◇ | 23 to 26 | 0.127 (0.050) | 0.800 | 2.0 | Flattened probe | McCroskey, 33 |
| □ | | 0.0356 (0.014) | .785 | 8.57 |  | |
| ◇ | | 0.0279 (0.011) | .541 | 10.9 | | |
| ◿ | | 0.0152 (0.006) | .666 | 13.3 | | |
| Reference tube | | 0.318 (0.125) | ---------- | 1.0 | | |
| ● | 18 to 20 | 0.0762 (0.030) | 0.434 | 3.93 | See previous sketch for reference 33 | Present |
| ■ | | 0.0406 (0.016) | .250 | 8.18 | | |
| ◆ | | 0.0380 (0.015) | .466 | 8.66 | | |
| Reference tube | | 0.838 (0.330) | .880 | 2.14 | | |
| — — — | 14.20 | 0.635 to 0.0508 (0.25 to 0.02) | 0.75 | 1.0 |  | Daum et al., 41 |
| — — — — | 16.72 | ↓ | ↓ | ↓ | | |
| — — | 18.32 | | | | | |
| Reference tube, extrapolated $\left(p_{t,2}\right)_M$ vs. $H^{-1}$ to infinite Reynolds number | | | | | | |
| | | Subsonic data | | | | |
| △ | 0.512 | 0.76 to 3.8 (0.3 to 1.5) | 1.0 | 1.0 | See previous sketch for reference 37 | Sherman, 37 |
| ▽ | .33 | ↓ | ↓ | ↓ | | |
| ◁ | .164 | | | | | |
| Reference tube, $\left(p_{t,2}\right)_{ideal} = p_0$ | | | | | | |
| ⊕ | 0.29 | 0.0406 (0.016) | 0.55 | 1.0 |  | Pollard, 42 |
| ⊞ | .57 | ↓ | | | | |
| ◈ | .79 | | | | | |
| ⬙ | .98 | 0.954 (0.374) | | | | |
| Reference tube | | 0.696 (0.274) | ↓ | ↓ | | |

20

Figure 3.- Viscous and rarefied flow effects on ratio of measured to continuum pitot pressures for $\gamma = 7/5$. Symbol key given in table IV.

An iterative procedure (see appendixes A and B) was required to determine the local probe Reynolds number $\left(N_{Re,1} = \rho_1 u_1 H / \mu_1\right)$ in the present data-reduction procedure. Large corrections were obtained for pitot-pressure data in the near-wall region, and significant corrections were required up to 5.1 centimeters (2 in.) from the wall. Hence all data presented in table III have been corrected where required. In general, the corrections reduced the measured pitot pressure in the wall region since the rarefied flow effect caused the indicated measurements to read high in this region where $N_{Re,1} < 100$ and $M_{e,1} < 6.0$. The magnitude of the corrections used through the boundary layer can be obtained for all runs from comparisons of values listed in table II for the uncorrected and corrected pitot pressures. Also, for the lowest pressure run (condition 1 in table I) where the corrections would be the largest, the final values of $\left(p_{t,2}\right)_{meas} / \left(p_{t,2}\right)_{ref}$ are plotted against the corresponding values of $N_{Re,1}$ in figure 3 as the $\chi$ symbols. For this condition the maximum correction ratio for the pitot pressure was 2.14 where the local probe Reynolds number was 0.45. The smallest probe Reynolds number for all three runs was 0.39 at $y = 0.274$ centimeter (0.108 in.).

Effects of turbulent fluctuations.- The turbulent fluctuations in velocity and density will generally increase the local mean pitot pressures according to the analysis of reference 45. The maximum increase for the present conditions was estimated to be about 10 percent based on the data correlations and discussion of reference 45. This maximum increase in measured pitot pressure would occur in the vicinity of the viscous-sublayer edge which, in the present tests, was located about 1.91 centimeters (0.75 in.) from the wall. The corresponding maximum increase in Mach number would be about 6 percent. No attempt has been made to correct the pitot pressures for these effects because of uncertainties in the magnitude and distribution of the fluctuating quantities and of the second-order correlation coefficient (see ref. 45) for the present conditions.

Another effect of turbulent fluctuations is manifested through the acoustic response of the measurement system (the probe, tubing, and transducer volume). This effect has been treated in reference 46 where it was shown that the mean pressures may be further increased due to the acoustic response of the system by amounts that are comparable to the increases noted in the previous paragraph. Since no general analysis of this effect is possible for supersonic turbulent flow, such effects are not considered further herein.

### Corrections for Radiation and Conduction Losses to Temperature Probe

The data from the bare-wire chromel-alumel thermocouple used in the surveys were corrected for heat losses due to radiation and conduction. A detailed discussion of the method used and auxiliary data required for correcting the temperature survey data are given in appendixes A and B. Corrections due to conduction and radiation varied through the boundary layer and were 20 to 30 percent in the free stream. An indication

of the magnitude of the correction applied through the boundary layer may be obtained by comparing values from table II for the uncorrected and corrected total temperatures. Consideration of all sources of error in the data-reduction procedure for total temperature (excluding any temperature-probe interference effects and any effects of fluctuating values) indicates that the final dimensionless profiles are correct to within approximately ±10 percent.

## EXPERIMENTAL RESULTS

### Pressure and Temperature Measurements

Pitot-pressure profiles.- Figure 4 shows the variation in the ratio of pitot-to-total pressure with distance from the nozzle wall for the three test runs (table I). Corrections for viscous and rarefaction effects have been applied to the pitot data. The pitot-pressure data have been normalized by the settling-chamber pressure recorded at the same time to account for any slight variation in total pressure during the survey runs. Pitot-pressure data were obtained in the inviscid flow out to 17.8 centimeters (7 in.) from the nozzle wall for the test runs at the upper and lower total pressures. The degree of flow uniformity in the inviscid stream at the measuring station (x = 2.083 meters (82 in.)) is apparent from these data for y > 10.2 centimeters (4 in.). There is very little scatter in the experimental data, however, there is a slight peak in the pitot profiles as they join the inviscid core flow (8.6 cm < y < 12.7 cm (3.4 in. < y < 5.0 in.)). The nominal boundary-layer edge δ has been chosen somewhat closer to the wall than the location of the peak pitot pressure for each test. While the resulting values of δ cannot be specified accurately, they provide an approximate indication of boundary-layer thickness and in terms of y/δ, the profiles tend to collapse to about the same distributions as will be shown in subsequent sections of this report.

Previous investigations (see ref. 47) have shown that nozzle-wall turbulent boundary layers may differ from flat-plate boundary layers at similar conditions. These differences would be due to upstream wall temperature and pressure gradients along the wall as well as normal pressure gradients, none of which would exist for uniform flat-plate flows. Any upstream wave system (resulting from an overexpansion at the throat, for example) would have some effect on the turbulent boundary-layer profiles. Also, such an upstream wave system could have some influence on the peak pitot pressure measured in the vicinity of the boundary-layer edge as seen in figure 4 at y ≈ 10.2 centimeters (4 in.).

In order to determine the effects of such wave systems or disturbances on the inviscid flow field in the nozzle, a center-line pitot-pressure survey was made from about 5.1 centimeters (2 in.) downstream of the nozzle throat to the exit (x = 2.248 meters (88.5 in.)). These data were used to compute the Mach number (with isentropic flow
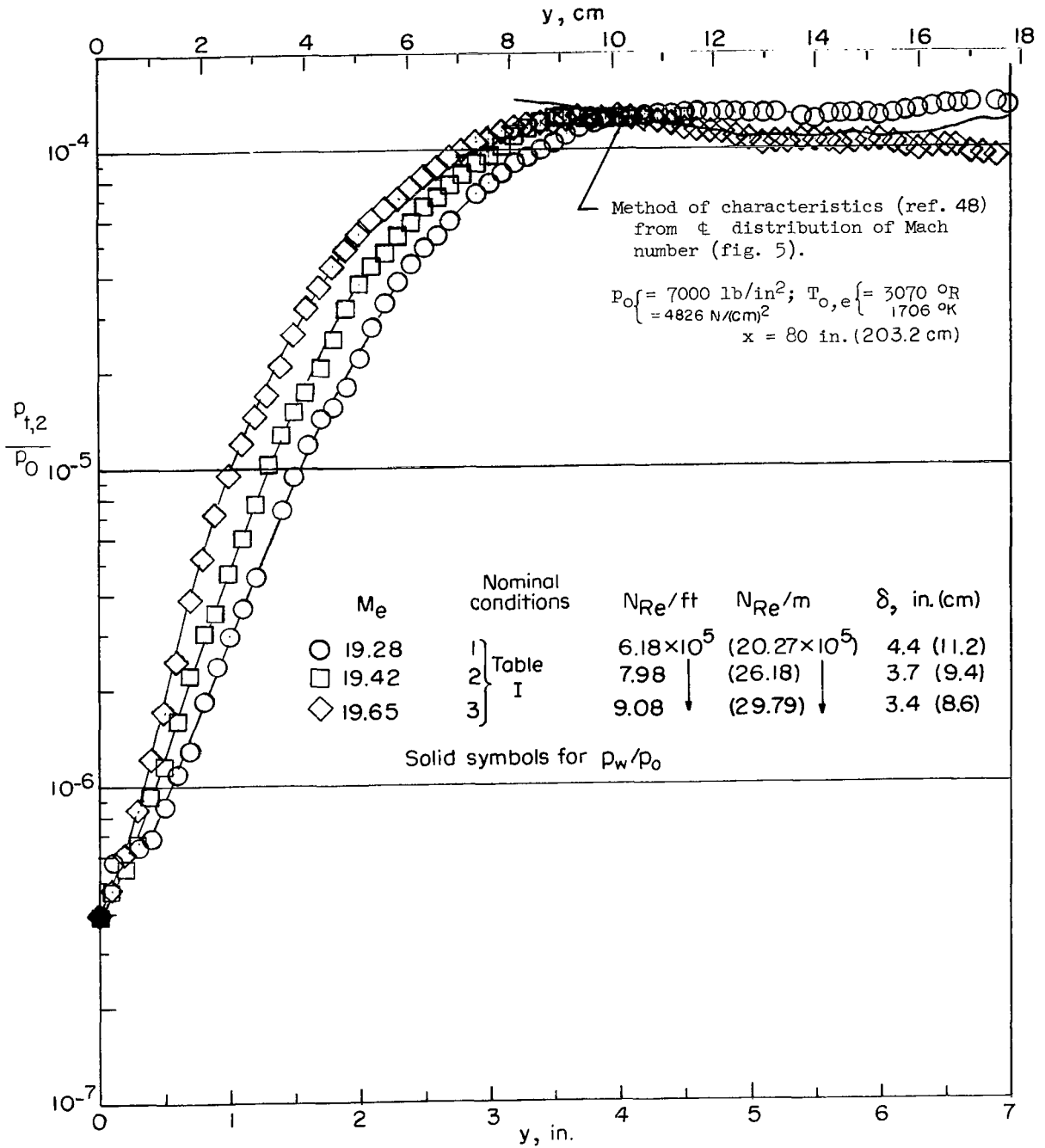
Figure 4.- Pitot-pressure profiles corrected for viscous and rarefied flow effects. (Uncorrected values given in table II.)

assumed from the settling chamber) and the results are shown in figure 5. It is seen that disturbances exist for distances greater than about 1/3 of the nozzle length with a large overexpansion from $x \approx 64$ to 98 centimeters (24 to 37 in.). These disturbances tend to diminish further downstream as the $x = 2.083$-meter (82-in.) station is approached.

To investigate the origin of the overexpansion and subsequent disturbances in the nozzle, the inviscid flow field based on this center-line Mach number distribution was calculated by the method of characteristics as applied to nozzle flows in reference 48. Equilibrium real gas properties of nitrogen were used in this calculation with stagnation conditions taken as $p_o = 4830$ N/cm$^2$ (7000 lb/in$^2$) and $T_o = 1705$ K (3070$^o$ R). (The data of fig. 5 were obtained with $p_o = 3450$ N/cm$^2$ (5000 lb/in$^2$); however, the computed results for this value of $p_o$ would be nearly identical to those with $p_o = 4830$ N/cm$^2$ (7000 lb/in$^2$).) The results of this inviscid-flow-field calculation showed that the center-line overexpansion originates in a region on the wall just slightly downstream of the nozzle-wall inflection point. (This finding is consistent with the results of ref. 49, which indicates the overexpansion may be caused by the abrupt change in slope of the center-line Mach number distribution used in the original design calculation. For the present nozzle, this change in slope was at $x \approx 92.60$ centimeters (36.5 in.).) The lateral pitot-pressure distribution in the inviscid flow at $x = 2.032$ meters (80 in.) obtained from this calculation is shown in figure 4. The resulting wavy distribution is similar to the data, and indicates that the observed variations in the inviscid flow are caused by the overexpansion in the upstream core flow (fig. 5). These relatively small variations in the inviscid flow (fig. 4) are believed to have little effect on the wall boundary-layer development.

Wall and free-stream static pressures.- Measured values of wall static-to-total pressure ratios and calculated values of free-stream static-to-total pressure ratios at $x = 2.083$ meters (82 in.) are shown in figure 6. The values of the calculated free-stream static pressures were obtained from the isentropic relation:

$$\frac{p_e}{p_o} = \left(1 + \frac{\gamma - 1}{2} M_e^2\right)^{-\frac{\gamma}{\gamma - 1}}$$

where $M_e$ is obtained from the isentropic relation between free-stream pitot pressure and settling-chamber pressure:

$$\frac{p_{t,2}}{p_o} = \left[\frac{(\gamma + 1)M_e^2}{(\gamma - 1)M_e^2 + 2}\right]^{\frac{\gamma}{\gamma - 1}}\left[\frac{\gamma + 1}{2\gamma M_e^2 - (\gamma - 1)}\right]^{\frac{1}{\gamma - 1}}$$
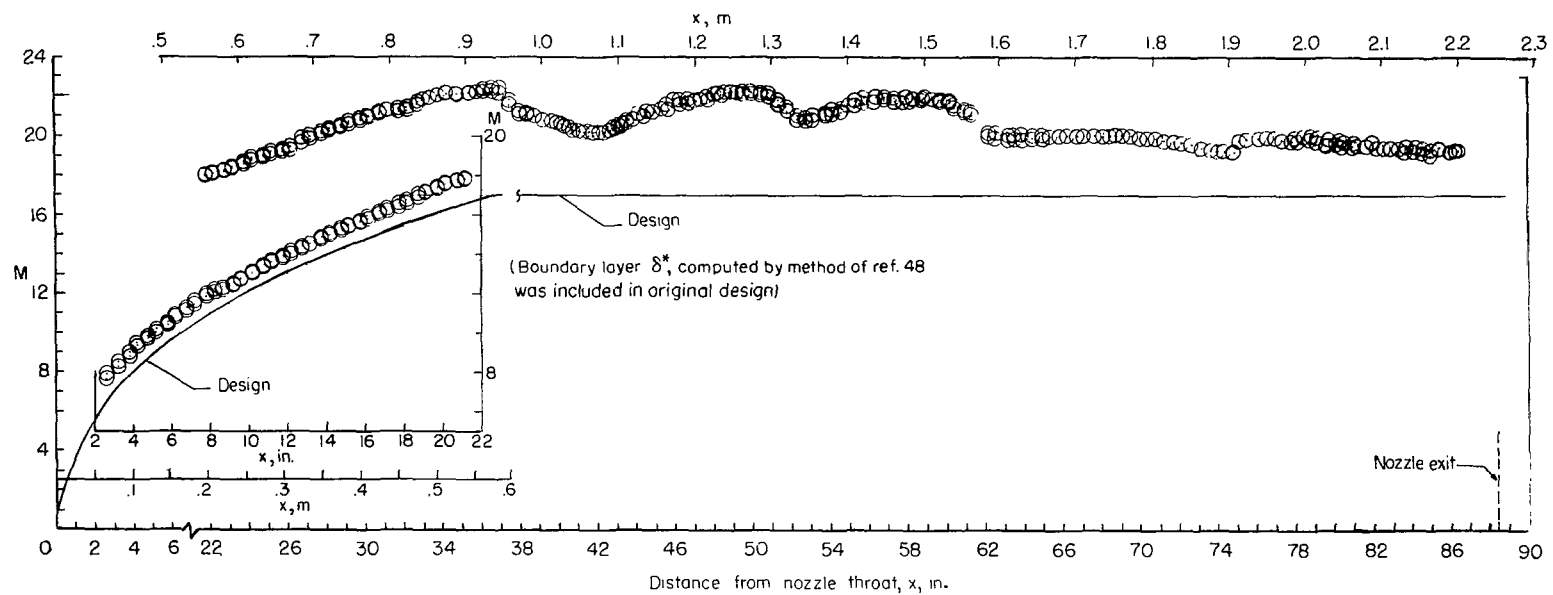
Figure 5.- Mach number distribution along tunnel center line. Data were obtained at nominal stagnation conditions of $p_0 \approx 3450$ N/cm$^2$ (5000 lb/in$^2$) and $T_0 \approx 1670$ K (3000° R).
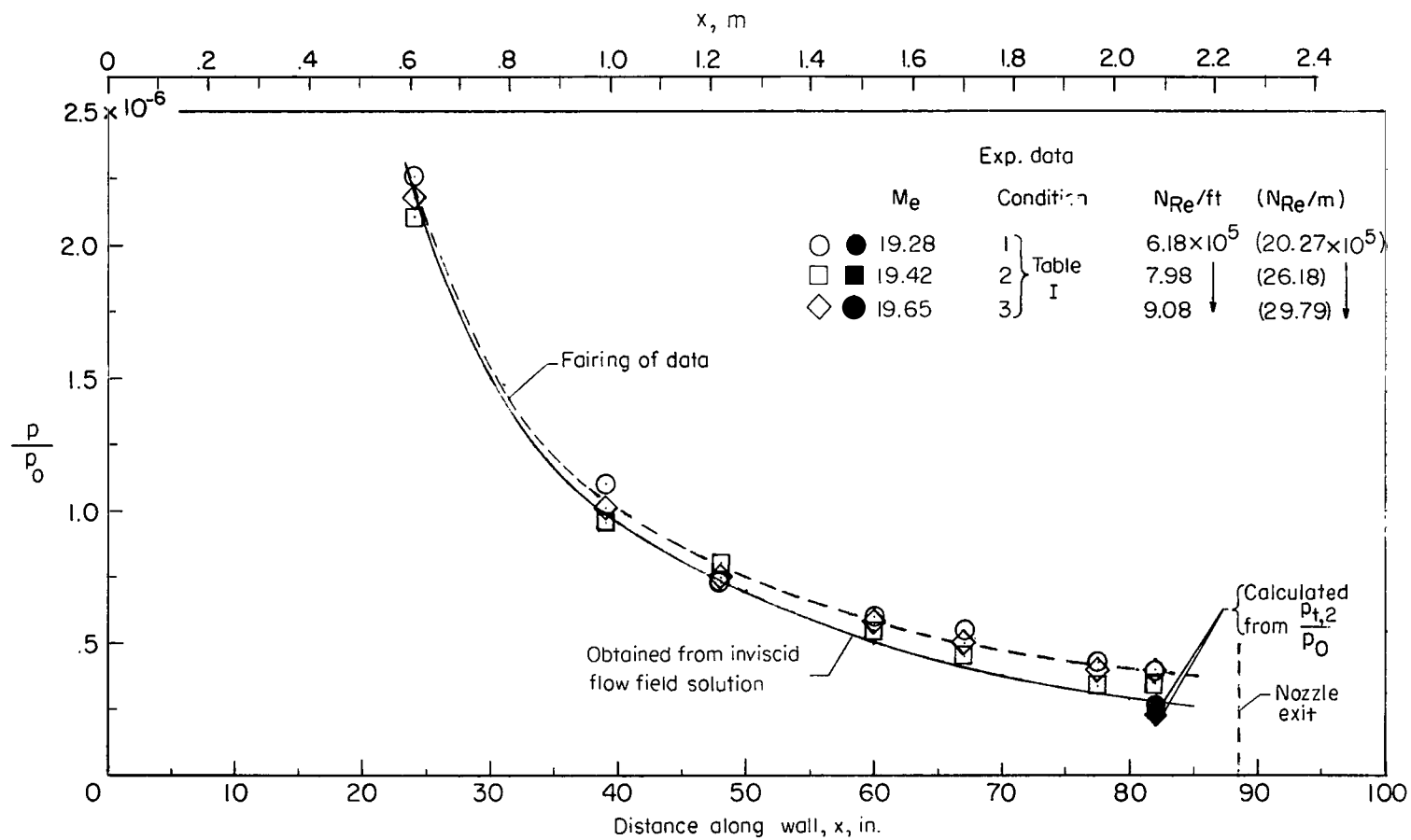
Figure 6.- Distribution of wall static pressures. Solid symbols are for static pressure computed from measured stream pitot pressures.

There is a significant difference between the measured wall pressures and calculated static pressures shown in figure 6. These results are different from previous lower Mach number results (for example, refs. 12 and 19), where the agreement between calculated free-stream and measured wall static pressures was found to be good. However, investigation of nozzle-wall boundary layers in helium at Mach numbers from 20 to 47 (refs. 11 and 16) indicated that wall static pressures were larger than stream static pressures.

Nozzle-wall pressures measured at several locations ahead of the survey station are also shown in figure 6. Included for comparison in the figure are ratios of stream static pressure to total pressure, shown as the solid line, obtained from the same inviscid-flow-field solution described in the preceding section. These values were obtained by interpolation in the computed characteristics mesh at the distances from the nozzle center line of $(r_w - \delta)$ where $\delta$ was the boundary-layer thickness computed by the finite-difference method of reference 5. (Solution no. 2 was used for this purpose. The computing procedure and inputs used for this solution are discussed in subsequent sections herein.) These values of static pressure tend to approach the measured wall pressures upstream of $x = 102$ centimeters (40 in.). The value at $x = 2.083$ meters (82 in.) is in good agreement with values obtained from measured pitot pressures at this station.

The magnitude of the streamwise pressure gradient upstream of the survey station from $x = 1.53$ to 2.04 meters (60 to 80 in.) is approximately $(3.54 \times 10^{-7})p_o$ per meter or $(0.9 \times 10^{-8})p_o$ per inch. The pressure drop across the boundary layer as indicated by the difference between the measured wall static values at $x = 2.083$ meters (82 in.) and the computed free-stream values (figs. 6 and 7) is about $(0.15 \times 10^{-6})p_o$. The magnitude of the normal pressure gradient across the 10.2-centimeter (4-in.) boundary layer is then roughly $(1.57 \times 10^{-6})p_o$ per meter or $(4 \times 10^{-8})p_o$ per inch or about four times larger than the streamwise pressure gradient. Hence, it might be expected that the normal pressure gradient could have at least as large an effect on the boundary-layer structure as the streamwise pressure gradient. The difference between the measured wall static pressures and computed free-stream static pressures may be caused by upstream disturbances, by turbulent velocity fluctuations, or by the inviscid-flow expansion that is present in all nozzle flows. If the latter mechanism affects the normal static-pressure gradients within the boundary layer, the pressure at the wall should be above the pressure near the edge of the boundary layer, as indicated by the results shown in figure 6.

Static-pressure profiles.- Static-pressure distributions across the boundary layer obtained from measurements with a static-pressure probe and from various computations are shown in figure 7(a). Consider first the static-pressure distribution (shown as the dashed line in fig. 7(a)) from the inviscid-flow-field calculation described previously. The aforementioned trend of increasing static pressure as the wall is approached is
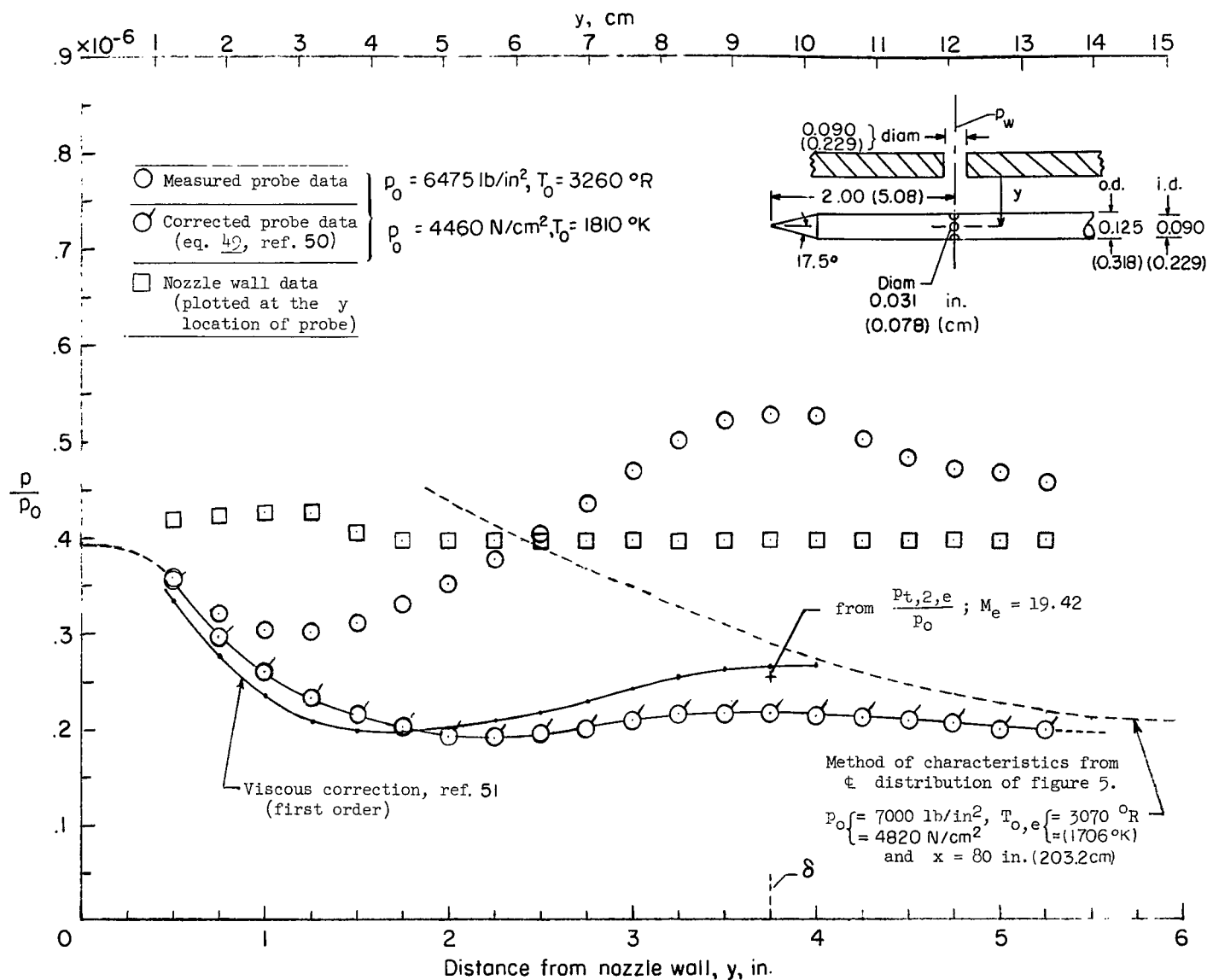
(a) Comparison of measured and corrected static pressures with wall and free-stream values.

Figure 7.- Distribution of static pressure across the boundary layer. Linear dimensions are given in inches (parenthetically in centimeters).

| | $M_e$ | $\gamma$ | $p_0$, psia $(N/cm^2)$ | $T_0$, °R (°K) | $T_w/T_0$ | $\delta$, in.(cm) | Ref. |
|---|---|---|---|---|---|---|---|
| O | 21.6 | 5/3 | 2100(1448) | 540(300) | ~1.0 | 6.00(15.2) | 11 |
| □ | 19.42 | 7/5 | 6475(4464) | 3260(1811) | 0.166 | 3.75(9.5) | Present |

Solid symbols for measured $p_w$
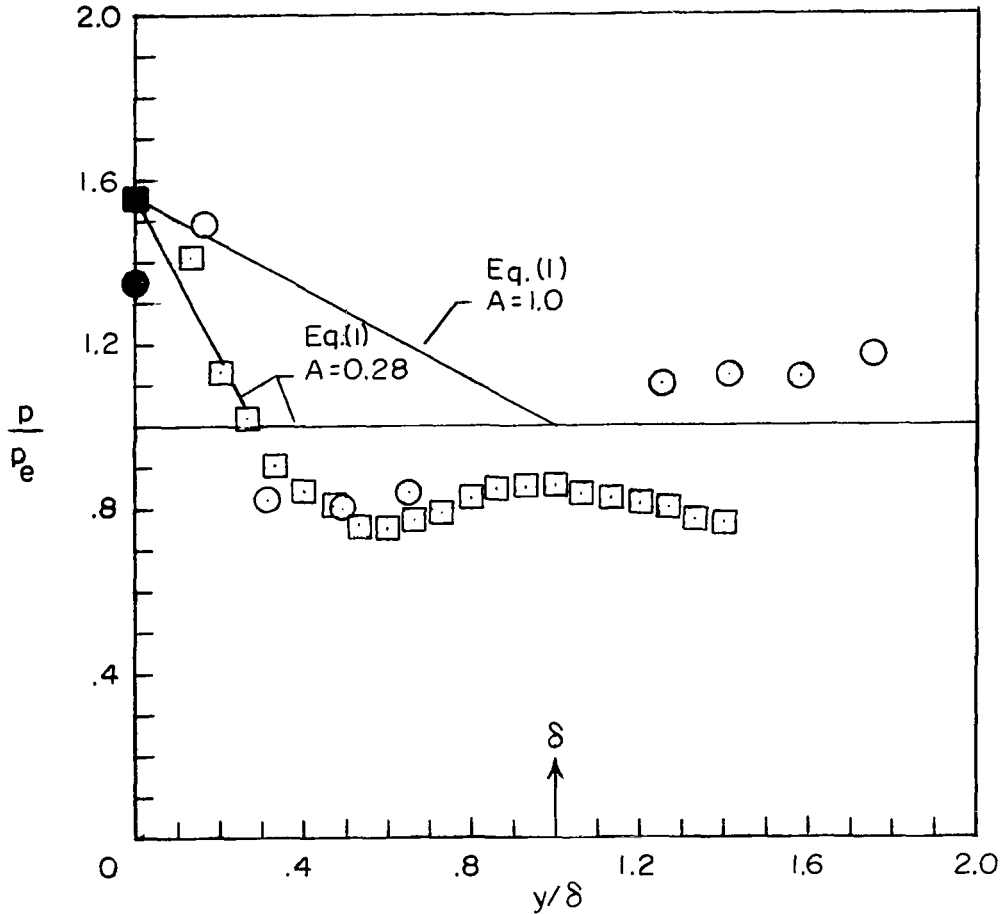


(b) Comparison of present static-pressure data with that of reference 11.

Figure 7.- Concluded.

indicated by the inviscid-flow calculation which was based on the center-line Mach number distribution of figure 5.

Also shown in figure 7(a) as an indication of wall-interference effects caused by the static probe are the values of the wall static pressure (measured at the wall orifice) as recorded for each location of the static probe as it was moved across the boundary layer. It is apparent that the wall static pressures are affected by the static-pressure probe when it is as far from the wall as 3.8 centimeters (1.5 in.), whereas the pitot-probe interference

had practically disappeared when the latter probe was 2.29 centimeters (0.9 in.) from the wall (fig. 2). As mentioned previously, these disturbed values of wall static pressures have not been used in any data-reduction procedures.

Static pressures measured across the boundary layer with a static-pressure probe at x = 2.083 meters (82 in.) are also shown in figure 7(a). The nominal stagnation conditions for these data are shown in the figure. A sketch of the static probe and its location with respect to the nozzle-wall orifice is shown in the figure. Four orifices were located 5.083 centimeters (2 in.) downstream of the tip and 90° apart around the probe circumference to reduce angle-of-attack effects. The accuracy and reliability of the data may be severely limited because of the large Mach number gradients in the boundary layer. The resulting change in Mach number across the 0.3180-centimeter-diameter (1/8-in.) probe was approximately 0.75. Nevertheless, the measured static-pressure data were corrected for bluntness and viscous induced pressure effects by the method of reference 50 (eq. (49) from ref. 50). No transverse curvature effects were included in the two-dimensional correction of reference 50. As a first approximation, the local Mach numbers used in this method were computed from the corrected pitot pressures (fig. 4) and the computed free-stream static pressure since the viscous induced corrections would be the largest in the outer part of the boundary layer where local Mach numbers are large. The local values of $T_t$ (from measurements corrected for radiation and conduction losses) through the boundary layer were also used. The surface temperature of the static-pressure probe was estimated by assuming a linear variation with y between assumed values for the ratio of probe temperature to free-stream total temperature of 0.2 at y = 0 and 0.6 at y = 9.53 centimeters (3.75 in.).

The resulting corrected static-pressure data shown in figure 7(a) indicate a trend of increasing pressure as the wall is approached. The same general trend is also indicated by the inviscid calculation but the latter distribution is displaced outwards from the wall by about 5.08 centimeters (2 in.). Also shown for comparison is a viscous correction to the measured data utilizing the first-order term of an empirical expression obtained from reference 51. The second-order term of this reference was obtained for a static-pressure probe similar to the present one but with a maximum $\overline{\chi}$ value of only 1.4. Hence, this second-order correction was not used herein since the present $\overline{\chi}$ values were about 14. The important point here is that the corrected static pressures at δ (y ≈ 9.53 centimeters (3.75 in.)) are in reasonable agreement with the value computed from the measured $p_{t,2}/p_o$, and also with the values from the inviscid-flow calculation. It is concluded on the basis of these results that there is a significant increase in static pressure from the edge of the boundary layer to the wall.

The exact distribution of static pressure across the boundary layer cannot be determined from these data, because of possible wall-interference effects for
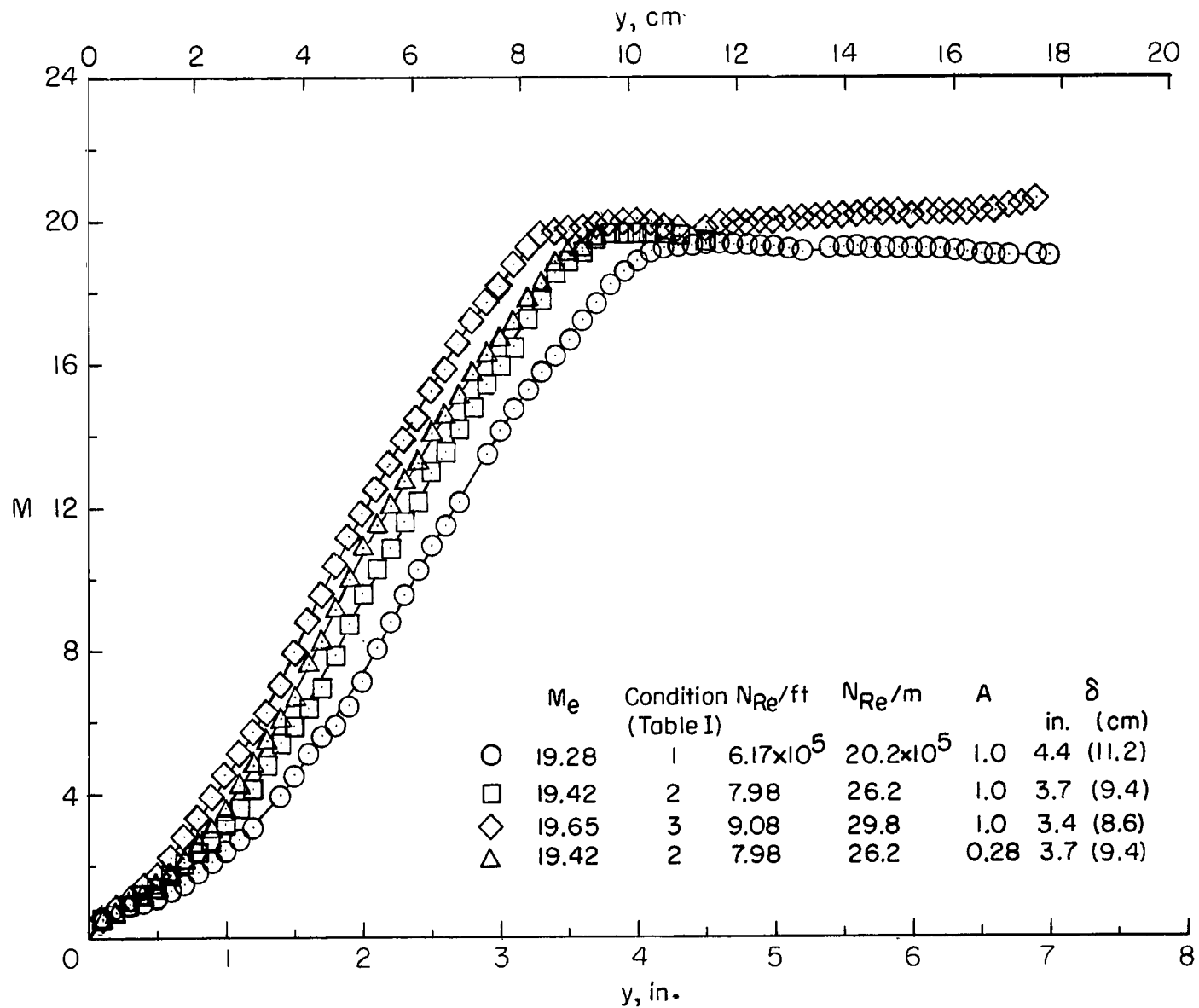
y $\lessgtr$ 3.81 centimeters (1.5 in.) and unknown effects of the Mach number gradient across the boundary layer. Another source of uncertainty is the thermal-diffusion effect on the static-pressure measurement. Estimates by the method of reference 36 indicate that the thermal-diffusion effect would increase the measured pressures by at most 3 percent for the range of probe wall temperatures utilized above in the viscous interaction correction. Because of these uncertainties, linear distributions between the measured wall value and the value inferred at $y = \delta$ from measured $p_{t,2}/p_0$ have been used to obtain all of the following computed boundary-layer profiles. (The wall and stream static pressures used are given in table I.) This distribution is specified by the relations

$$
\left.
\begin{aligned}
\frac{p}{p_0} &= \frac{p_w}{p_0} - \frac{1}{A}\left(\frac{p_w}{p_0} - \frac{p_e}{p_0}\right)\frac{y}{\delta} && (0 \leq y \leq A\delta) \\
\frac{p}{p_0} &= \frac{p_e}{p_0} && (y \geq A\delta)
\end{aligned}
\right\}
\tag{1}
$$

Values of A have been limited to 1.0 and 0.28 which give, respectively, a simple linear distribution from $y = 0$ to $\delta$, and a two-step linear distribution that approximates the data somewhat better. These distributions are compared with the corrected data in figure 7(b) where $p/p_e$ is plotted against $y/\delta$. Shown for comparison are static-pressure measurements across the boundary layer on the wall of a helium tunnel at Mach number 21.6 (ref. 11). The same trend of increasing static pressure as the wall is approached is evident in these data.

Mach number distributions.- The local values of Mach number as computed from the Rayleigh pitot formula with ratios of local pitot pressure to total pressure and ratios of static pressure to total pressure are plotted against y in figure 8. Figure 8(a) shows the Mach number distribution out to about 18 centimeters (7 in.) from the wall as based on corrected pitot pressures (fig. 4) and static pressures from equation (1) with $A = 1.0$ for all three conditions and with $A = 0.28$ for the intermediate condition 2 where $p_0 \approx 4310$ N/cm$^2$ (6250 lb/in$^2$). The maximum effect of these two static-pressure distributions was to change the Mach number by about 1.0 in the central region of the boundary layer. However, because of the previously mentioned uncertainties in the static-pressure distributions, the two-step linear distribution has been used only with the intermediate condition 2 for the purpose of illustrating the possible effects of different static-pressure distributions on the various profile parameters. The Mach number distributions tend to be nearly linear for $y > 2.54$ centimeters (1 in.) and the slope decreases with decreasing total pressure.

Shown in figure 8(b) are the local values of Mach number in the wall region ($y < 1.27$ centimeters (0.5 in.)) for condition 2 (table I) as obtained with both the corrected and uncorrected pitot pressures. The solid faired line is used to evaluate

The table within the figure:

| $M_e$ | Condition (Table I) | $N_{Re}/ft$ | $N_{Re}/m$ | A | $\delta$ in. (cm) |
|---|---|---|---|---|---|
| ○ 19.28 | 1 | $6.17 \times 10^5$ | $20.2 \times 10^5$ | 1.0 | 4.4 (11.2) |
| □ 19.42 | 2 | 7.98 | 26.2 | 1.0 | 3.7 (9.4) |
| ◇ 19.65 | 3 | 9.08 | 29.8 | 1.0 | 3.4 (8.6) |
| △ 19.42 | 2 | 7.98 | 26.2 | 0.28 | 3.7 (9.4) |

(a) Distribution across boundary layer and adjacent free stream.

Figure 8.- Mach number distributions across the boundary layer.  Equation (1) used for static pressures.
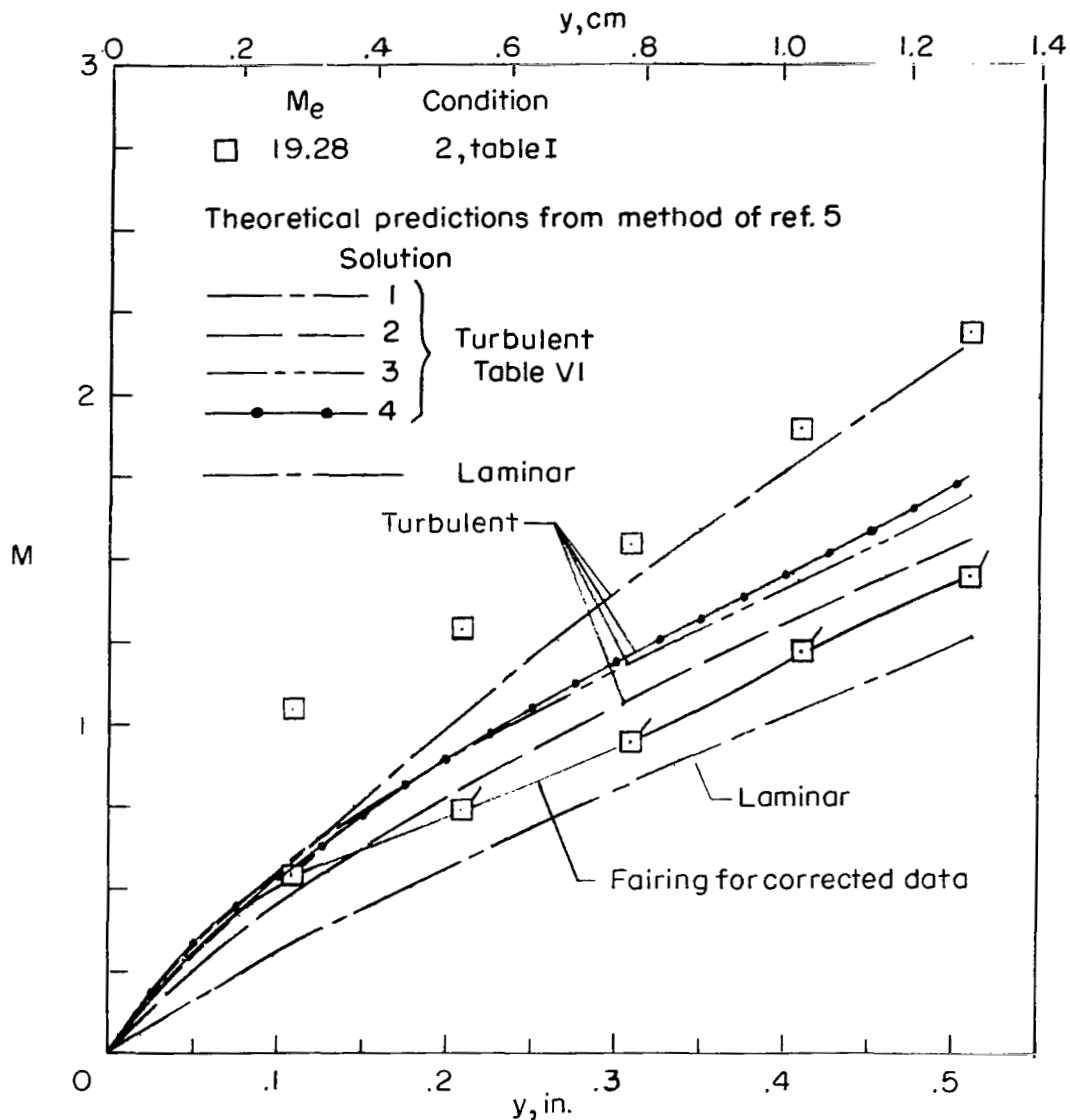
(b) Variation of local Mach number in the near-wall region from both uncorrected and corrected pitot pressures. A = 1.0. Flagged symbols show corrected values.

Figure 8.- Continued.

experimental skin friction as indicated in a subsequent section of this report. This line was faired through all data points and therefore represents the best estimate of Mach number distribution if equal "weight" or reliability is assigned to all data points. Comparison of Mach numbers from corrected and uncorrected pitot pressures shows, however, that the rarefaction effects cause larger percentage corrections in Mach number as the wall is approached. The skin friction (which is proportional to $\partial M/\partial y$) would therefore be strongly influenced by uncertainties in both static pressures and pitot pressures.

Predicted Mach number distributions from the finite-difference method of reference 5 are also shown in figure 8(b). These theoretical results will be discussed in detail in a subsequent section and are included here to illustrate the significant differences between predictions of skin friction for laminar and turbulent boundary layers.

In order to obtain some indication of the validity of the pitot-pressure corrections, some additional pitot-pressure surveys were made in the outer part of the boundary layer for y > 5.08 centimeters (2.0 in.) with large circular tubes of 0.318-centimeter (0.125-in.) diameter. The results are shown in figure 8(c) where the local Mach numbers computed from the pitot pressures measured with the large probe and the flattened probe are shown. Comparison of corrected and uncorrected data in the overlap region of 7.6 > y > 5.1 centimeters (3.0 > y > 2.0 in.) indicates that while the corrections are generally of opposite sign for the two different tubes, the net scatter in the data is reduced. This reduction in data scatter indicates that the corrections are satisfactory for the limited range of conditions within the overlap region. Also, comparison of the corrected data from the large circular probe and the small flattened probe indicates that there was no significant effect of the Mach number gradient on the pitot pressure from the large probe for y > 5.6 centimeters (2.2 in.). Since the Mach number gradient is nearly linear, it can be concluded that the large probes could have been used over most of the boundary layer in the present investigation, however, all data presented in the tables and other figures are from the small flattened probe.

Total-temperature surveys.- The ratios of local stagnation temperature to measured settling-chamber temperatures are given in figure 9. Figures 9(a) and 9(b) show, respectively, the uncorrected and corrected data plotted against y. (See appendix A for details of the method used to obtain total-temperature corrections.) The nominal test conditions shown in figure 9 were taken from the temperature-survey tests (table I). These data are the first published experimental measurements, known to the present authors, of stagnation-temperature profiles in cold-wall turbulent boundary layers for Mach numbers as high as 19 in air or nitrogen. Comparisons between theoretical calculations and some of the present data (without pitot-pressure and final temperature corrections) have previously been made in references 5 and 47. The only other high Mach number (M $\gtrsim$ 19) data published to date have been in helium (refs. 11, 16, 26, and 27).

The thermal boundary-layer thicknesses for the present data (shown in fig. 9(a)) are somewhat larger than the thicknesses based on pitot-pressure data (see fig. 4) also shown in the figure. This same result for relative thermal and pitot-pressure boundary-layer thicknesses has been observed in other experiments (private communication from the Von Karman Gas Dynamics Facility, Arnold Engineering Development Center). The wall temperature measured near x = 2.083 meters (82 in.) where the nozzle-wall section was water cooled was about 300 K (540° R) which gives a ratio of wall-to-stream
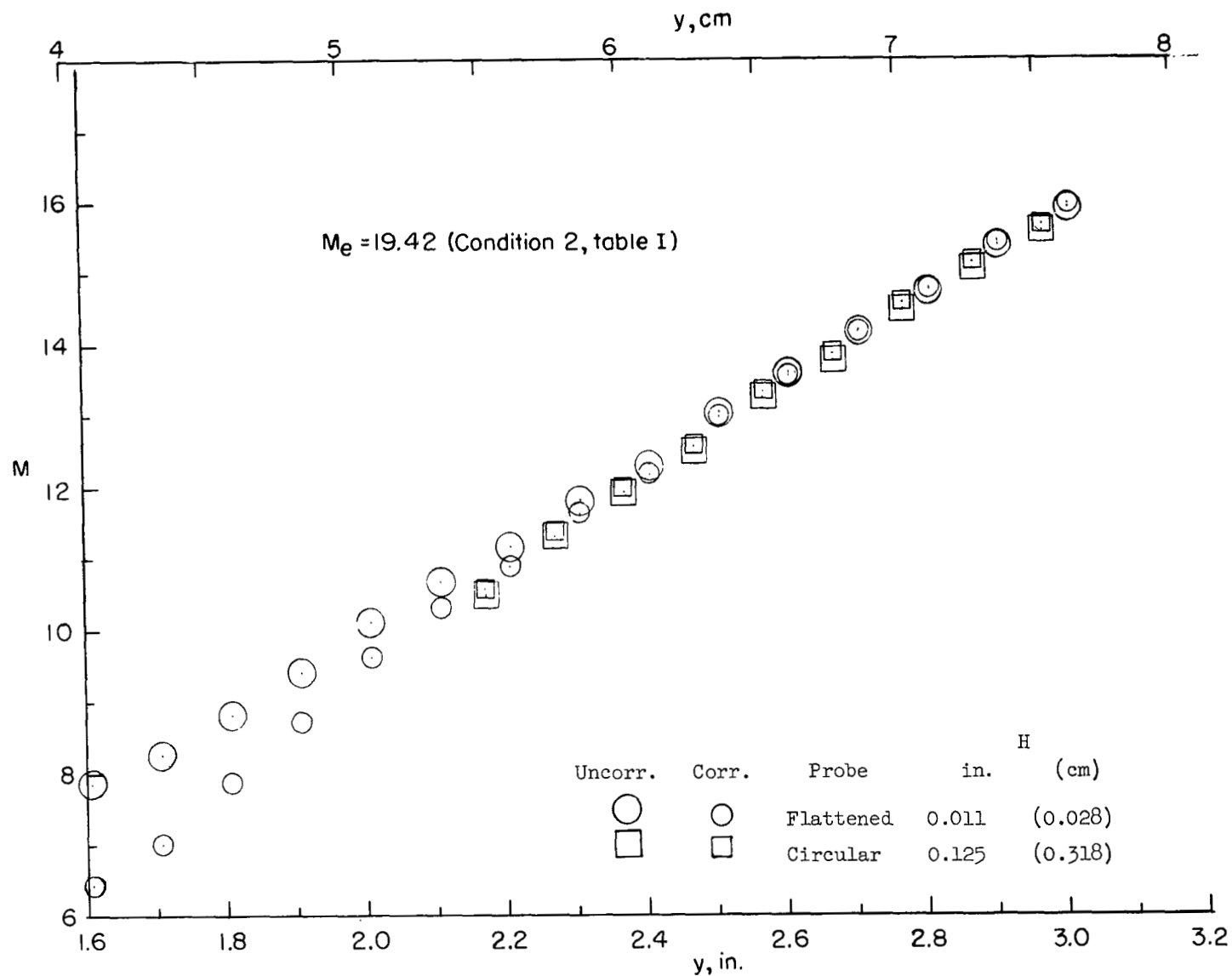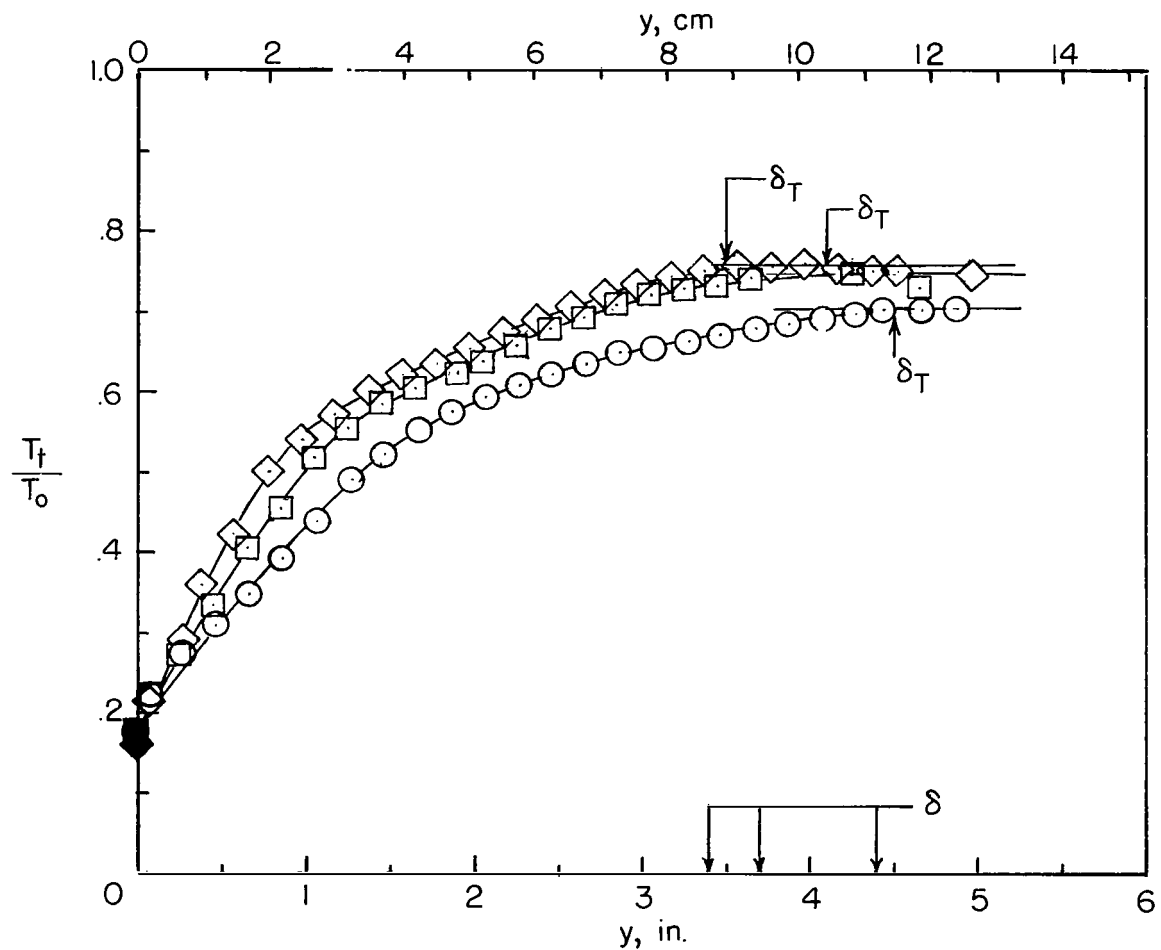
(c) Comparisons of local Mach number from small flattened pitot tubes (fig. 1) and large circular tubes.  A = 1.0.

Figure 8.- Concluded.

| | $M_e$ | Condition (Table I) | $N_{Re}/ft$ | $N_{Re}/m$ | $T_w/T_{0,e}$ | $\delta_T$, in. (cm) | $\delta$, in. (cm) |
|---|---|---|---|---|---|---|---|
| ○ | 19.28 | 1 | $5.78 \times 10^5$ | $18.96 \times 10^5$ | 0.177 | 4.5 (11.4) | 4.4 (11.17) |
| □ | 19.42 | 2 | 8.84 | 29.00 | .177 | 4.1 (10.4) | 3.7 (9.4) |
| ◇ | 19.65 | 3 | 9.16 | 30.05 | .163 | 3.5 (8.9) | 3.4 (8.6) |

Solid symbols for $T_w/T_{0,e}$
$T_w = 540\ ^\circ R$ (300 $^\circ K$)



(a) Uncorrected data.

Figure 9.- Distribution of total temperatures through the boundary layer.

stagnation temperature of about 0.17. No upstream wall temperatures were measured for the present tests. However, the wall temperatures probably do not exceed 330 K (600° R) for the water-cooled section of the nozzle (which extends from the end of the throat section at x = 14.5 centimeters (5.7 in.) (ref. 30) to the exit of the nozzle) since the heating rates are small downstream of the throat section.

Comparisons of the uncorrected and corrected data indicate that the corrections caused large changes in both the magnitude and profile shapes of total temperature. Comparisons of theoretical predictions from the methods of references 5 and 52 with the corrected data (fig. 9(b)) again indicate that the boundary layer is not laminar. Further implications of the theoretical predictions will be discussed in a subsequent section of the report.

The corrected total-temperature data are plotted as a function of $y/\delta_T$ in figure 9(c) to show the consistency in profile shapes of these data. The "hump" in the profile data at $y/\delta_T \approx 0.3$ is present in all the corrected data and may be caused by or associated with the thick viscous sublayer which extends out to $y/\delta_T \approx 0.2$ as indicated in the figure. Since the uncorrected data (fig. 9(a)) show little, if any, evidence of such a hump, it is apparent that the nonlinear effects of heat conduction and radiation losses on the indicated probe temperatures have smoothed out and removed the hump.

## Computed Boundary-Layer Profiles and Parameters

The velocity profiles through the boundary layer were obtained by using the Mach number (fig. 8(a)) and total-temperature profiles (fig. 9(b)). With the assumptions of an ideal gas (p = $\rho$RT) and constant ratio of specific heats, the velocity profiles were then calculated from the equation

$$\frac{u}{u_e} = \frac{M}{M_e}\sqrt{\frac{T}{T_e}} \tag{2}$$

where

$$T = T_t\left(1 + \frac{\gamma - 1}{2}M^2\right)^{-1} \tag{3}$$

and $\gamma = 7/5$. The Mach number values used to calculate the velocities were taken from fairings of the data in figure 8(a) at values of y corresponding to the total-temperature data points of figure 9. The local mass flow was calculated from the relation

$$\rho u = \sqrt{\frac{\gamma}{R}}\frac{pM}{\sqrt{T}} \tag{4}$$

where p was computed from equation (1).

38
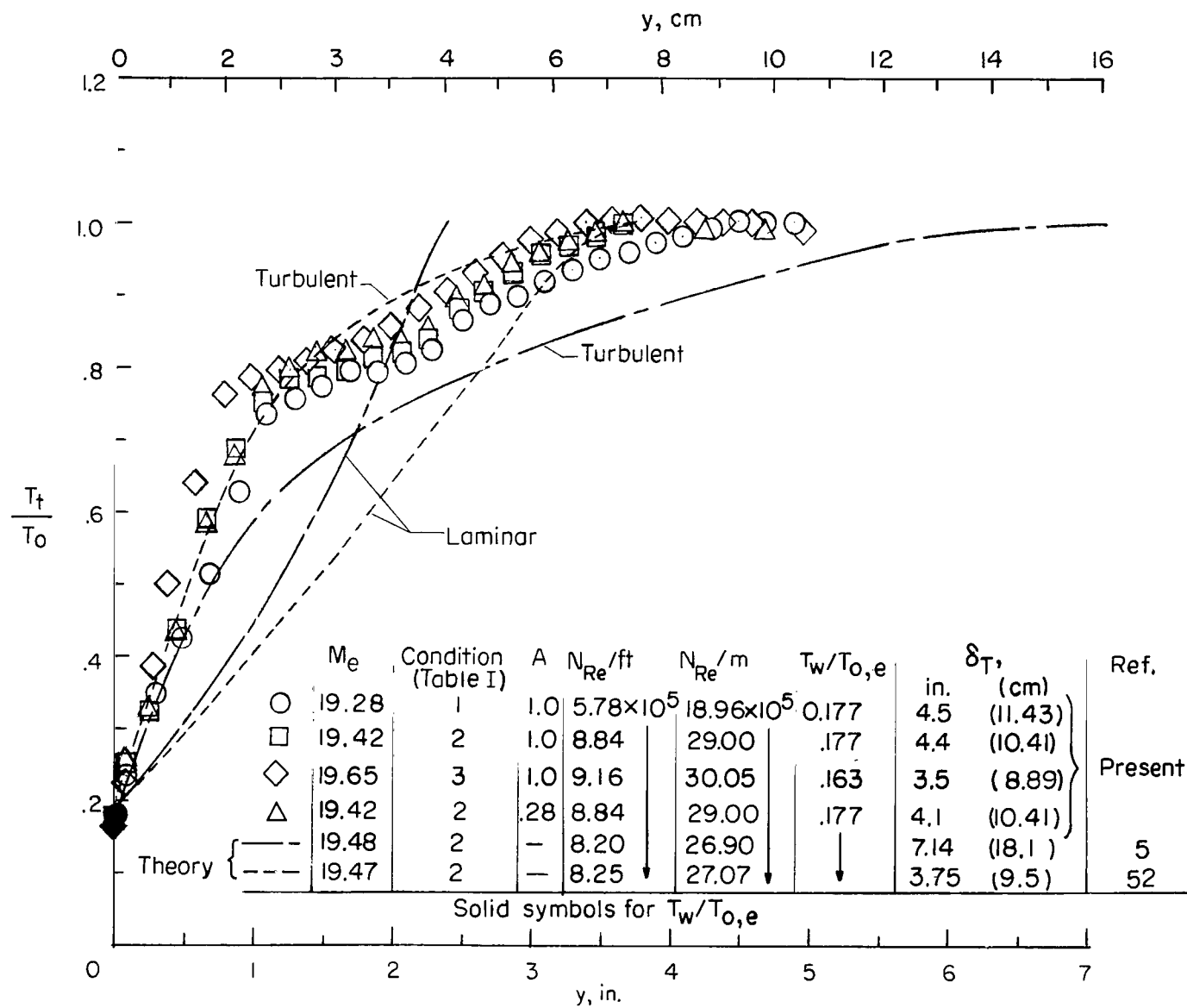
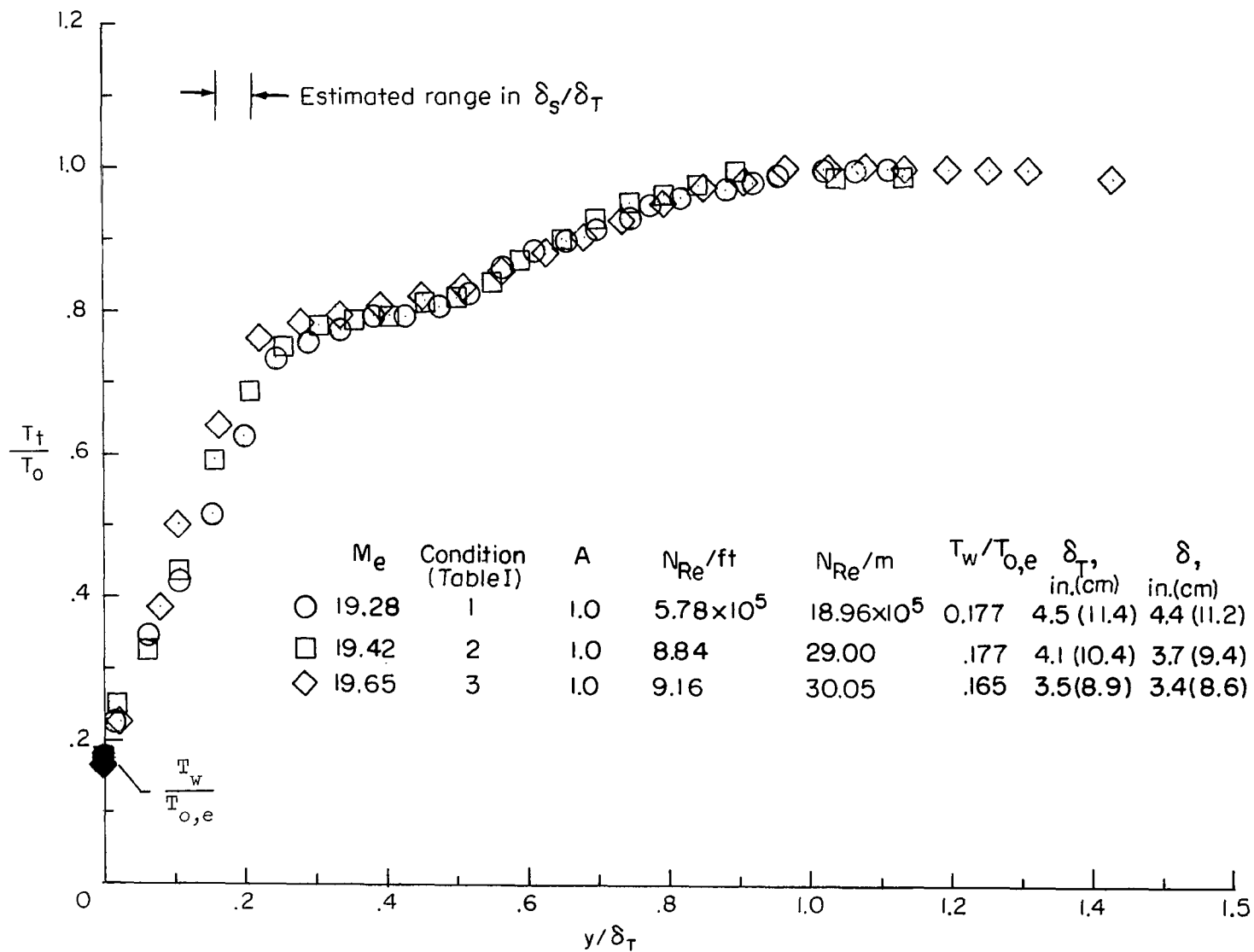(b) Corrected data and theoretical predictions.

Figure 9.- Continued.

(c) Corrected data as a function of $y/\delta_T$.

Figure 9.- Concluded.

The displacement-thickness factor that appears in the integral equations for an axisymmetric boundary layer is

$$\frac{\delta^*}{\delta} = \int_0^1 \left(1 - \frac{\rho u}{\rho_e u_e}\right)\left(1 - \frac{y \cos \beta}{r_w}\right) d\left(\frac{y}{\delta}\right) \tag{5}$$

Similarly, the boundary-layer momentum thickness is

$$\frac{\theta}{\delta} = \int_0^1 \frac{\rho u}{\rho_e u_e}\left(1 - \frac{u}{u_e}\right)\left(1 - \frac{y \cos \beta}{r_w}\right) d\left(\frac{y}{\delta}\right) \tag{6}$$

The values of $\delta^*$ and $\theta$ for the present tests were obtained by numerical integration of equations (5) and (6).

The values of skin friction for the present tests were obtained from the Mach number gradient at the wall by using the formula

$$c_f = \frac{\tau_w}{\frac{1}{2}\rho_e u_e^2} = \frac{2\mu_w a_w}{\gamma p_e M_e^2}\left(\frac{\partial M}{\partial y}\right)_w \tag{7}$$

Values of $(\partial M/\partial y)_w$ were obtained from fairings of Mach number data near the wall similar to the solid line fairing shown in figure 8(b) for condition 2 (table I). However, the values of $c_f$ obtained from such fairings must be considered as only approximate estimates because of the large pitot-pressure corrections required in the wall region, uncertainties in the static pressures, and the relatively large spacing between data points near the wall.

The Reynolds analogy factor has also been estimated from the total temperature and Mach number gradients at the wall by the formula

$$\frac{2N_{St}}{c_f} = \frac{T_{t,e} u_e}{(T_{aw} - T_w)N_{Pr,w} a_w}\left(\frac{\partial}{\partial y}\frac{T_t}{T_{t,e}}\right)_w\left(\frac{\partial M}{\partial y}\right)_w^{-1} \tag{8}$$

and

$$\frac{T_{aw} - T_e}{T_{t,e} - T_e} = 0.9$$

was assumed. While the results obtained from equations (7) and (8) are considered preliminary due to the uncertainty in the experimental values of the total temperature and Mach number slopes at the wall, they are included here as a matter of interest and for comparison with previous data and theoretical predictions. The numerically integrated

values of $\delta^*/\delta$ and $\theta/\delta$ from equations (5) and (6) and of $c_f$ and $2N_{St}/c_f$ obtained from equations (7) and (8) are given in table V(a).

## COMPARISONS OF EXPERIMENTAL RESULTS WITH
## THEORETICAL PREDICTIONS

The corrected pitot-pressure and total-temperature data have been used to compute the profile parameters $u/u_e$, $M/M_e$, and $\bar{\theta}$ and the results may be compared with theoretical predictions in figure 10. Predicted values of $M$ and $T_t/T_0$ are also shown in figures 8(b) and 9(b) and predicted values of boundary-layer-thickness parameters, skin friction, and Reynolds analogy factors are given in table V(b) where the corresponding experimental values at the intermediate pressure conditions are given for comparison. As previously discussed, the local static pressures computed from equation (1) have been used to calculate the profile data points with $A = 1.0$ except for the intermediate stagnation pressure run where $A = 0.28$ was also used. Before further discussion of comparisons between experimental results and theoretical predictions, the principal ingredients of the theoretical calculations will be presented.

TABLE V.- BOUNDARY-LAYER PARAMETERS

(a) Experimental data

$$\left[x = 2.083 \text{ meters } (82 \text{ in.})\right]$$

| $M_e$ | Average $N_{Re}/m$ | Average $N_{Re}/ft$ | $\delta$ | | $\delta^*/\delta$ | $\theta/\delta$ | $\delta^*/\theta$ | $(\partial M/\partial y)_w$ | | $c_f$ | $2N_{St}/c_f$ | $\theta$ | | $N_{Re,\theta}$ |
|---|---|---|---|---|---|---|---|---|---|---|---|---|---|---|
| | | | cm | in. | | | | per m | per ft | | | cm | in. | |
| 19.28 | $1.96 \times 10^6$ | $5.98 \times 10^5$ | 11.2 | 4.4 | 0.530 | 0.0159 | 33.4 | 295 | 90 | $9.0 \times 10^{-4}$ | 0.97 | 0.178 | 0.070 | 3490 |
| 19.42 | 2.76 | 8.41 | 9.4 | 3.7 | .492 | .0185 | 26.7 | 240 | 73 | 5.2 | 1.09 | .173 | .068 | 4760 |
| 19.65 | 2.99 | 9.12 | 8.65 | 3.4 | .499 | .0179 | 27.8 | 243 | 74 | 4.3 | 1.06 | .155 | .061 | 4640 |

(b) Comparison of theoretical predictions for turbulent flow
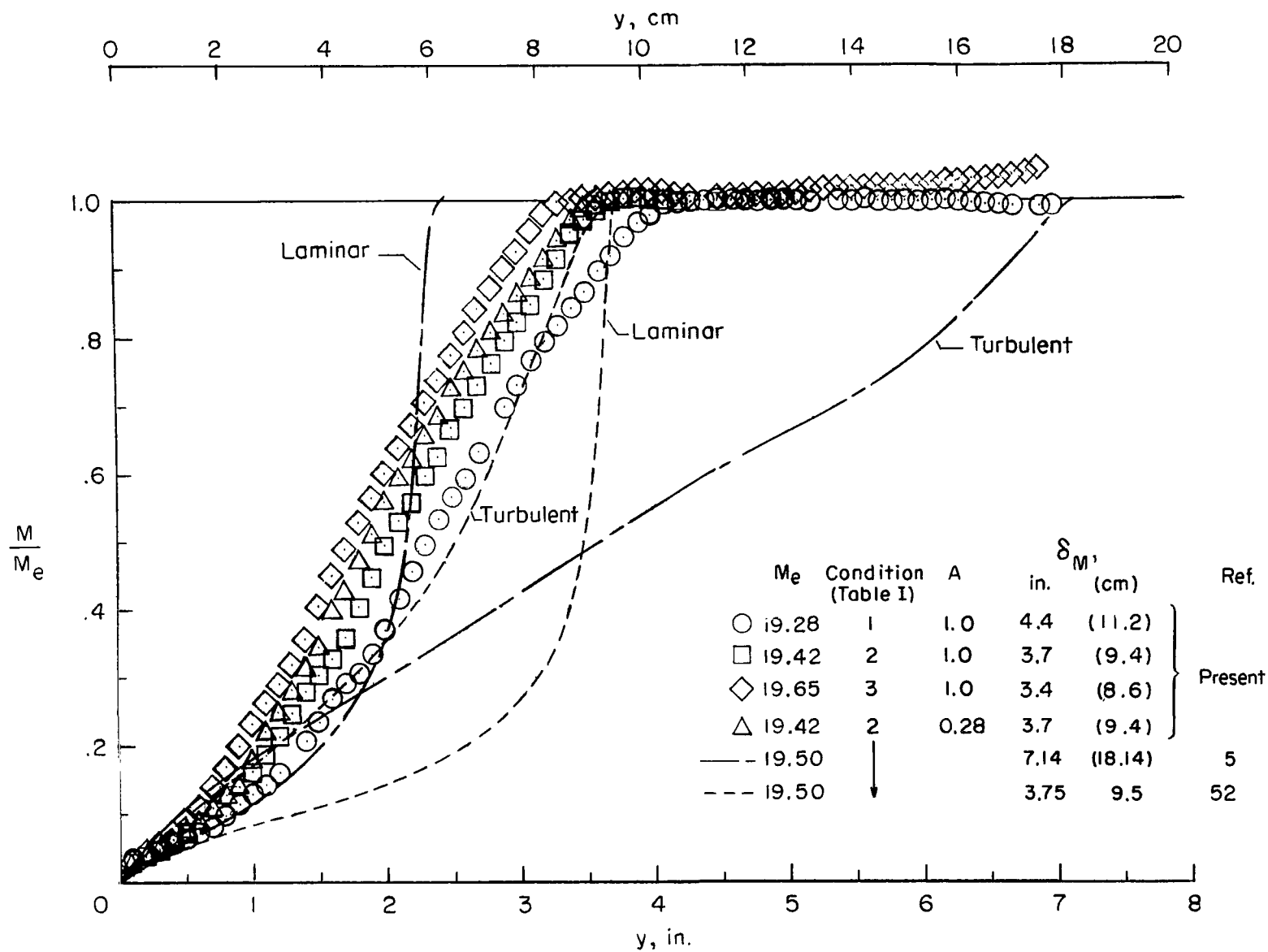with experimental values

$$\left[M_e = 19.48; \quad N_{Re}/m = 2.69 \times 10^6 \ (N_{Re}/ft = 8.2 \times 10^5)\right]$$

| Source | $\delta$ at $M = 0.995$ | | $N_{Re,\delta}$ | $N_{Re,\theta}$ | $\theta$ | | $c_f$ |
|---|---|---|---|---|---|---|---|
| | cm | in. | | | cm | in. | |
| Bushnell and Beckwith (ref. 5) | 18.10 | 7.14 | $4.9 \times 10^5$ | $7.8 \times 10^3$ | 0.29 | 0.114 | $5.2 \times 10^{-4}$ |
| Harris (ref. 52) | 9.53 | 3.75 | 2.57 | 2.70 | .098 | .0385 | 4.64 |
| Experiment | 9.40 | 3.7 | 2.6 | 4.8 | .173 | .068 | 5.2 |
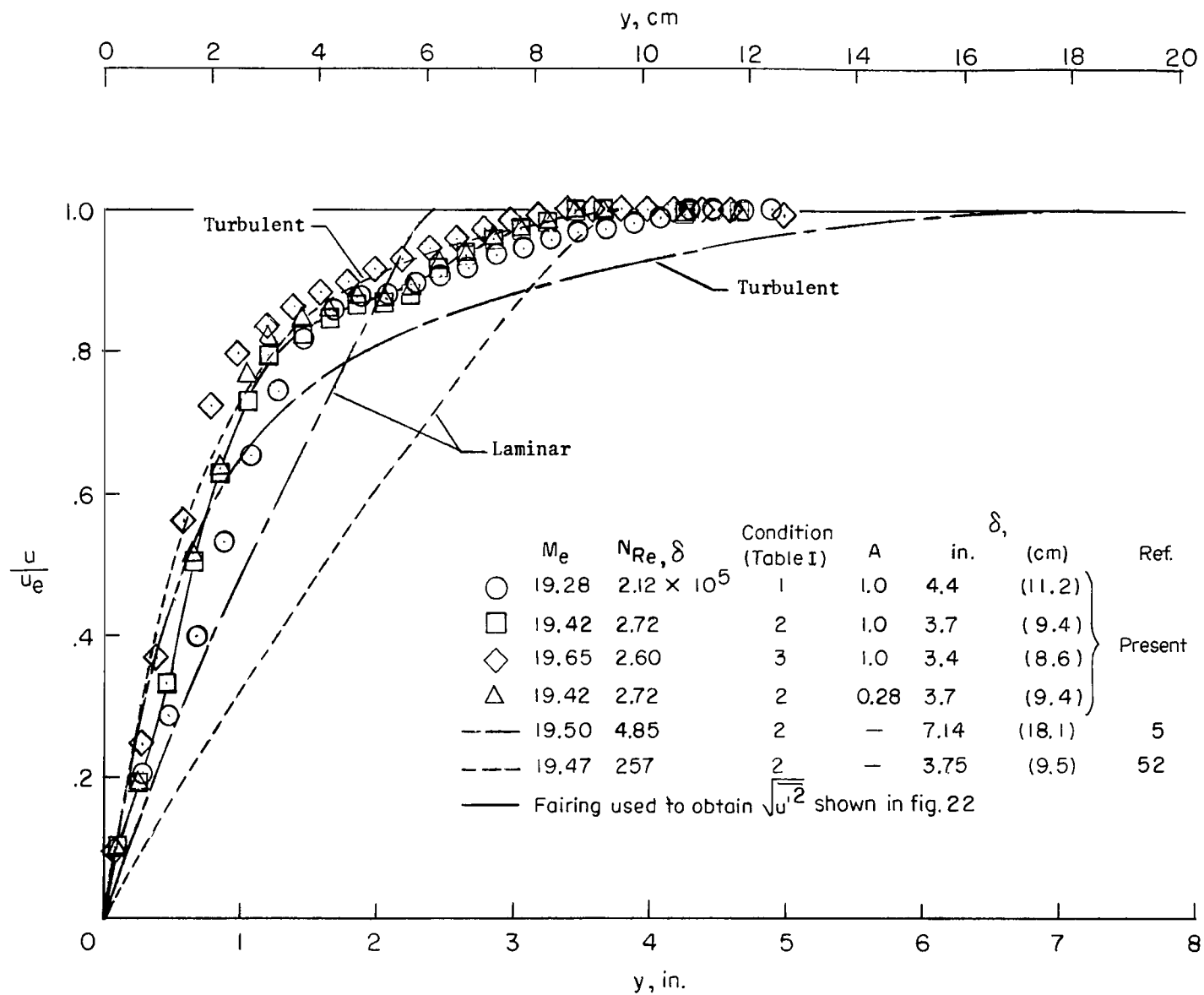
(a) Velocity.

Figure 10.- Comparison of experimental and theoretical profiles.

(b) Mach number.

Figure 10.- Continued.
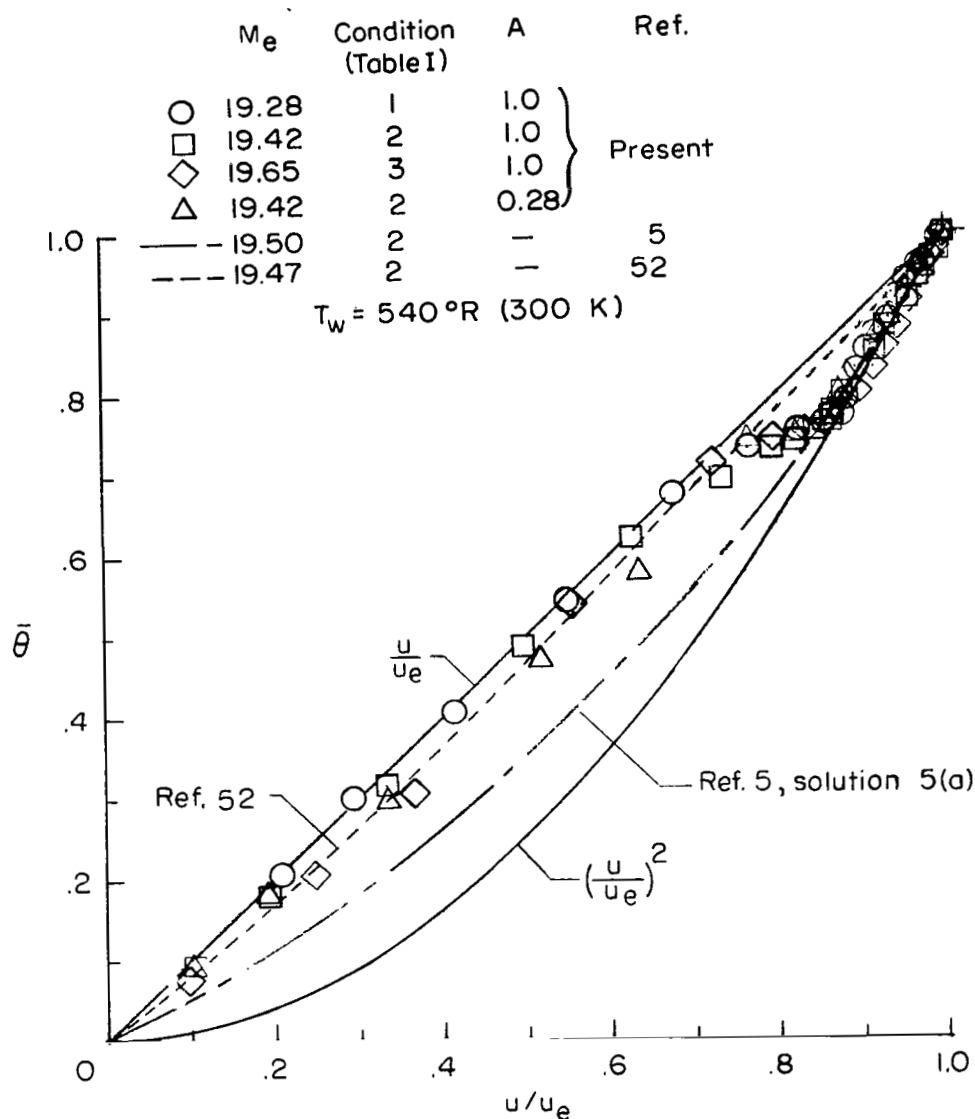
(c) Total-temperature-velocity profile.

Figure 10.- Concluded.

Theoretical Methods and Inputs

The theoretical results shown in figures 9(b) and 10 were calculated for compressible laminar and turbulent boundary layers by two independent theoretical methods. The method of Bushnell and Beckwith (ref. 5) employs a two-point implicit finite-difference procedure. The method of Harris (ref. 52) uses a three-point implicit finite-difference procedure. Both methods solve the mean flow boundary-layer equations and utilize eddy-viscosity and eddy-conductivity (as determined from specified turbulent Prandtl number

distributions) concepts for the turbulent flow solutions. A simple mixing-length approach is used in the method of reference 5. The eddy-viscosity expressions used by Harris (ref. 52) are identical to those of Cebeci and Smith (ref. 53) who used the Prandtl mixing-length relation near the wall and a Clauser eddy-viscosity expression in the far-wall region. The calculation by the method of reference 5 incorporated the complete pressure-gradient history in the entire nozzle with appropriate initial profiles upstream of the throat, whereas the calculation by Harris was for an equivalent flat plate without pressure gradient. Comparison of the results from the equivalent-flat-plate solution with those from the solutions by the method of reference 5 will then provide some indication of the effects of the upstream history of the nozzle flow on local profile shapes near the nozzle exit. The nominal inputs for the flat-plate calculation were $M_e = 19.5$, $p_e = 11.0$ N/m$^2$ (0.0016 lb/in$^2$), and $T_e = 22$ K (40$^O$ R). The inputs used for the method of reference 5 are given in figure 11. The wall temperature is the same as that of reference 5, but the final Mach number at the 2.083-meter (82-in.) station has been increased from 18.2 to 19.5 in accordance with more recent experimental data. The stagnation conditions used in all solutions were $p_O = 4310$ N/cm$^2$ (6250 psia) and $T_O = 1683$ K (3030$^O$ R).

## Discussion of Comparisons

The theoretical results calculated by the method of Harris (ref. 52) were selected from the equivalent flat-plate solution at the streamwise location where $N_{Re, \delta}$ (and hence $\delta$) agreed with experiment. The computed value of $N_{Re, \theta}$ would then agree with the experimental value only if both the Mach number and velocity profiles agreed perfectly with data. Figures 10(a) and 10(b) show that such agreement was not obtained; hence, agreement with the experimental value of $N_{Re, \theta}$ was not obtained. (See table V(b).) The good agreement between predicted skin friction from this solution and the experimental value given in table V(b) is probably fortuitous since the values of $N_{Re, \theta}$ are not in agreement.

The results from the method of reference 5 (figs. 9(b) and 10) were taken from the nozzle calculation at $x = 2.083$ meters (82 in.) corresponding to the experimental survey station. The predicted boundary-layer thickness from the calculation for turbulent flow is almost twice as large as the experimental value, whereas the predicted value of $\delta$ for laminar flow is about 2/3 of the experimental value. The calculated values for turbulent flow of $\theta$, $N_{Re, \delta}$, and $N_{Re, \theta}$ are therefore too large (see table V(b)) and again the agreement in skin friction is fortuitous. $\Big($The theoretical skin-friction values for all solutions were computed with the approximation that $\left(\dfrac{\partial M}{\partial y}\right)_w \approx \dfrac{M}{y}$ evaluated from the solution at $y \approx 0.13$ centimeter (0.05 in.). This evaluation for $(\partial M/\partial y)_w$ was intended to approximate the experimental evaluation which is based essentially on the two or three data points nearest the wall as illustrated in fig. 8(b).$\Big)$ The solutions for
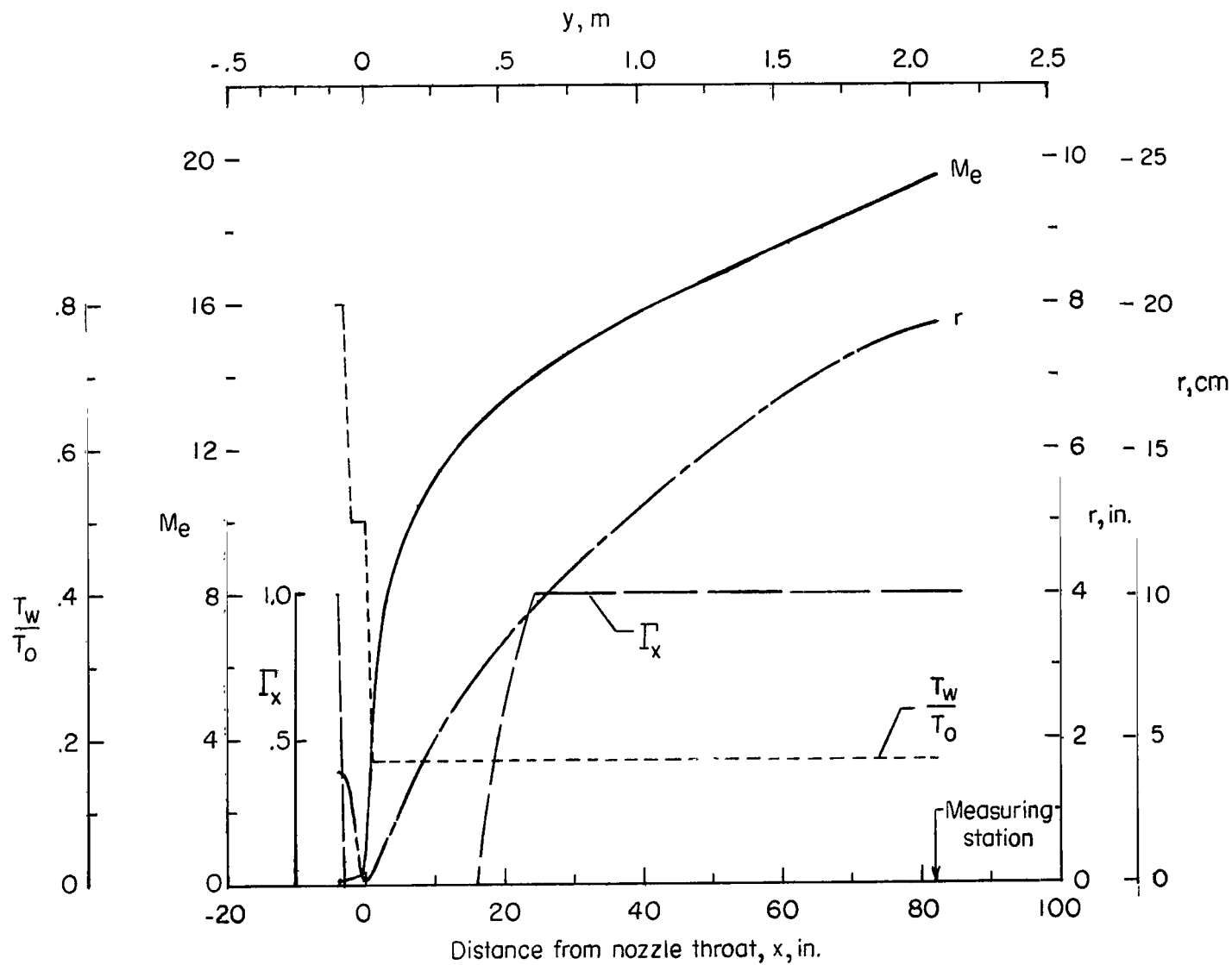
Figure 11.- Boundary conditions and input for nozzle wall boundary-layer calculations by method of reference 5.

this same nozzle flow as reported in reference 5 gave boundary-layer thicknesses from 9.9 to 12.7 centimeters (3.9 to 5.0 in.) depending on the modifications to the eddy viscosity and turbulent Prandtl number functions as well as the input and boundary conditions used. The eddy viscosity and $N_{Pr,T}$ functions used to obtain the profiles shown in figures 9(b) and 10 are identical to those for solution number 5 of reference 5 for which the predicted value of $\delta$ was 12.7 centimeters (5.0 in.). However, the boundary conditions for the present solution were modified downstream of the x = 1.22-meter (48-in.) station, to provide inviscid-flow conditions that are consistent with stagnation conditions 2 (table I) and with the present measurements of stream static pressure. The resulting inputs are compared with values used in the corresponding solutions of reference 5 in the following table:

| Source | $p_o$ | | $\dfrac{p_o\sqrt{2c_pT_o}}{\mu_o}$ | | x = 2.083 meters (82 in.) | | | |
| | | | | | $\rho_e/\rho_o$ | $M_e$ | $\delta$ | |
| | N/cm$^2$ | lb/in$^2$ | per cm | per in. | | | cm | in. |
| Previous data (solution 5, ref. 5) | 4850 | 7040 | $3.15 \times 10^7$ | $0.80 \times 10^8$ | $2.47 \times 10^{-5}$ | 18.2 | 12.7 | 4.98 |
| Present data (figs. 9(b) and 10) | 4310 | 6250 | 2.80 | .71 | 1.93 | 19.5 | 18.1 | 7.14 |

Subsequent comparisons of the two solutions have shown that downstream of the x = 1.2-meter (48-in.) station the boundary-layer thickness varied inversely as the density ratio while the length of flow had little effect on the rate of boundary-layer growth, at least for flow distances of several boundary-layer thicknesses. These results indicated that the local density must be accurately known before reliable predictions of boundary-layer thicknesses can be obtained for hypersonic nozzles.

In figure 10(c), the normalized total-temperature parameter $\bar{\theta}$ is plotted as a function of the velocity ratio $u/u_e$. The prediction by the method of reference 5 is in good agreement with the data for the outer part of the boundary layer ($u/u_e > 0.8$). The flat-plate solution is nearly the same as the linear variation of Crocco which is in good agreement with the data for $u/u_e < 0.8$. The differences in these predictions are caused partly by the upstream pressure gradient history which is incorporated in the nozzle flow calculation but not in the flat-plate calculation. The magnitude and distribution of the turbulent Prandtl number also affects the variation of $\bar{\theta}$ with $u/u_e$, particularly for $u/u_e < 0.8$, as shown in reference 5.

Comparisons of predictions from both methods for turbulent and laminar boundary layers with the experimental velocity and Mach number profiles (figs. 10(a) and 10(b), respectively) indicates the boundary layer on the nozzle wall is not laminar at this x = 2.083-meter (82-in.) station. From the previous discussion of figure 10 and the results shown in reference 5 for this nozzle flow, it is evident that not only must the local density levels be accurately known, but also the entire flow history must be included in the calculation before agreement with experimental profiles and boundary-layer thickness can be expected. Nevertheless, the equivalent-flat-plate solution for turbulent flow gives much better agreement with $T_t/T_o$, $u/u_e$, and $M/M_e$ profiles (figs. 9(b), 10(a), and 10(b), respectively) than the solution with the upstream flow history included. Of course, the boundary-layer thickness is forced to agree by matching $N_{Re,\delta}$ with the data so that no prediction of $\delta$ is obtained. Other than this lack of any prediction for boundary-layer thickness, the only notable deficiency in the flat-plate solution is the overprediction in $T_t/T_o$ for 3.8 cm < y < 7.6 cm (1.5 in. < y < 3 in.) (fig. 9(b)) and the resulting overprediction of $\bar{\theta}$ for $u/u_e$ > 0.8 as shown in figure 10(c). The nearly quadratic trend of $\theta$ with $u/u_e$ indicated by the data in this region are characteristic of nozzle-wall boundary layers (ref. 47) and are believed to be caused mainly by upstream pressure and wall temperature gradients. The nearly linear trend of the present data for $u/u_e$ < 0.8 is typical of flat-plate data and may be related to the thick viscous sub-layer which, from figure 10(a), extends out to values of $u/u_e$ = 0.7 to 0.8.

Since the predictions for the profile shapes by the turbulent flat-plate solution are in reasonable agreement with data, the most likely cause of the overprediction in boundary-layer thickness at x = 2.083 meters (82 in.) from the solution by the method of reference 5 (obtained with the proper upstream boundary conditions) would be simply an overprediction of the rate of boundary-layer growth in the upstream region of the nozzle. One way to obtain predictions of smaller growth rates is to reduce the eddy viscosity by large amounts. The effects of various modifications to the eddy viscosity and other inputs used in the theory will now be considered in an attempt to identify the cause of the overpredictions in boundary-layer thickness.

### Effects of Modifications to Theory Inputs

The eddy viscosity is defined in terms of the turbulent shear and normal velocity gradient as

$$\tau_T = -\overline{(\rho v)'u'} = \epsilon \frac{\partial u}{\partial y} \tag{9}$$

Expansion of the Reynolds stress correlation

$$\overline{(\rho v)'u'} = \rho \, \overline{v'u'} + v \overline{\rho'u'} + \overline{\rho'v'u'}$$

and introduction of the mixing length $l$ and intermittency functions in the x- and y-directions, $\Gamma_x(x)$ and $\Gamma_y(y)$, results in the following expression for $\epsilon$ (see ref. 5):

$$\epsilon = \Gamma_x \Gamma_y \left[ \rho l^2 \left| \frac{\partial u}{\partial y} \right| - l^2 \frac{\partial \rho}{\partial y} \left( v + l \left| \frac{\partial u}{\partial y} \right| \right) \right] \tag{10}$$

where

$$\frac{l}{\delta} = \left[ 1 - \exp\left( - \frac{y \rho_w}{A^* \mu_w} \sqrt{\frac{\tau_w}{\rho_w}} \right) \right] f\left( x, \frac{y}{\delta} \right) \tag{11}$$

The mixing-length function for the near-wall region is

$$f_n = 0.4 \frac{y}{\delta} \qquad\qquad \left( \frac{y}{\delta} \leqq 0.1 \right) \tag{12}$$

and for the far-wall region

$$f_f = \text{Constant} = 0.09 \qquad\qquad \left( \frac{y}{\delta} \geqq 0.3 \right) \tag{13}$$

An alternate form used in reference 5 for $f_f$ is

$$f_f = f_f\left( H_i^* \right) = 0.1234 H_i^* - 0.0317 \qquad\qquad \left( \frac{y}{\delta} \geqq 0.3 \right) \tag{14}$$

which was designated "variation 2" in reference 5. The values of f for the range in y/δ of $0.1 \leqq y/\delta \leqq 0.3$ were determined from a straight-line segment between the limits for $f_n$ and $f_f$ as noted previously.

Laminar solutions are obtained for $\epsilon = 0$ or $\Gamma_x(x) = 0$. If an established turbulent boundary layer is subjected to large streamwise accelerations, the turbulence may be suppressed, and $\Gamma_x$ would be correspondingly reduced. Several criteria for such laminarization effects have been suggested, one of which is

$$K = \frac{\mu_e}{\rho_e u_e^2} \frac{du_e}{dx}$$

In the investigation of reference 54, when K exceeded about 2 to $3 \times 10^{-6}$ in the approach to the nozzle throat, the boundary-layer profiles and heat-transfer rates in the throat

region tended to approach those for a laminar boundary layer. This laminarization trend persisted downstream of the throat minimum, even though the local values of K decreased below the level of $2 \times 10^{-6}$.

The variations with axial distance of K, $N_{Re,x}$, and $N_{Re,\theta}$ (for laminar and turbulent solutions) for the present nozzle are given in figure 12. It is seen that K exceeds the "laminarization criteria" upstream of the throat and hence the wall boundary layer presumably could be partially or completely laminar in this region. If the boundary layer did revert to laminar flow, this condition might persist far downstream because of the associated small values of $N_{Re,\theta}$ which peak at 3000 in the throat and decrease to a minimum of 1400 about 30.5 centimeters (12 in.) downstream of the throat. On the basis of these levels and distributions of K and $N_{Re,\theta}$ a trial $\Gamma_x$ distribution shown in figure 11 was used for several solutions.

The $\Gamma_y(y)$ function in equation (10) is used to represent the effect of intermittency in the outer part of a turbulent boundary layer. The density gradient term in equation (10), referred to herein as the $\rho'$ term, decreases the eddy viscosity in the outer part of the boundary layer if $\partial\rho/\partial y$ is positive. The eddy viscosity is also decreased by the use of either of the two intermittency functions, which vary between 0 and 1.0, and by reductions in mixing length.

Several modifications to the eddy viscosity of this nature were used in various combinations to obtain a series of solutions for the present nozzle flow. In order to illustrate the effect of such modifications, results from four typical solutions are presented and compared with experimental results in figure 13 and table VI. Solution number 1 is the same as the turbulent solution already presented in figures 9(b) and 10 and in table V(b) by the method of reference 5. The turbulent Prandtl number distributions used in these four solutions are given in the inset in figure 13(a) and other inputs are listed in table VI. None of the four solutions shown utilized the $\rho'$ term because it was found that while the eddy viscosity and boundary-layer thickness were reduced the profile shapes were not sufficiently full.

TABLE VI.- EFFECTS OF EDDY VISCOSITY MODIFICATIONS AND COMPARISON WITH EXPERIMENTAL RESULTS

| Solution number | $f_f$ | $\Gamma_x$ | $\Gamma_y$ | $(l/\delta)_{max}$ | $H_i^*$ | Values at x = 2.083 meters (82 in.) | | | | | | | | |
| | | | | | | $\delta$ | | $c_f$ | $\theta$ | | $\delta^*$ | | $\delta^*/\theta$ | $N_{Re,\theta}$ |
| | | | | | | cm | in. | | cm | in. | cm | in. | | |
| 1 ———— | Equation (14) | 1.0 | 1.0 | 0.069 | 1.724 | 18.1 | 7.14 | $5.22 \times 10^{-4}$ | 0.29 | 0.114 | 12.20 | 4.807 | 42.1 | 7810 |
| 2 —— —— | Equation (14) | Figure 11 | 1.0 | .055 | 2.143 | 9.87 | 3.89 | 4.43 | .130 | .051 | 7.15 | 2.818 | 55.5 | 3470 |
| 3 – – —— | 0.09 | Figure 11 | 1.0 | .09 | 1.918 | 11.65 | 4.59 | 5.56 | .178 | .070 | 7.18 | 2.823 | 41.6 | 4770 |
| 4 – – – —— | .09 | Figure 11 | Reference 5 | .09 | 1.920 | 10.70 | 4.21 | 5.29 | .160 | .063 | 7.86 | 3.098 | 49.2 | 4310 |
| Experiment | | | | | | 9.4 | 3.7 | 5.2 | .173 | .068 | 4.63 | 1.82 | 26.7 | 4760 |
| | | | | | | 8.64 | 3.4 | 4.3 | .155 | .061 | 4.31 | 1.70 | 27.8 | 4640 |
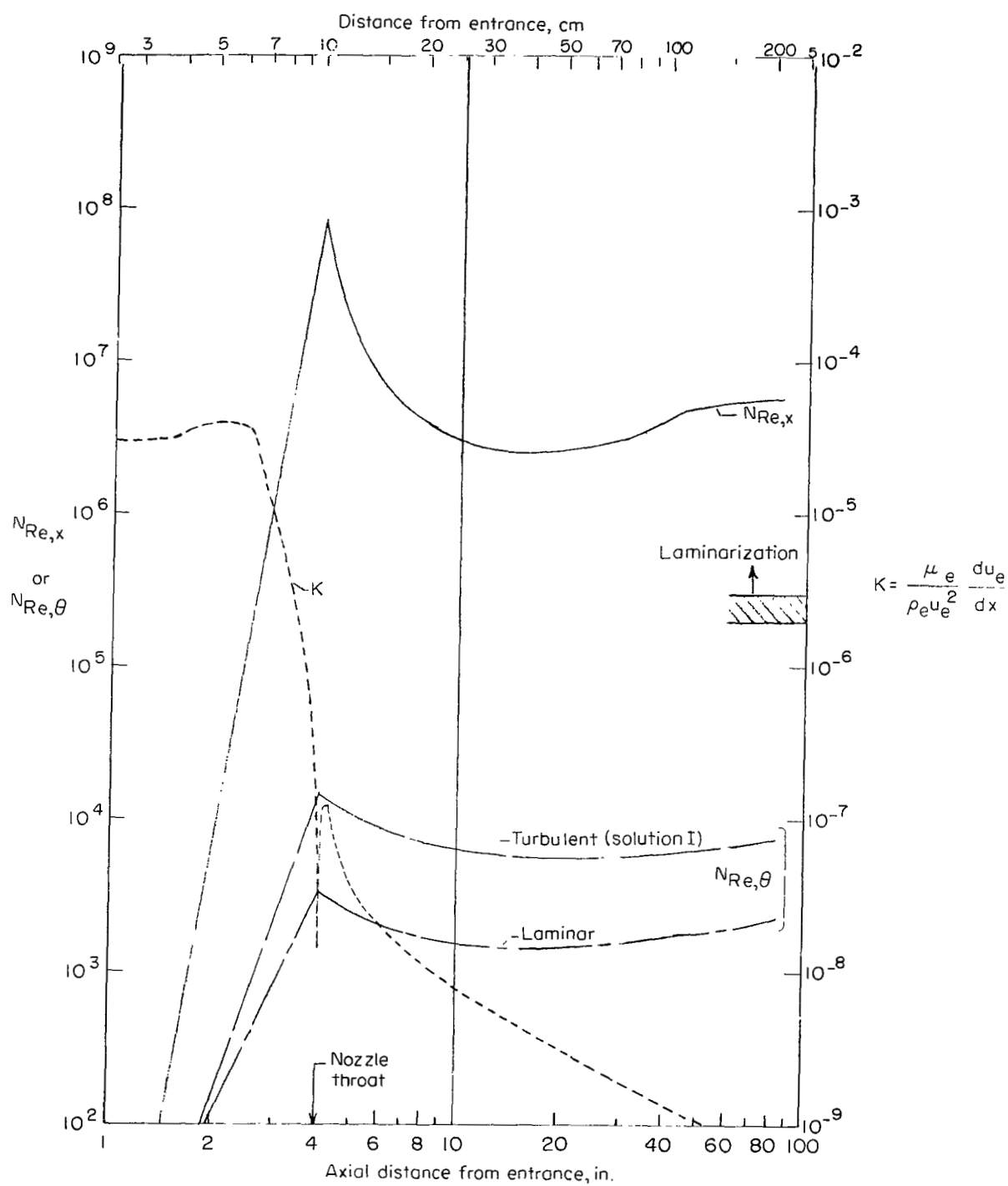
Figure 12.- Variations of Reynolds numbers and laminarization parameter at the edge of the nozzle wall boundary layer.
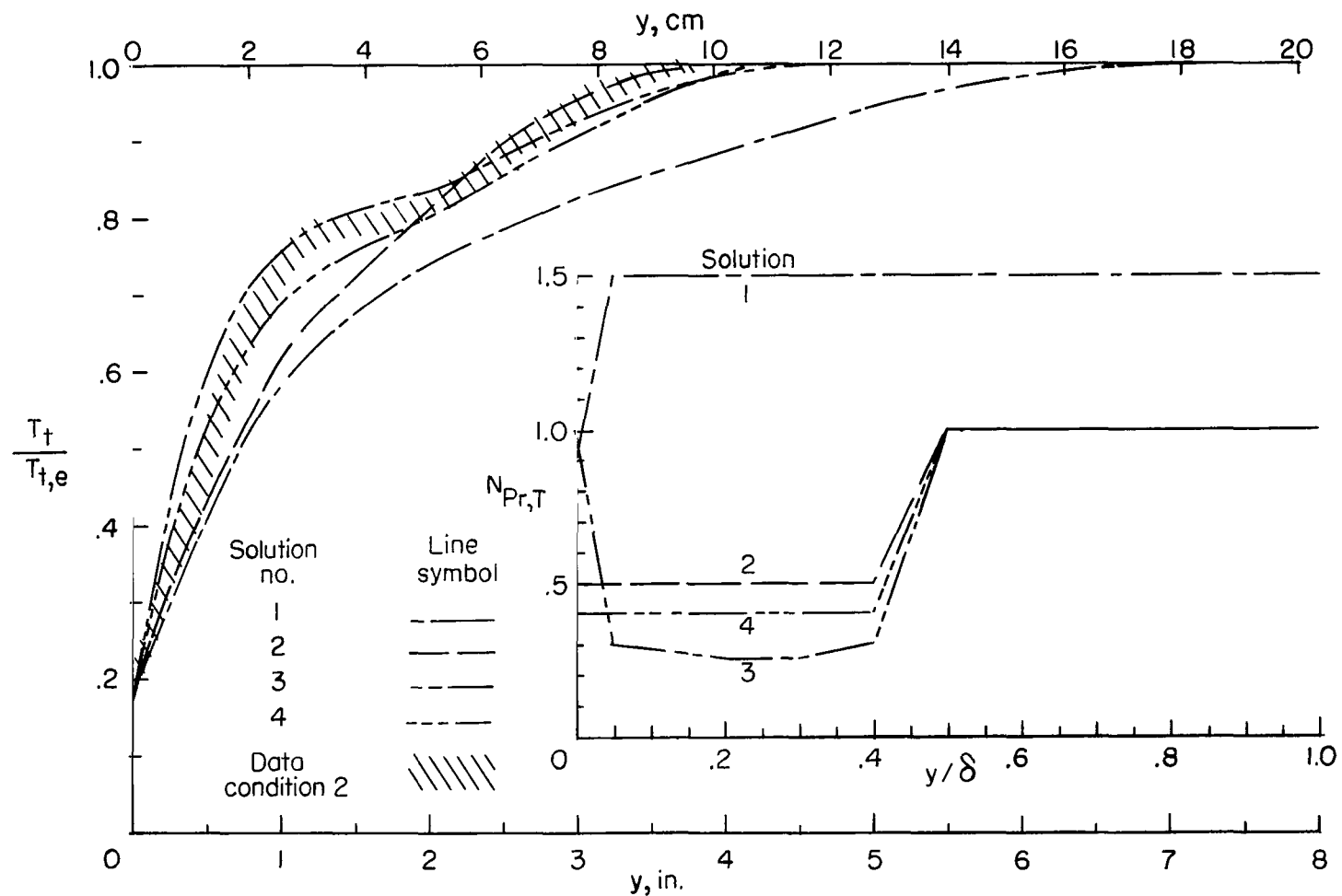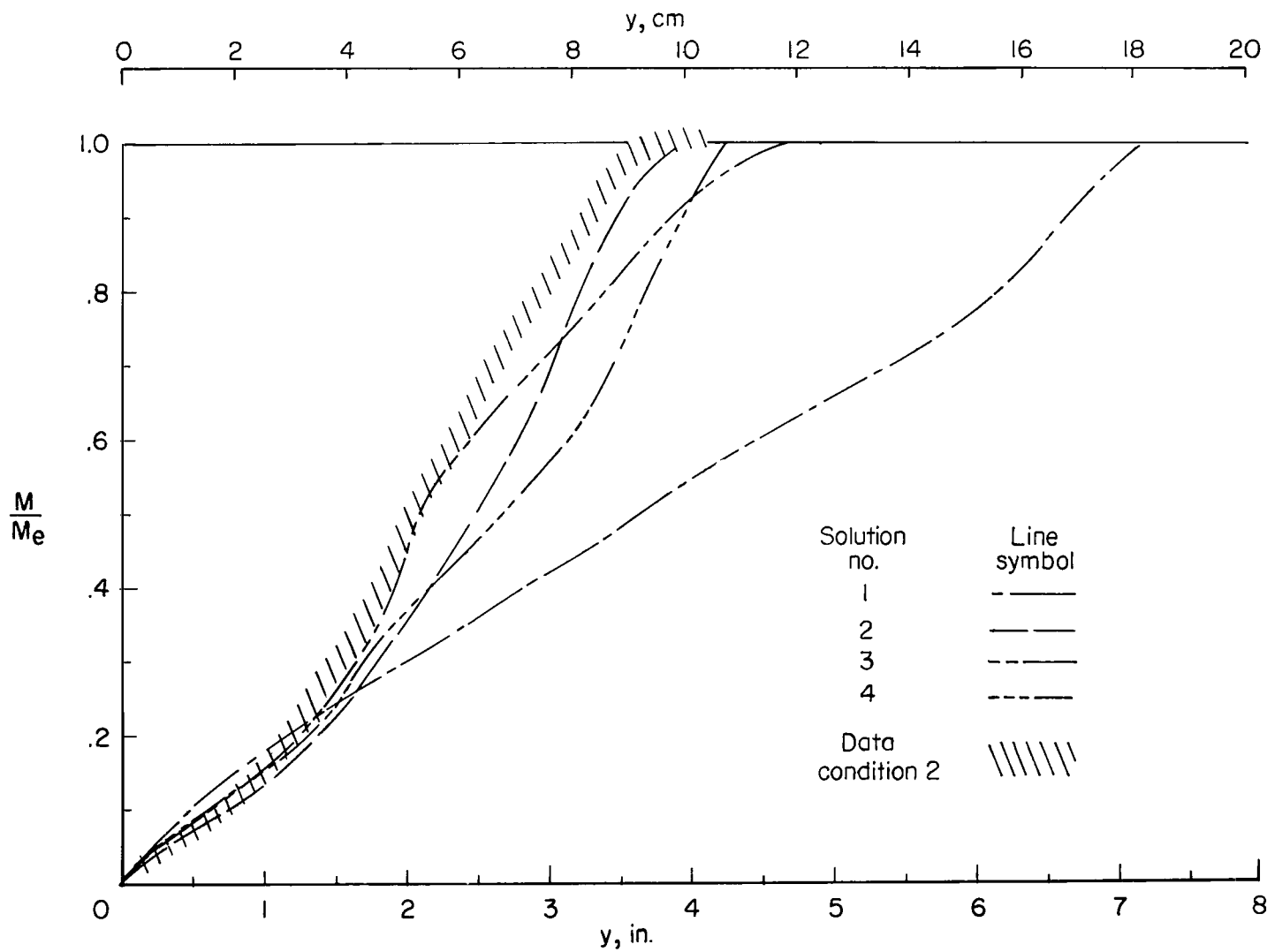
(a) Stagnation temperature.

Figure 13.- Effects of eddy-viscosity modifications on theoretical profiles at  x = 2.083 meters (82 in.)  and comparisons with experimental profiles.
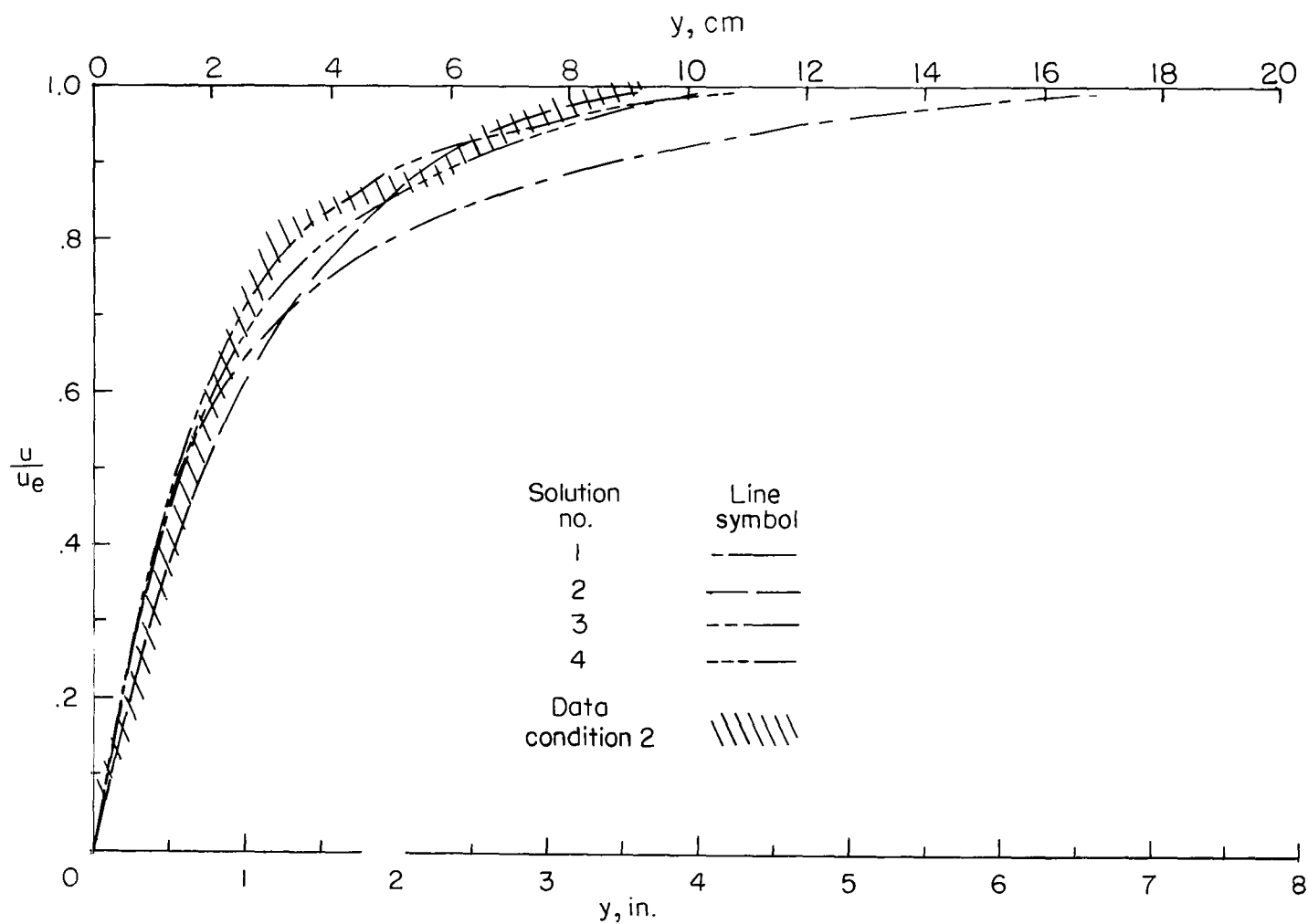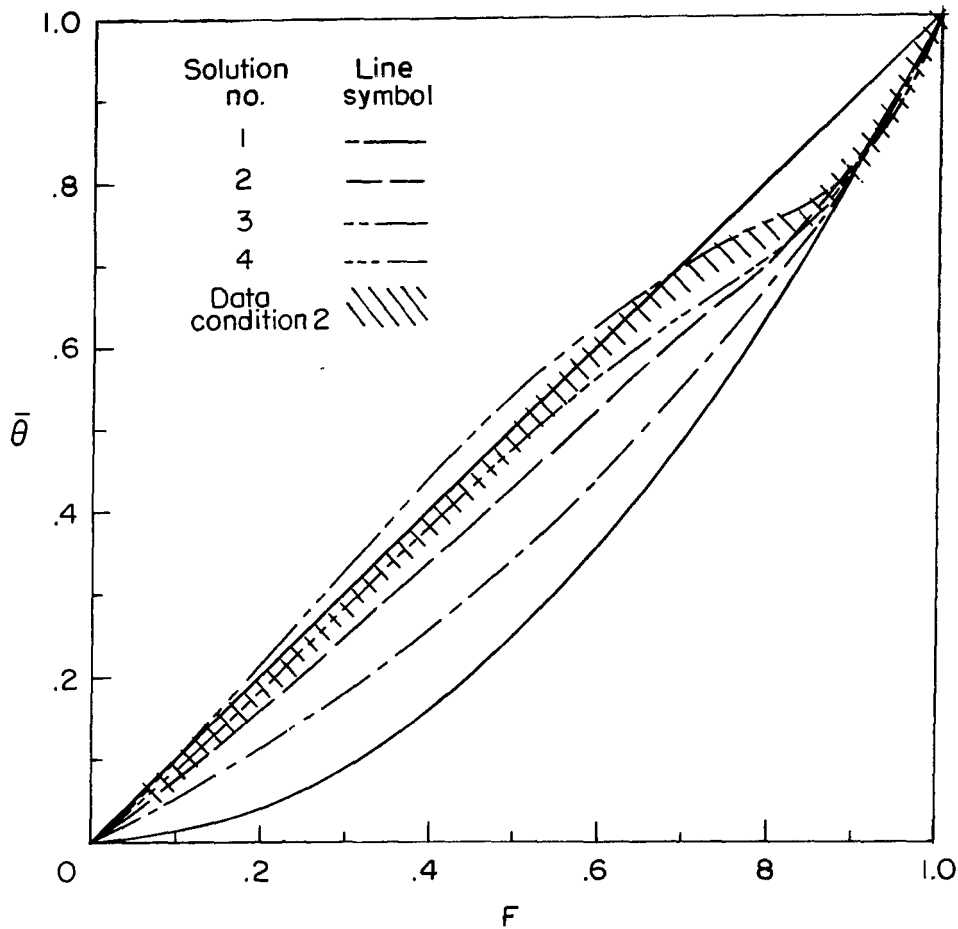
(b) Velocity.

Figure 13.- Continued.

(c) Mach number.

Figure 13.- Continued.

(d) Total-temperature parameter variation with velocity.

Figure 13.- Concluded.

The only way to reduce the boundary-layer thicknesses significantly while retaining good profile shapes was by using $\Gamma_x = 0$ over some upstream portion of the nozzle. The $N_{Pr,T}$ function has little effect on boundary-layer thickness but does control the Crocco profile directly. These effects of the $\Gamma_x$ function and $N_{Pr,T}$ are illustrated by comparisons of results from solutions 1 and 2. While solution 2 has about the right boundary-layer thickness, the total-temperature and velocity profiles (figs. 13(a) and 13(b)) are not sufficiently full for $y < 5.10$ centimeters (2 in.). The Mach number and Crocco profiles (figs. 13(c) and 13(d)) are considerably improved. In order to obtain fuller profiles for $y < 5.10$ centimeters (2 in.), $(l/\delta)_{max}$ was increased by using $f_f = 0.09$, and further reductions in $N_{Pr,T}$ gave good agreement with the Crocco profile. Comparison of theoretical profiles and $\delta$, $c_f$, and $\theta$ from solutions 2, 3, and 4 with the experimental results (fig. 13 and table VI) shows that these solutions essentially bracket the data except for the Mach number profiles. The large range in eddy viscosity for these
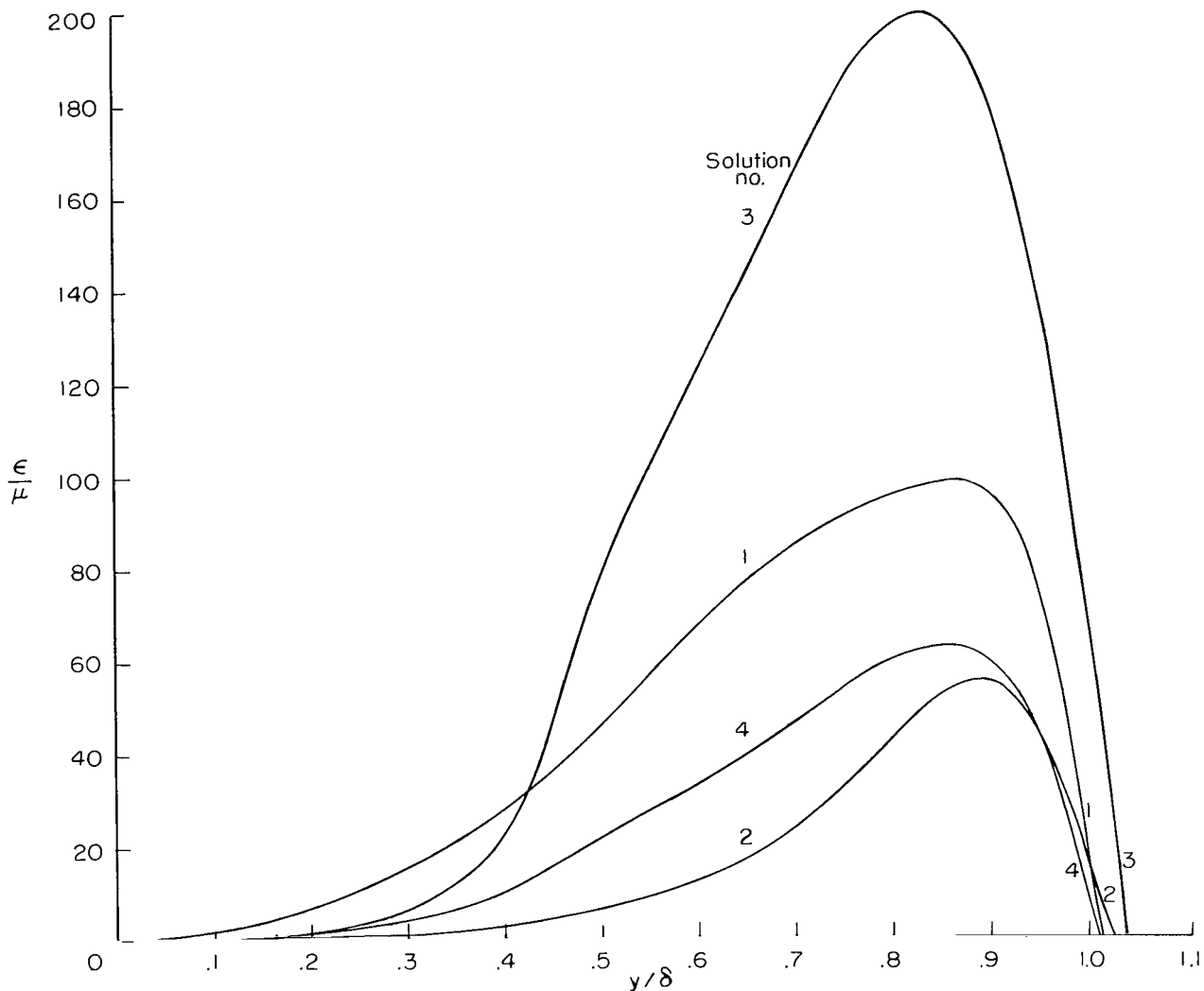
Figure 14.- Eddy-viscosity distribution at x = 2.083 meters (82 in.) from the four theoretical solutions of figure 13.

four solutions is shown in figure 14. These distributions should not be used to infer any general causative trends between eddy viscosity and flow variables since the eddy-viscosity values were obtained from the solutions at x = 2.083 meters (82 in.) and are influenced by the entire upstream history of the boundary layer as well as by local conditions.

The results shown in figure 13 and the preceding discussion indicate that further adjustment of the theoretical inputs, particularly $\Gamma_x$, $N_{Pr,T}$, and $(l/\delta)_{max}$, the predictions could probably be brought into as close agreement with the data as desired. However, further adjustments and solutions are not justified because of limitations in the data and theory.

The principal limitations in the data, besides the usual experimental uncertainties, are the unknown extent of upstream laminarization and the unknown wall-temperature history. Comparison of the preliminary version of the present data as given in reference 5 with the final corrected data herein emphasizes the experimental uncertainties that are of particular concern for all boundary-layer data obtained at hypersonic conditions. As mentioned previously, the present data as published in reference 5 did not include the rarefaction corrections to pitot pressure, and the total-temperature corrections were preliminary estimates. Also, the previous free-stream density was almost 30 percent larger than the present value for a stagnation pressure roughly 10 percent smaller. This reduction in free-stream density for the present conditions increased the predicted boundary-layer thickness by about 40 percent. Thus, all of the present conclusions concerning the comparisons between predictions and experimental results hinge on the accuracy of these large corrections. It is believed that the "final" corrected data, as presented herein, are accurate to within $\pm 10$ percent. The new corrections have changed the preliminary results as presented in reference 5 only for $y/\delta < 0.5$ where the maximum changes were: an increase in $T_t/T_O$ of about 20 percent, a decrease in $M/M_e$ of nearly 50 percent, and a decrease in velocity of about 20 percent. These changes in $T_t/T_O$ and $u/u_e$ produce a nearly linear variation in $\overline{\theta}$ with $u/u_e$ (for $u/u_e < 0.8$) rather than the quadratic type variation shown previously in reference 5. The quadratic variation typical of most previous nozzle-wall boundary layers may be caused partly by cold-wall conditions in the settling-chamber and nozzle-throat regions of most facilities, a condition which is not present in the Mach 19 nitrogen facility. Recent data obtained by W. V. Feller in the Langley Mach 6 facility show that the typical quadratic Crocco profile near the nozzle exit is modified to a more nearly linear profile by increases in wall temperature in the settling chamber and throat region of the nozzle.

The principal limitations in the theory are the same as those for any turbulent boundary theory, namely, the unknown relations between turbulent flux correlations and mean flow quantities. At present, the best that can be done is to model these correlations and essentially by trial-and-error processes, as demonstrated herein, to determine what modifications to the models give the best predictions. The real problem with this process is that the results may not be unique. Another limitation in the theory is the assumption of constant static pressure which is believed to be the main reason for the overpredictions in $\delta^*$ (see table VI) from solutions 2 to 4. The overpredictions in $\delta^*$ may also be partly caused by transverse curvature effects, which were included in the theory, but only to first order. (See ref. 5.) Nevertheless, on the basis of these comparisons, it seems likely that the boundary layer was laminarized to some extent in the throat region. It is also apparent from the present results and those of reference 5 that in order to obtain agreement with the present experimental Crocco profiles, values of $N_{Pr,T}$ of 0.5 or less are required over the inner part of the boundary layer. Again, due to uncertainties

in the data and in the upstream boundary conditions and $\Gamma_x$ variation, these conclusions must be considered as only tentative.

## COMPARISONS WITH PREVIOUS DATA

To the authors' knowledge, corrections for viscous or rarefaction effects on pitot-pressure measurements have not been applied to the previous data used in the following comparisons except the data of reference 11.

### Mach Number Profiles

The present Mach number profiles are compared with previous data for nozzle-wall boundary layers in figure 15. The data in this figure illustrate the large differences that can occur in profile shapes over the wide range of test conditions represented. It can be seen that, in general, the profiles become less full as the Mach number is increased and $N_{Re,\theta}$ is decreased. In fact, it was found that the parameter $M_e / \sqrt{N_{Re,\theta}}$ generally increased as the profile shapes shown decreased in fullness. Thus, consideration of the data for $\gamma = 7/5$ shows that the fullest profiles (those to the left in the figure, refs. 12 and 28) have $0.03 \lesssim M_e / \sqrt{N_{Re,\theta}} \times 10^3 \lesssim 0.1$, while the group of profiles that are more nearly linear (refs. 15, 17, and the present data) have $0.2 \lesssim M_e / \sqrt{N_{Re,\theta}} \times 10^3 \lesssim 0.3$. The data of Wallace (ref. 19) have $M_e / \sqrt{N_{Re,\theta}}$ values of about 0.11 to 0.14 which are between the aforementioned ranges, and the profile shapes are consistent with this range since they follow the profile group with full shapes for $y/\delta < 0.1$ and change over to the "linear" group for $y/\delta > 0.4$. The helium profiles follow essentially the same trends as noted for the air and nitrogen data.

### Velocity Profiles

The values of $N$ in the power-law velocity profile relation

$$\frac{u}{u_e} = \left(\frac{y}{\delta}\right)^{1/N} \tag{15}$$

are of use in characterizing and classifying velocity profiles.

The values of $N$ which best match the outer portion of the present velocity profiles are shown in figure 16. These values of $N$ have been compared with results from previous data for axisymmetric nozzles in reference 55. The present data for $N$ are near the upper side of the data band shown in reference 55 where it was indicated that for $N_{Re,\theta} \approx 2500$, $N$ would increase approximately as $(T_w/T_o)^{0.25}$. In order to determine if this variation is also present at other values of $N_{Re,\theta}$, values of $N(T_w/T_o)^D$ from the present and previous data (data for adiabatic wall temperatures and $M_e > 17$ have
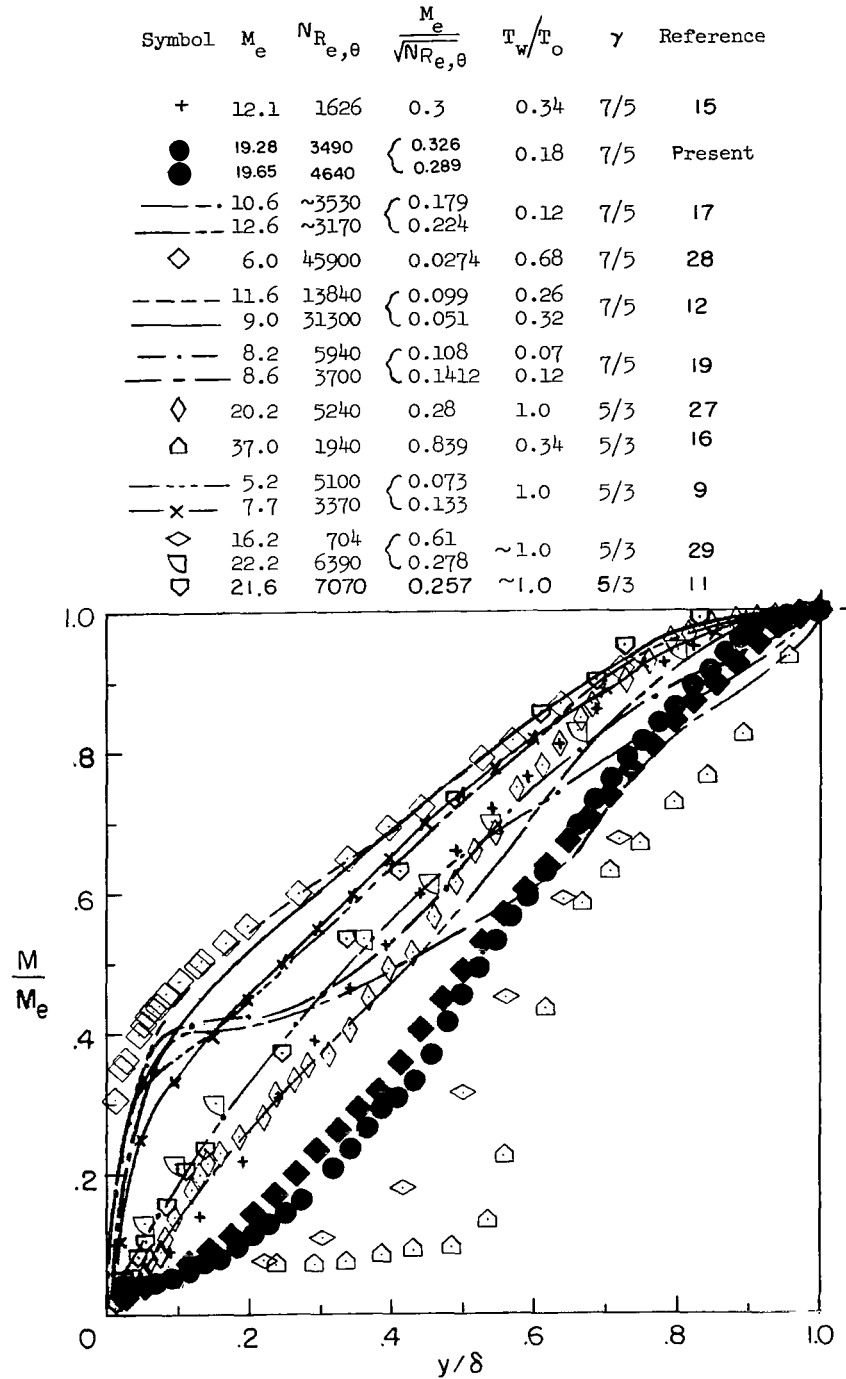
| Symbol | $M_e$ | $N_{R_{e,\theta}}$ | $\dfrac{M_e}{\sqrt{N_{R_{e,\theta}}}}$ | $T_w/T_o$ | $\gamma$ | Reference |
|---|---|---|---|---|---|---|
| + | 12.1 | 1626 | 0.3 | 0.34 | 7/5 | 15 |
| ● | 19.28 | 3490 | { 0.326 | 0.18 | 7/5 | Present |
| ● | 19.65 | 4640 | 0.289 | | | |
| —  —  . | 10.6 | ~3530 | { 0.179 | 0.12 | 7/5 | 17 |
| ———  — — | 12.6 | ~3170 | 0.224 | | | |
| ◇ | 6.0 | 45900 | 0.0274 | 0.68 | 7/5 | 28 |
| — — — — | 11.6 | 13840 | { 0.099 | 0.26 | 7/5 | 12 |
| ——— | 9.0 | 31300 | 0.051 | 0.32 | | |
| — . — | 8.2 | 5940 | { 0.108 | 0.07 | 7/5 | 19 |
| — . . — | 8.6 | 3700 | 0.1412 | 0.12 | | |
| ◊ | 20.2 | 5240 | 0.28 | 1.0 | 5/3 | 27 |
| ⌂ | 37.0 | 1940 | 0.839 | 0.34 | 5/3 | 16 |
| — ... — | 5.2 | 5100 | { 0.073 | 1.0 | 5/3 | 9 |
| — x — | 7.7 | 3370 | 0.133 | | | |
| ◇ | 16.2 | 704 | { 0.61 | ~1.0 | 5/3 | 29 |
| ⊽ | 22.2 | 6390 | 0.278 | | | |
| ▽ | 21.6 | 7070 | 0.257 | ~1.0 | 5/3 | 11 |



Figure 15.- Comparison of experimental Mach number profiles with previous results on nozzle walls for $8.25 \leqq M_e \leqq 37$ and $1.9 \times 10^3 < N_{Re,\theta} < 114 \times 10^3$. Data from reference 11 are the same as data of reference 29, but corrected for pitot-pressure errors, and variable local static pressure.
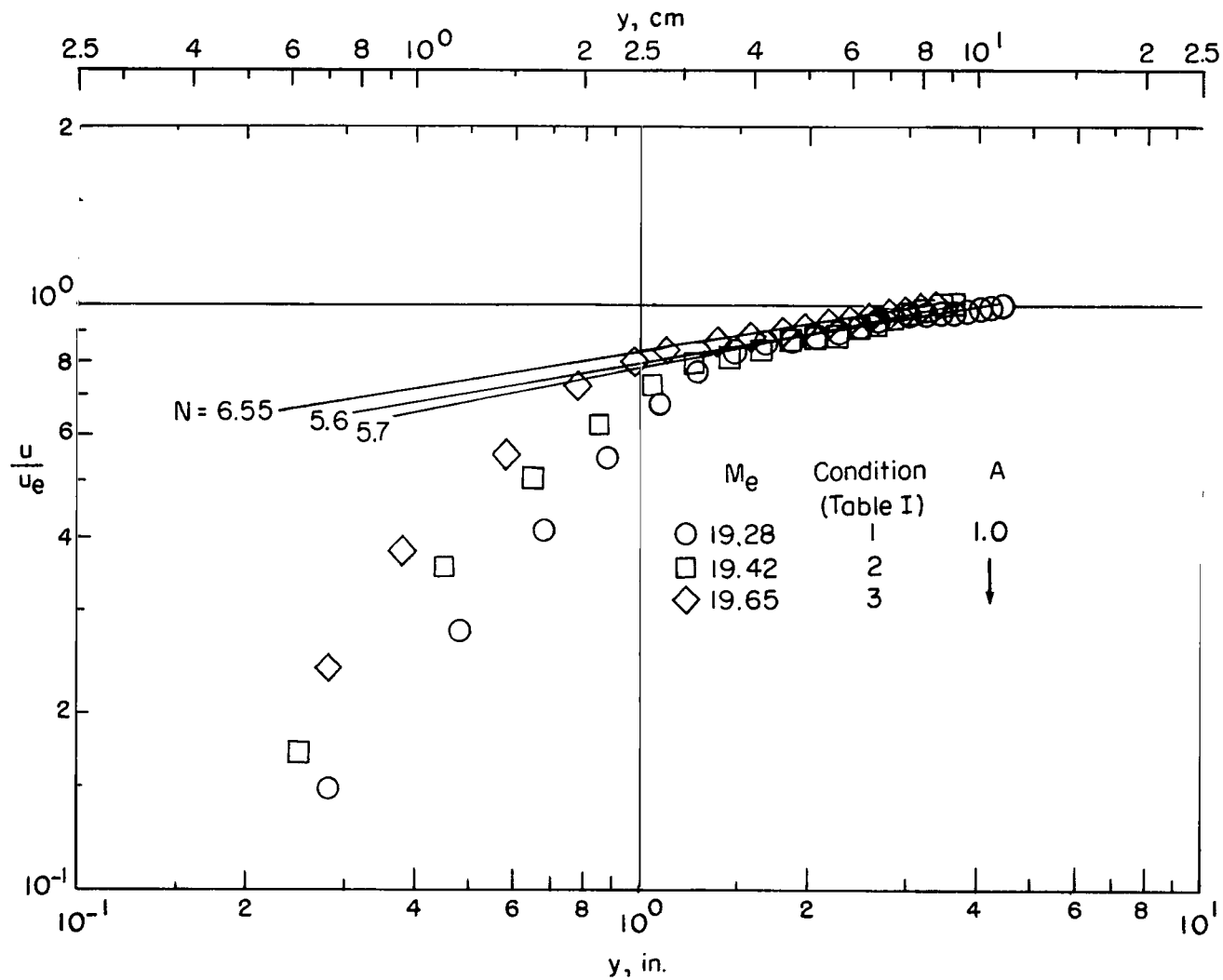
y, cm

2.5  4  6  8  $10^0$  2  2.5  4  6  8  $10^1$  2  2.5

2

$10^0$

8

$\frac{u}{u_e}$

N = 6.55  5.6  5.7

6

4

2

$10^{-1}$

$M_e$  Condition  A
(Table I)

○ 19.28  1  1.0

□ 19.42  2

◇ 19.65  3

$10^{-1}$  2  4  6  8  $10^0$  2  4  6  8  $10^1$

y, in.

Figure 16.- Power-law variation of present velocity profiles.  A = 1.0.

TABLE VII.- REFERENCES AND VALUES OF EXPERIMENTAL PARAMETERS USED IN FIGURES 17 AND 19

| Reference | $\gamma$ | $M_e$ | $N_{Re,\delta}$ | $N_{Re,\theta}$ | $T_w/T_e$ | $T_w/T_o$ | $(\delta_s/\delta)_{meas}$ | $N$ |
|---|---|---|---|---|---|---|---|---|
| ○ 15 | 7/5 | 11.85 | $3.12 \times 10^4$ | $0.94 \times 10^3$ | 9.10 | 0.312 | 0.350 | 6.45 |
|  |  | 11.99 | 4.21 | 1.26 | 9.89 | .332 | .325 | 6.50 |
|  |  | 12.07 | 5.25 | 1.63 | 10.40 | .344 | .300 | 6.57 |
| □ 14 | 7/5 | 6.65 | 2.25 | 2.79 | 3.12 | .312 | .100 | 3.31 |
|  |  | 11.30 | 4.49 | 3.77 | 7.27 | .317 | .200 | 3.69 |
|  |  | 11.50 | 4.70 | 2.58 | 7.36 | .268 | .220 | 4.92 |
| ◇ 17 | 7/5 | 8.25 | 18.20 | 12.0 | 1.93 | .150 | .010 | 4.10 |
|  |  | 16.30 | 7.88 | 1.85 | 5.58 | .118 | .080 | 4.16 |
|  |  | 14.00 | 6.98 | 2.40 | 4.07 | .119 | .075 | 4.09 |
|  |  | 12.65 | 6.55 | 3.17 | 3.25 | .117 | .070 | 2.71 |
| △ 12. | 7/5 | 8.87 | 40.60 | 16.7 | 5.90 | .352 | .030 | 6.00 |
|  |  | 9.00 | 79.00 | 31.3 | 5.43 | .312 | .025 | 6.10 |
|  |  | 11.27 | 25.00 | 6.63 | 8.42 | .319 | .060 | 6.70 |
|  |  | 11.60 | 40.40 | 13.84 | 8.88 | .259 | .040 | 6.50 |
| ◿ 21 | 7/5 | 8.27 | 4.94 | 2.51 | 6.15 | .420 | .130 | 4.03 |
|  |  | 9.07 | 6.35 | 2.28 | 8.30 | .492 | .217 | 4.36 |
|  |  | 10.06 | 6.35 | 1.70 | 9.04 | .425 | .357 | 4.36 |
| ◹ 9 | 7/5 | 2.95 | 15.49 | 8.19 | 2.74 | 1.0 | .020 | 6.24 |
|  |  | 2.95 | 36.90 | 19.38 | 2.74 | ↓ | .020 | 8.10 |
|  |  | 4.20 | 11.90 |  | 4.53 |  | .012 | 6.00 |
|  |  | 4.20 | 45.50 | 20.65 | 4.53 |  | .010 | 7.70 |
|  |  | 4.20 | 88.50 | 41.60 | 4.53 | ↓ | .011 | 10.00 |
| ◠ 19 | 7/5 | 8.82 | 8.46 | 6.57 | 2.14 | .13 | .040 | ≈3.0 |
|  |  | 8.24 | 6.68 | 5.95 | 1.05 | .07 | .006 | ↓ |
|  |  | 8.62 | 5.37 | 3.70 | 1.93 | .12 | .045 |  |
|  |  | 8.89 | 10.75 | 9.40 | 2.78 | .16 | .045 |  |
| ◇ 28 | 7/5 | ≈6.0 | 143.3 | 45.9 | 5.76 | .706 | .007 | 9.3 |
|  |  | ↓ | 83.6 | 25.9 | 5.70 | .700 | .005 | 8.8 |
|  |  |  | 44.4 | 13.5 | 6.15 | .739 | .010 | 7.8 |
|  |  |  | 24.9 | 8.1 | 6.00 | .736 | .012 | 7.7 |
|  |  |  | 175.1 | 59.9 |  |  |  | 8.4 |
|  |  |  | 116.3 | 33.3 |  |  |  | 8.3 |
|  |  |  | 51.4 | 15.5 |  |  |  | 7.1 |
|  |  |  | 32.3 | 10.0 |  |  |  | 7.1 |
|  |  |  | 234.6 | 77.7 |  |  |  | 8.8 |
|  |  |  | 138.8 | 47.4 |  |  |  | 8.4 |
|  |  |  | 63.3 | 20.4 |  |  |  | 7.3 |
|  |  |  | 42.9 | 13.8 |  |  |  | 6.7 |
|  |  |  | 247.9 | 80.3 |  |  |  | 8.8 |
|  |  |  | 166.5 | 57.1 |  |  |  | 8.4 |
|  |  | ↓ | 79.9 | 26.8 |  |  |  | 6.8 |
|  |  |  | 68.6 | 19.9 |  |  |  | 6.0 |
| ◇ 55 | 7/5 | 7.84 |  | 100.7 |  | .430 |  | 6.44 |
|  |  | 7.90 |  | 162.6 |  | .416 |  | 7.34 |
|  |  | 7.96 |  | 223.9 |  | .410 |  | 8.44 |
|  |  | 7.99 |  | 312.5 |  | .435 |  | 8.48 |
| ◺ 20 | 7/5 | 7.0 |  | 2.09 |  | .512 |  | 6.3 |
| △ 25 | 7/5 | 4.93 | 16.3 | 5.35 | 5.42 | .924 | .0375 | ≈6.0 |
|  |  | 5.01 | 16.5 | 6.48 | 4.29 | .752 | .0272 |  |
|  |  | 5.03 | 15.6 | 7.95 | 3.49 | .586 | .0260 |  |
|  |  | 5.06 | 15.2 | 7.37 | 3.27 | .534 | .0238 |  |
|  |  | 6.83 | 25.0 | 8.55 | 6.34 | .641 | .0440 |  |
|  |  | 6.83 | 29.4 | 12.64 | 5.24 | .511 | .0322 |  |
|  |  | 6.78 | 22.4 | 8.40 | 5.22 | .511 | .0375 |  |
|  |  | 6.77 | 18.1 | 7.96 | 4.64 | .470 | .0410 |  |
|  |  | 7.67 | 20.0 | 8.13 | 5.94 | .466 | .0490 |  |
| ▽ (*) | 7/5 | 5.93 | 104.0 | 17.27 | 5.31 | .661 | .040 | 7.00 |
|  |  | 5.91 | 204.0 | 31.80 | 5.20 | .654 | .020 | 10.00 |
|  |  | 5.95 | 391.0 | 52.40 | 5.15 | .640 | .010 | 10.25 |
|  |  | 7.90 | 44.0 | 12.48 | 5.31 | .394 | .025 | 6.50 |
|  |  | 7.95 | 86.0 | 22.40 | 5.33 | .391 |  | 8.50 |
|  |  | 7.96 | 173.0 | 42.00 | 5.32 | .389 | .020 | 9.50 |
|  |  | 8.02 | 269.0 | 59.50 | 5.34 | .401 |  | 9.80 |
|  |  | 8.04 | 344.0 | 74.00 | 5.53 | .396 | .020 | 10.25 |
|  |  | 9.86 | 32.0 | 13.40 | 6.26 | .317 | .025 | 6.10 |
|  |  | 10.01 | 60.0 | 22.40 | 6.26 | .309 |  | 6.80 |
|  |  | 10.06 | 83.0 | 22.60 | 6.08 | .299 |  | 7.30 |
|  |  | 10.10 | 114.0 | 31.90 | 5.85 | .286 | .005 | 8.40 |
|  |  | 10.10 | 180.0 | 47.00 | 5.64 | .277 |  | 10.15 |
|  |  | 10.18 | 203.0 | 57.30 | 5.54 | .269 | .005 | 10.10 |
| ⊗ Present | 7/5 | 19.28 | 21.95 | 3.490 | 13.31 | .177 | .25 | 5.7 |
|  |  | 19.42 | 25.70 | 4.760 | 13.52 | .177 | .24 | 5.6 |
|  |  | 19.65 | 25.90 | 4.640 | 12.81 | .163 | .23 | 6.55 |
| ◢ 9 | 5/3 | 6.7 | 18.65 | 5.10 | 9.99 | 1.0 | .037 | 7.10 |
|  |  | 9.9 | 25.20 | 3.37 | 20.60 | 1.0 | .069 | 10.00 |
| ● 27 | 5/3 | 20.2 | 161.10 | 5.24 | 137.00 | 1.0 | .100 | 16.00 |
| ■ 29 | 5/3 | 19.2 | 163.0 | 2.46 | 123.88 | ≈1.0 | .106 |  |
|  |  | 22.2 | 495.0 | 6.39 | 165.28 | ≈1.0 | .051 |  |
| ◆ 16 | 5/3 | 27.0 | 62.2 | 1.50 | 150.3 | .616 | .43 | 18.0 |
|  |  | 26.3 | 25.2 | 1.17 | 82.2 | .355 | .54 | 12.0 |
|  |  | 27.9 | 93.5 | 2.90 | 166.7 | .640 | .37 | 16.5 |
|  |  | 27.6 | 32.6 | 2.15 | 82.6 | .324 | .38 | 11.0 |
|  |  | 28.6 | 138.3 | 3.41 | 93.0 | .340 | .37 | 12.0 |
|  |  | 29.3 | 85.6 | 8.07 | 163.7 | .570 | .27 | 15.2 |
|  |  | 29.4 | 46.4 | 3.73 | 91.1 | .315 | .36 | 13.1 |
|  |  | 32.3 | 51.4 | 1.58 | 113.4 | .325 | .41 | 14.6 |
|  |  | 36.8 | 82.5 | 1.94 | 148.0 | .327 | .53 | 18.1 |
|  |  | 45.5 | 202.0 | 4.30 | 408.4 | .591 | .44 | 19.0 |
|  |  | 44.6 | 149.0 | 2.85 | 223.1 | .336 | .51 | 13.0 |
|  |  | 47.0 | 256.0 | 4.84 | 439.5 | .596 | .46 | 20.0 |
|  |  | 47.3 | 163.0 | 4.35 | 247.2 | .331 | .56 | 14.4 |
| ◣ 11 | 5/3 | 19.1 | 224.0 | 3.62 | 122.5 | ≈1.0 | .110 | ---- |
|  |  | 21.6 | 606.0 | 7.07 | 156.6 | ≈1.0 | .045 | ---- |

*Data obtained from the Von Karman Gas Dynamics Facility, Arnold Engineering Development Center.

been excluded, see table VII) were plotted against $N_{Re,\theta}$ in figures 17(a) and 17(b). Comparison of these two figures show that the correlation of $N$ over the complete range of $N_{Re,\theta}$ is somewhat improved (particularly for the present data) with $D \approx 0.1$ (fig. 17(b)) rather than $D \approx -0.25$ (fig. 17(a)) as would be indicated by the results of reference 55 at $N_{Re,\theta} \approx 2500$.
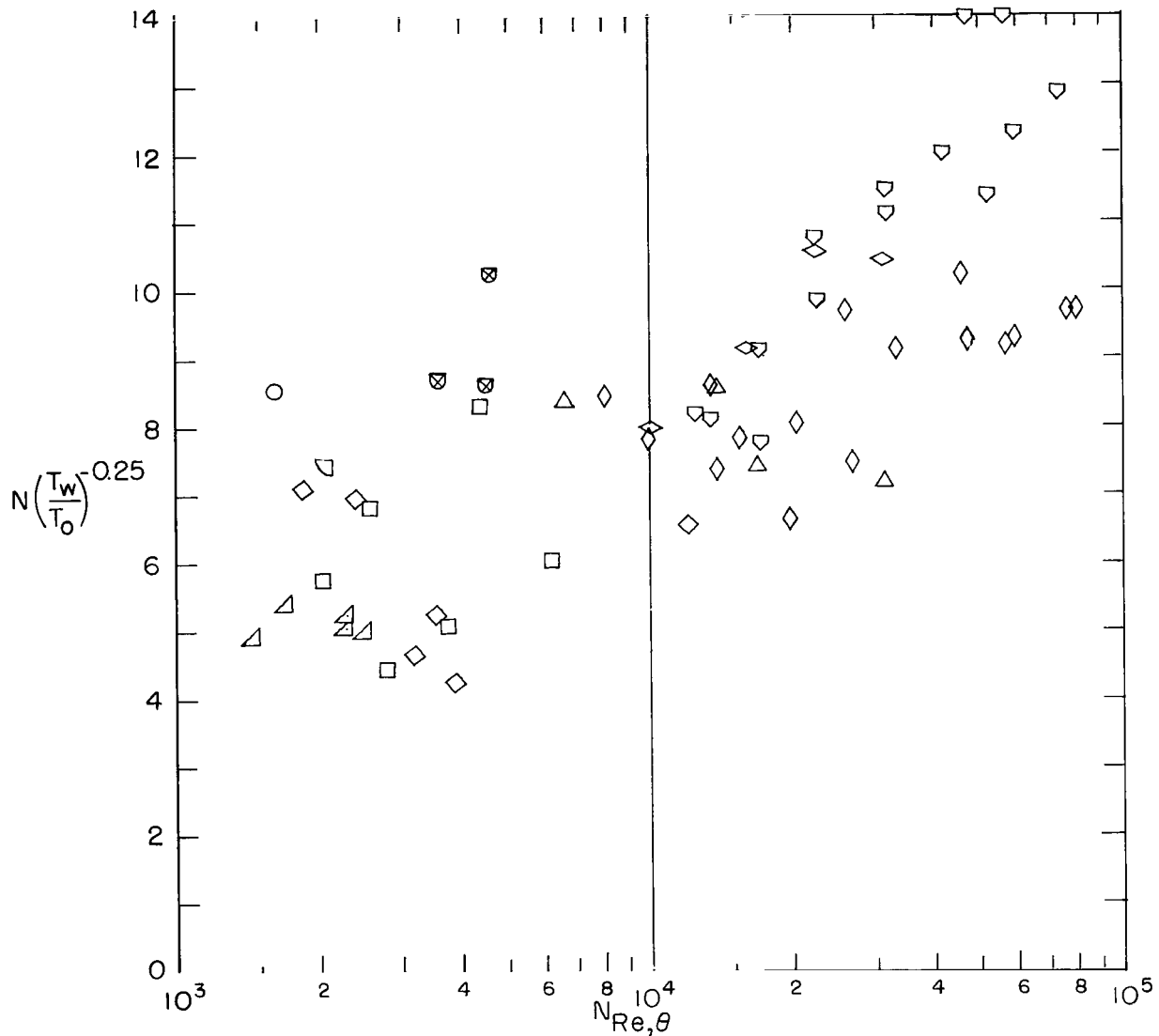


(a) Effect of $T_w/T_o$ on correlation of exponent $N$ in power-law velocity profile according to reference 55.

Figure 17.- Correlation of exponent in power-law velocity profiles. (See table VII for symbol key.) $\gamma = 7/5$, $0.07 \leqq T_w/T_o \leqq 1.0$.

In figure 18 the present velocity-profile data are compared with data for the complete profiles from previous investigations of nozzle-wall boundary layers. This figure illustrates how the viscous sublayer thickness $\delta_S$ (relative to $\delta$) tends to increase with increasing Mach number, decreasing $N_{Re,\theta}$ and decreasing $T_w/T_o$. In order to determine quantitatively this increase in $\delta_S$, it was defined as the value of $y$ at the edge of the region where the velocity profile is approximately linear. In figure 19, the resulting values of $\delta_S/\delta$ are plotted against $M_e/\sqrt{N_{Re,\theta}}$, the same parameter that characterized
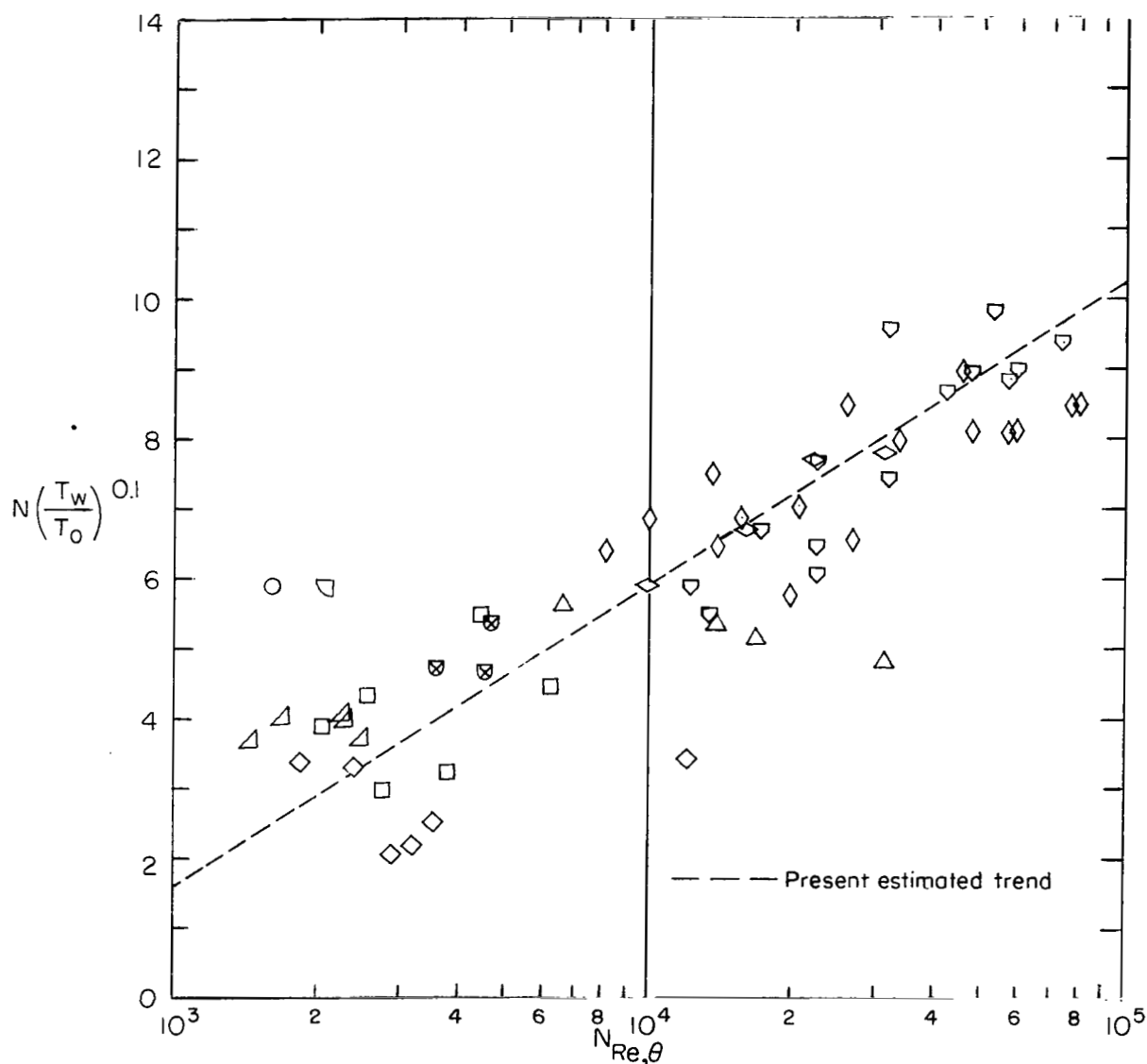


(b) Improved correlation of present and previous data for velocity profile exponent N.

Figure 17.- Concluded.

64

the shape of experimental Mach number profiles (fig. 15). This plot shows a trend for $\delta_s/\delta$ to decrease as $M_e/\sqrt{N_{Re,\theta}}$ decreases. There is apparently no consistent effect of $T_w/T_O$ on the scatter of the data points about the mean variation shown. The values of these parameters for all data used in the figure are given in table VII. While the correlation of figure 19 shows considerable scatter, it should be useful for estimating the sublayer thickness which is important in relation to roughness size responsible for increases in friction drag.



| | $M_e$ | $\dfrac{M_e}{\sqrt{N_{Re,\theta}}}$ | $N_{Re,\theta}$ | $\gamma$ | $T_w/T_{o,e}$ | Reference |
|---|---|---|---|---|---|---|
| ◯ | 6.65 | 0.126 | 2790 | 7/5 | 0.312 | 14 |
| ◻ | 11.30 | .184 | 3770 | | .275 | 14 |
| ◇ | 11.50 | .226 | 2580 | | .268 | |
| △ | 12.00 | .340 | 1265 | | .332 | 15 |
| ◹ | 12.10 | .300 | 1626 | | .334 | 15 |
| ◺ | 11.27 | .139 | 6630 | | .319 | 12 |
| ◠ | 11.60 | .099 | 13840 | | .259 | 12 |
| ◯ | 36.80 | .840 | 1940 | 5/3 | .327 | 16 |
| ◇ | 21.60 | .257 | 7070 | | 1.000 | 11 |
| ◁ | 6.00 | .027 | 45900 | 7/5 | .680 | 28 |
| ● | 19.28 | .321 | 3490 | | .177 | Present |
| ◆ | 19.65 | .289 | 4640 | | .163 | |
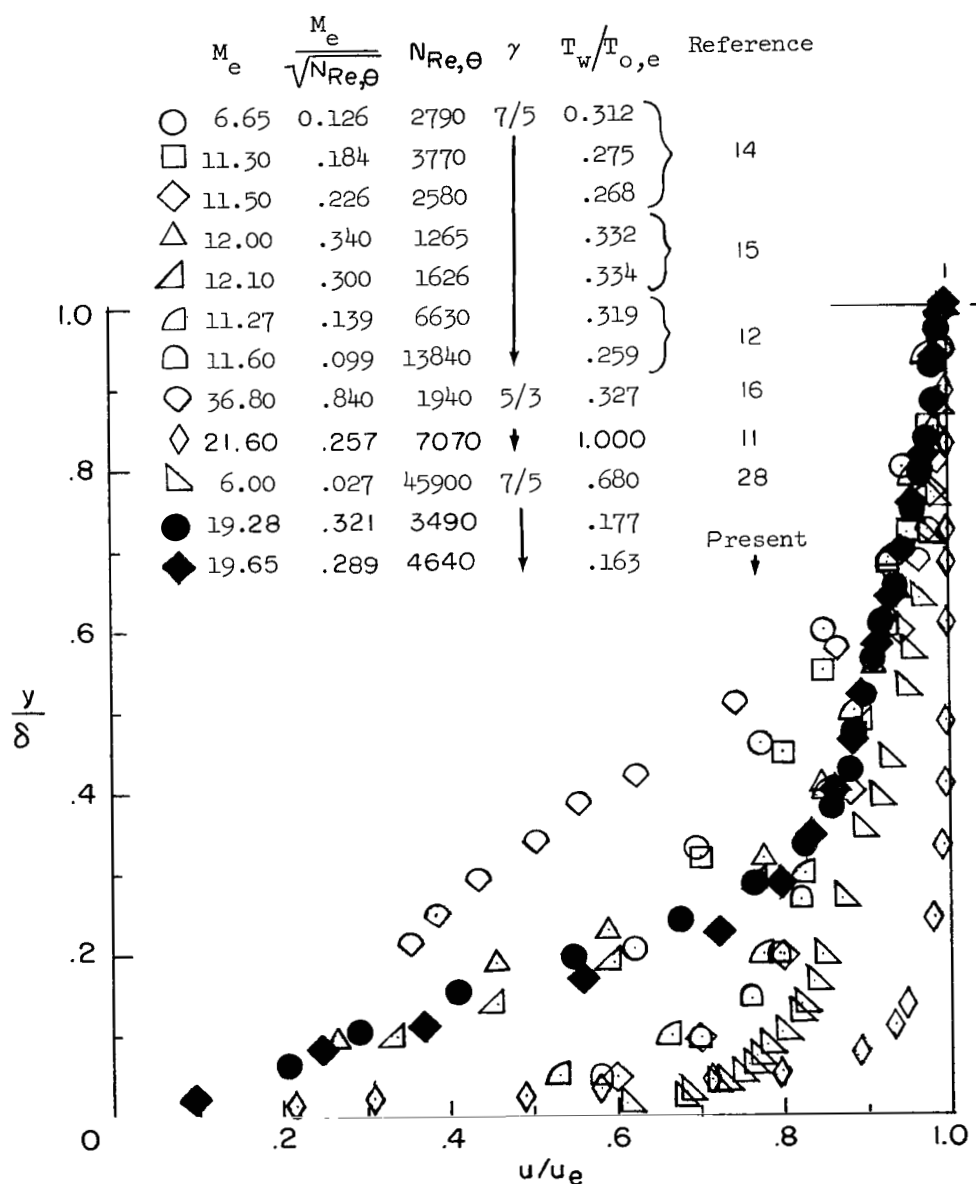
Figure 18.- Comparison of present data with previous results.
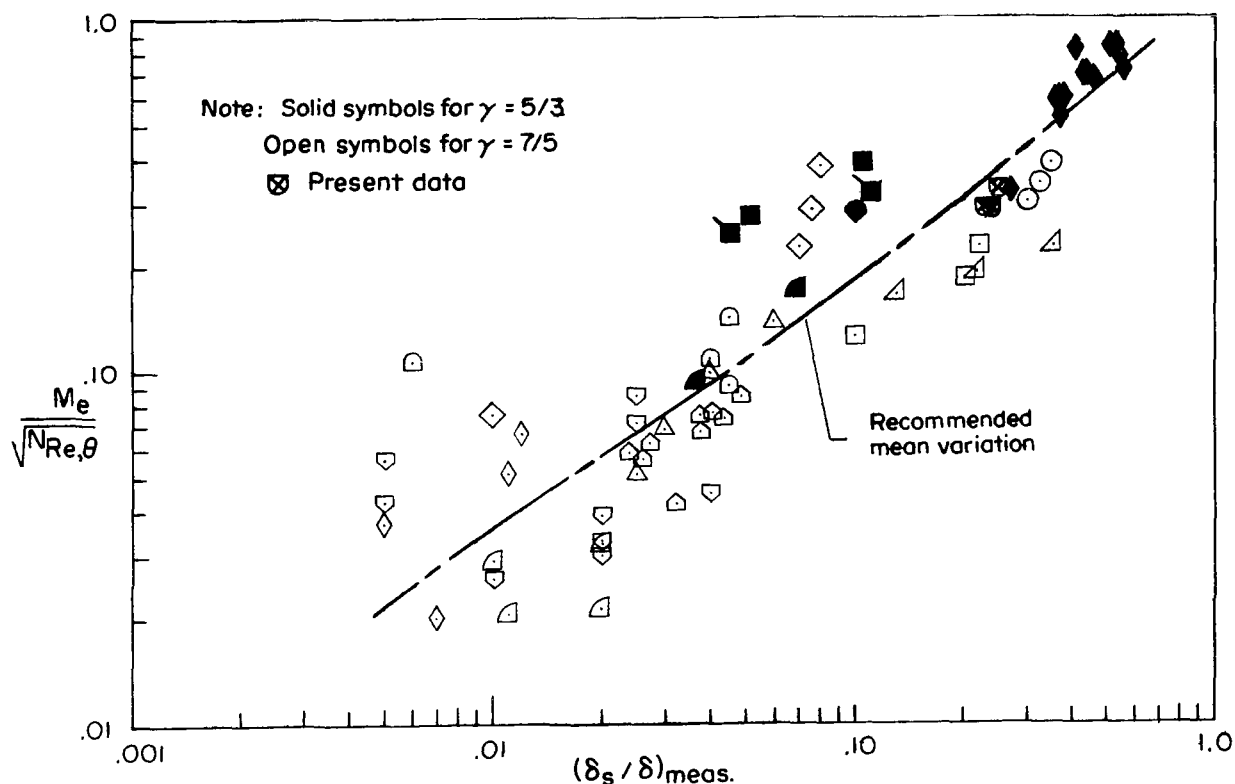
Figure 19.- Variation of viscous sublayer thickness with $M_e/\sqrt{N_{Re,\theta}}$ for nozzle-wall boundary layers. Symbol key, experimental parameters, and references given in table VII.

## Variation of Total Temperature With Velocity

In figure 20 the total-temperature parameter $\bar{\theta} = \dfrac{T_t - T_w}{T_{t,e} - T_w}$ is plotted as a function of $u/u_e$ from the present data and from previous data for a wide range of $M_e$ and $N_{Re,\theta}$. It is seen that most previous data are considerably below the linear Crocco variation which best correlates flat-plate flows. (See ref. 47.) The nozzle-wall data shown in the figure are from some of the same sources used in reference 47 except the recent data from the Von Karman Gas Dynamics Facility, Arnold Engineering Development Center, and the Langley data of W. V. Feller which were not included in the survey of reference 47. The empirical relation $\bar{\theta} = (u/u_e)^2$ seems to best correlate all previous nozzle-wall data except the new unpublished data obtained by Feller at Langley in the same Mach 6 facility used to obtain the data of reference 28. These new data were obtained with the settling-chamber walls and throat region heated to temperatures above the free-stream stagnation temperature. The results suggest that the quadratic variation of $\bar{\theta}$ with $u/u_e$, considered typical of nozzle-wall boundary layers, is caused by the persistent effects on the developing boundary layer of the comparatively cold-wall temperatures in the settling chamber and throat. The arrangement of the heater element

| | $M_e$ | $N_{Re,\theta}$ | $T_w/T_{0,e}$ | $T_w/T_0$ (Settling chamber) | $x$, in.(cm) | Ref. |
|---|---|---|---|---|---|---|
| ◯ | ~6 | $4.57 \times 10^4$ | 0.68 | 0.7 | 94 (239) | 28 |
| ◒ | ~6 | ↓ | | 1.15 | 94 (239) | Feller (unpublished) |
| ◁◁ ◻◻ | }6 to 10 | { 1.25 to 2.24 ↓ | { 0.31 to 0.66 | — | 242 (615) 249 (632) 301 (765) | } VKF, AEDC |
| ◇ ◇ | } 11.3 to 11.6 | 0.66 to 1.38 ↓ | 0.26 to 0.32 } | Cold | { 30 (76) 30 (76) | 12 |
| ⦀ | { 19.3 to 19.7 | { 0.36 to 0.46 ↓ | { 0.16 to 0.18 | Hot | 82 (208) | Present |



Figure 20.— Comparison of total-temperature-velocity profiles with previous data on nozzle walls.

within the settling chamber and the throat construction used in the present facility (see ref. 30) indicate that the effective surface temperatures in the settling chamber are somewhat higher than stream stagnation temperature while the throat temperatures are probably as high as 0.8 of total stream temperatures. Hence, the nearly linear variation of $\bar{\theta}$ with $\bar{u}/u_e$ for the present data are consistent with the new results of Feller in the limited sense that higher surface temperatures in the settling-chamber and throat regions cause a trend toward the linear variation.

## ESTIMATED VELOCITY FLUCTUATIONS

Estimated values of longitudinal-velocity fluctuations have been made in reference 45 for the data of reference 19 ($M_e \approx 8.5$) and compared with previous measured values for $0 \leq M_e \leq 4.7$. The location of the peak in velocity fluctuations is near the viscous sublayer edge which tended to move away from the wall with increasing Mach number (ref. 45). An attempt has been made to estimate the variation in velocity fluctuations through the present boundary layer and the results are compared with those of reference 45.

The first-order y-momentum equation for axisymmetric turbulent-boundary-layer flow may be expressed as

$$\frac{\partial}{\partial y}\left(\rho \overline{v'^2}\right) - \frac{\cos \beta}{r_w - y \cos \beta} \rho \overline{v'^2} = -\frac{\partial p}{\partial y} - \frac{\rho u^2}{r_c} \tag{16}$$

where $\beta$ is the nozzle contour angle at $x$, and $r_c$ is the radius of curvature of the surface in the x-direction. At a given x-location, equation (16) becomes a linear, ordinary differential equation for the variable $\rho \overline{v'^2}$. Hence, the solution of equation (16) for $\sqrt{\overline{v'^2}}$ is

$$\frac{\sqrt{\overline{v'^2}}}{u_e} = \left\{ -\frac{\rho_e/\rho}{1 - \frac{y}{r_w}\cos \beta} \int_0^{y/\delta} \left(1 - \frac{y}{r_w}\cos \beta\right)\left[\frac{1}{\gamma M_e^2}\frac{\partial}{\partial \frac{y}{\delta}}\left(\frac{p}{p_e}\right) + \frac{\delta}{r_c}\frac{p}{p_e}\left(\frac{M}{M_e}\right)^2\right]d\left(\frac{y}{\delta}\right)\right\}^{1/2} \tag{17}$$

This equation shows that in order to get real values of $\sqrt{\overline{v'^2}}$, $\partial p/\partial y$ would have to be negative over most of the boundary layer since the second term in the integrand is always positive and generally small.

If it is assumed that $\delta/r_c$ and $\delta/r_w$ are very small corresponding to small curvature at the wall, equation (17) reduces to

$$\frac{\sqrt{\overline{v'^2}}}{u_e} = \left(\frac{\dfrac{p_w}{p_e} - \dfrac{p}{p_e}}{\gamma M_e^2 \rho/\rho_e}\right)^{1/2} \tag{18}$$

which shows again that $\partial p/\partial y$ would have to be negative near the wall while elsewhere $p < p_w$.

Equations (17) and (18) were used to compute $\sqrt{\overline{v'^2}}/u_e$ and the results are shown in figure 21. Equation (1) was used for the static-pressure distribution in equations (17) and (18) with $A = 1.0$ and in equation (18) with $A = 0.28$. The values of $\beta$, $\delta/r_c$, and $\delta/r_w$ are given in the figure and were based on the inviscid nozzle-wall coordinates at $x = 2.083$ meters (82 in.). The Mach number and density profiles used were those for condition 2 with $A = 1.0$.

The present results with $A = 1.0$ are roughly similar in trends and levels to the incompressible data of Klebanoff (ref. 56) also shown in figure 21. The curvature terms have very little effect except near the outer edge of the boundary layer. This result indicates that in terms of the boundary-layer coordinate system used in equation (16), the static-pressure variation across the boundary is caused mainly by the turbulent velocity fluctuations normal to the surface. However, in the present tests, finite values of $\partial p/\partial y$ may be imposed upon the boundary layer by the external inviscid-flow field. (See fig. 7.) Hence, the relative contributions of turbulent fluctuations and the inviscid-flow field to the observed static-pressure variation cannot be determined. Any variation in static pressure caused by turbulent fluctuations is enhanced by large stream Mach numbers and large density changes across the layer as indicated by equation (18), and the data comparisons of figure 7(b).

The data of reference 56 indicate that the approximate relation

$$\frac{\sqrt{\overline{u'^2}}}{u_e} \approx \sqrt{2}\,\frac{\sqrt{\overline{v'^2}}}{u_e} \tag{19}$$

is applicable over most of the boundary layer except near the wall in the viscous sublayer region. Values of $\sqrt{\overline{u'^2}}/u_e$ have been obtained by applying the $\sqrt{2}$ factor to the results in figure 21 for finite-curvature values. Another approximate relation for $\sqrt{\overline{u'^2}}$ is based on Prandtl's mixing-length concept:

$$\frac{\sqrt{\overline{u'^2}}}{u_e} = \frac{l}{\delta}\,\frac{\partial(u/u_e)}{\partial(y/\delta)} \tag{20}$$

This relation has also been applied to the present data for $p_o = 4309$ N/cm$^2$ (6250 lb/in.$^2$) with equations (12) and (13) used for $l/\delta$. The velocity-profile derivatives were obtained from the faired line shown in figure 10(a).

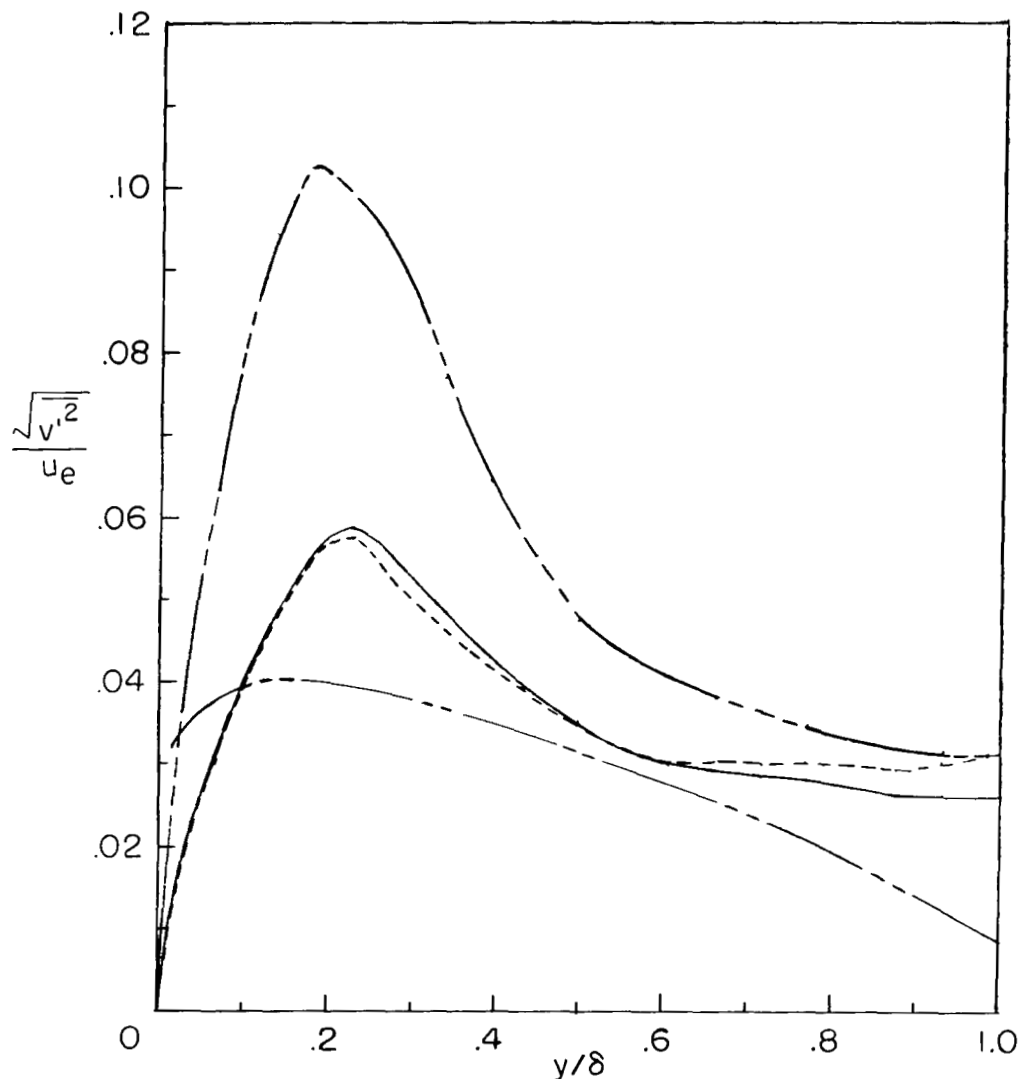| | $M_e$ | $N_{Re,\theta}$ | $\delta/r_w$ | $\delta/r_c$ | Eq. | A | Ref. |
|---|---|---|---|---|---|---|---|
| ———— | 19.42 | $27.2 \times 10^4$ | 0.478 | $1.55 \times 10^{-3}$ | 17 | 1.0 | |
| ———— | 19.42 | 27.2 | 0 | 0 | 18 | 1.0 | Present |
| —·—·— | 19.42 | 27.2 | 0 | 0 | 18 | 0.28 | |
| ——·· | 0 | 8.0 | — | — | — | — | 56 |



Figure 21.— Comparison of estimated normal-velocity fluctuations with data of reference 56. Present results calculated with $\beta = 3.5°$.

The resulting estimated values of $\sqrt{\overline{u'^2}}/u_e$ from equations (19) and (20) are plotted as a function of $y/\delta$ in figure 22. Also shown for comparison in the figure are previous experimental values as presented in reference 45. Again, the present values from equation (19) are roughly similar to previous results while the mixing-length estimates are larger except for $y/\delta > 0.5$. Because of uncertainties in the present mean flow data

| $M_e$ | $N_{Re,\delta}$ | in. $\delta$, (cm) | | Reference |
|---|---|---|---|---|
| —·— ~0 | 5.8 × 10⁵ | 1.05 | ( 2.67) | |
| —·—· .57 | 7.5 × 10⁵ | 2.3 | ( 5.84) | Data presented in reference 45 from other sources |
| —·— {1.72 | 5.0 × 10⁵ | .7 | ( 1.78) | |
| ↓ | ↓ | ↓ | ↓ | |
| 4.67 | 6.1 × 10⁵ | 1.15 | ( 2.92) | |
| {8.25 | 5.37 × 10⁴ | 5.2 | (13.2 ) | |
| ↓ | ↓ | ↓ | ↓ | |
| 8.82 | 10.75 × 10⁴ | 5.9 | (15.0 ) | |
| {19.42 | 2.72 × 10⁵ | 3.7 | ( 9.40) | Present |

Figure 22.- Comparison of present estimates of velocity fluctuations with previous data.

(particularly the static-pressure data), these results for fluctuating velocities are only indicative of possible trends and approximate order of magnitude levels for the present conditions. More reliable estimates for fluctuating quantities will have to be obtained from direct measurements of $\rho'$, $\rho$, and improved measurements of static pressures and other mean flow quantities.

## CONCLUSIONS

Total-temperature, pitot-pressure, and static-pressure measurements were obtained in the boundary layer of a contoured nozzle at Mach 19.5 in nitrogen. The

ratio of wall temperature to settling-chamber temperature was about 0.17; the boundary layer was about 10 centimeters (4 in.) thick, and the Reynolds number based on momentum thickness varied from about 3500 to 4800. A general assessment and review of probe errors encountered in pressure and total-temperature measurements in hypersonic boundary layers is included. Accordingly, the pressure data were corrected for viscous and rarefied flow effects and the temperature data, obtained with a bare-wire thermocouple, were corrected for heat losses by radiation and conduction. The significant conclusions from this investigation were:

1. A static-pressure gradient exists normal to the nozzle wall as indicated by measured static pressures at the wall and in the boundary layer and calculated free-stream pressures. This static-pressure gradient was apparently caused partly by inviscid-flow expansions and partly by fluctuations in the normal-velocity component.

2. Viscous and rarefied flow effects required large corrections to the pitot-pressure measurements as far as 5.1 centimeters (2 in.) from the wall. In general, the trend was to reduce the pitot pressure in the wall region since the rarefied flow effects increased the indicated pitot pressure above continuum values.

3. Estimated values of laminar sublayer thickness and the exponent $N$ in the power-law velocity profile were in good agreement with previous results. The results indicated the sublayer thickness generally increased with increasing Mach number and decreasing momentum-thickness Reynolds number $N_{Re,\theta}$. The exponent $N$ increases with increasing $N_{Re,\theta}$ and is affected only slightly by the ratio of wall temperature to settling-chamber temperature.

4. The relation between the normalized total temperature and velocity was nearly linear over the inner part of the boundary layer as compared with a quadratic relation found in previous nozzle-wall boundary-layer data. This result was attributed to differences in surface or near surface temperatures in the settling-chamber and throat regions of the present nozzle and typical nozzles of previous investigations.

5. Comparisons of the present results in terms of boundary-layer-profile shapes, thickness parameters, and estimated values of skin friction with predictions from finite-difference theories showed that the boundary layer was not laminar. The theoretical results could be brought into reasonable agreement with the data only by suppressing the turbulent flow in the throat region of the nozzle and by using turbulent Prandtl numbers considerably less than unity in the theory. Although these theoretical results may not be unique because of nonlinear interactions between the various options used as inputs, the comparisons indicate that the nozzle boundary layer may have been laminarized in the throat region.

6. Estimates of the intensity of velocity fluctuations in the boundary layer were based on measured values of mean static pressure and also on an assumed mixing-length distribution. These estimates were roughly similar in trends and levels to previous experimental values for incompressible and supersonic flow.

Langley Research Center,
        National Aeronautics and Space Administration,
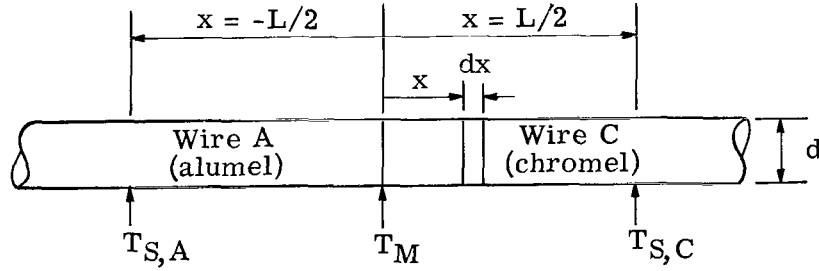                Hampton, Va., March 16, 1971.

# APPENDIX A

## EFFECTS OF HEAT LOSSES BY CONDUCTION AND RADIATION

## ON BARE-WIRE THERMOCOUPLE PROBES

### By Ivan E. Beckwith, William D. Harvey, and Christine M. Darden

### Basic Equations

The notation used in temperature data-reduction procedures for all test runs as reported herein is defined by the following sketch:



Sketch A

where the temperatures $T_{S,A}$, $T_{S,C}$, and $T_M$ (the junction temperature) have, in general, been measured. The heat-balance equation for an element of length $dx$ of the wire is

$$\frac{Ie}{\pi d^2}dx + \frac{N_{Nu,t}k_t}{d^2}(T_{aw} - T)dx = \frac{1}{4}\rho_w\bar{c}\frac{\partial T}{\partial t}dx - \frac{1}{4}\frac{\partial}{\partial x}\left(k_w\frac{\partial T}{\partial x}\right)dx + \frac{\sigma\epsilon}{d}\left(T^4 - \sqrt{\frac{T_a}{T}}T_a^4\right)dx \quad (A1)$$

The simplest way to evaluate the conduction term in this equation is to assume that the temperature distribution along the wire is a quadratic of the form

$$T = A + Bx + Cx^2 \quad (A2)$$

The conditions of continuity in temperature and heat conduction at the junction $(x = 0)$ are then utilized to give the temperature distributions for the alumel and chromel wires, respectively, as

$$T_A = T_M + B_Ax + \frac{4}{L^2}\left(T_{S,A} - T_M + \frac{L}{2}B_A\right)x^2 \quad (A3)$$

$$T_C = T_M + B_AKx + \frac{4}{L^2}\left(T_{S,C} - T_M - \frac{L}{2}KB_A\right)x^2 \quad (A4)$$

74

where

$$B_A = \left(\frac{\partial T_A}{\partial x}\right)_{x=0}$$

and

$$K = \left(\frac{k_A}{k_C}\right)_{x=0}$$

## Application to Probe Corrections

The local total temperature $T_t(= \hat{r}T_{aw})$ is then calculated from equations (A1), (A3), and (A4) by the following procedure:

The conduction term in equation (A1) is first written as

$$\frac{\partial}{\partial x}\left(k_w \frac{\partial T}{\partial x}\right) = k_w \frac{\partial^2 T}{\partial x^2} + \frac{dk_w}{dT}\left(\frac{\partial T}{\partial x}\right)^2$$

Evaluation of equation (A1) at the junction for wires A and C in sketch A then gives the relations

$$\frac{Ie_A}{\pi d^2} + \frac{N_{Nu,t}k_t}{d^2}\left(\hat{r}T_t - T_M\right) = \frac{1}{4}\left(\rho_w \bar{c}\right)_A \frac{dT_M}{dt} - \frac{1}{4}\frac{dk_A}{dT}B_A^2$$

$$- \frac{2k_{A,M}}{L^2}\left(\frac{L}{2}B_A - T_M F_A\right) + \frac{\sigma\epsilon_A}{d}\left(T_M^4 - \sqrt{\frac{T_a}{T_M}}T_a^4\right) \qquad (A5)$$

and

$$\frac{Ie_C}{\pi d^2} + \frac{N_{Nu,t}k_t}{d^2}\left(\hat{r}T_t - T_M\right) = \frac{1}{4}\left(\rho_w \bar{c}\right)_C \frac{dT_M}{dt} - \frac{1}{4}\frac{dk_C}{dT}K^2 B_A^2$$

$$+ \frac{2k_{C,M}}{L^2}\left(K\frac{L}{2}B_A + T_M F_C\right) + \frac{\sigma\epsilon_C}{d}\left(T_M^4 - \sqrt{\frac{T_a}{T_M}}T_a^4\right) \qquad (A6)$$

where

$$F_A = 1 - \frac{T_{S,A}}{T_M}$$

$$F_C = 1 - \frac{T_{S,C}}{T_M}$$

Subtraction of equation (A5) from equation (A6) then gives a quadratic equation for $B_A$ which is

$$\frac{I}{\pi d^2}\left(e_C - e_A\right) = \frac{1}{4}\left(\rho_C \bar{c}_C - \rho_A \bar{c}_A\right)\frac{dT_M}{dt} + 2\,\frac{k_{A,M}}{L}\,B_A + \frac{1}{4}\left(\frac{dk_A}{dT} - K^2\,\frac{dk_C}{dT}\right)B_A^{\,2}$$

$$+ \frac{2T_M}{L^2}\left(k_{C,M}F_C - k_{A,M}F_A\right) + \frac{\sigma}{d}\left(\epsilon_C - \epsilon_A\right)\left(T_M^{\,4} - \sqrt{\frac{T_a}{T_M}}\,T_a^{\,4}\right) \qquad (A7)$$

This equation is solved for $B_A$ as a function of the measured junction temperature $T_M$ and the measured end temperatures $T_{S,A}$ and $T_{S,C}$ which are shown in figure 23 in the form of the variables $T_S/T_M$ and $T_M/T_0$. These data were obtained with the probe shown schematically in the figure. This probe is the same size and shape as the boundary-layer probe shown in figure 1 but with 0.076-millimeter-diameter (0.003-in.) wires attached, as indicated, to obtain the end temperatures. The faired curves in figure 23 for $F_A$ and $F_C$ have been used herein for the reduction of boundary-layer survey data. All of these present data were obtained without electric heating and for time-steady conditions, so the terms containing $I$ and $dT_M/dt$ in equations (A5) to (A7) were zero. The values for thermal conductivity of alumel and chromel were taken from the faired lines shown in figure 24 (from data in ref. 57). Shown for comparison in this figure are the values of thermal conductivity of similar "type K" thermocouple wires from reference 58. The emissivity difference $\left(\epsilon_C - \epsilon_A\right)$ in equation (A7) is taken from faired curves of measured emissivity as discussed in appendix B where it is shown that the emissivity of chromel $\epsilon_C$ tends to increase more than $\epsilon_A$ after similar exposure to high-temperature nitrogen.

The values of $B_A$ obtained from equation (A7) are substituted into equation (A5) which is solved for $T_t$ by using data for $\hat{r}$ and $N_{Nu,t}$ as given in reference 59. These data apply only up to about Mach 5; however, preliminary measurements of the transient heating rates of typical boundary-layer probes during the present investigation indicate that the $N_{Nu,t}$ curve of reference 59 for Mach 5 is still applicable at Mach 19. Since the emissivity of both alumel and chromel does depend on the surface condition of the wires, it is first necessary to determine a reference emissivity for each test. This value is obtained by solving equation (A5) for $\epsilon_A$ with all measured quantities at $y = \delta$ used and with $T_t = T_{t,e}$ required. The resulting value of emissivity, termed $\epsilon_{A,e}$, is used to construct an effective emissivity curve for the remaining data from that particular run. (For details of this procedure and the effective emissivity curves used, see appendix B.)

To obtain $T_t/T_{t,e}$ from equation (A5), an iterative procedure was required, since $N_{Nu,t}$ and $\hat{r}$ are functions of local Reynolds number, Mach number, and Knudsen number (ref. 59). Since large corrections to the local Mach number were required due to the
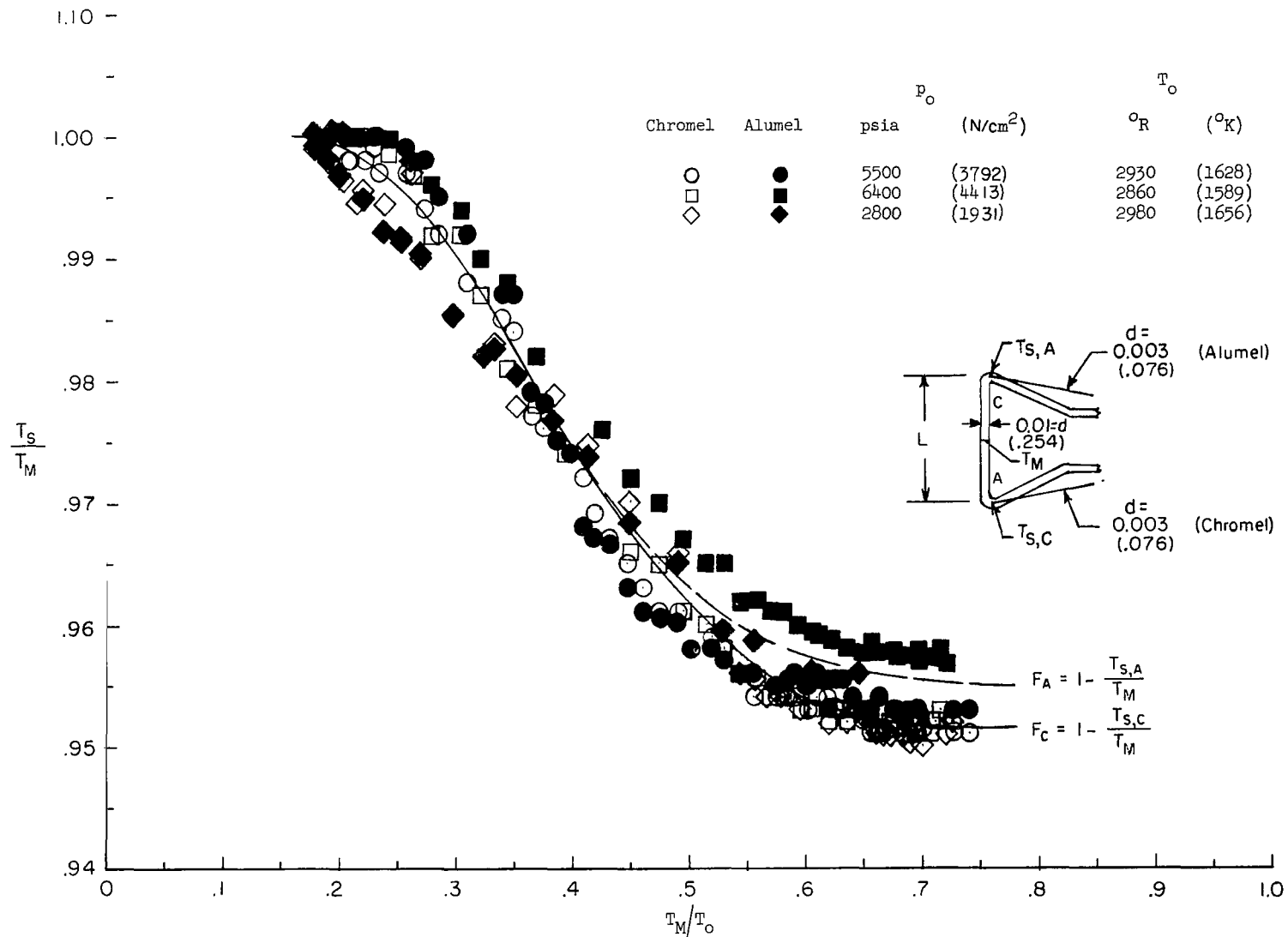
Figure 23.- Variation of ratio of end temperature to junction temperature with junction temperature. Linear dimensions in inches (parenthetically in millimeters).

rarefied flow effects (see fig. 3 and discussion in text), a double iteration cycle was used to obtain the final corrected pitot pressures and total temperature. The accuracy criteria used in the iteration procedure was that the percentage change with successive iterations was less than 1 percent on $N_{Re,1}$ and less than 0.5 percent on total temperature.
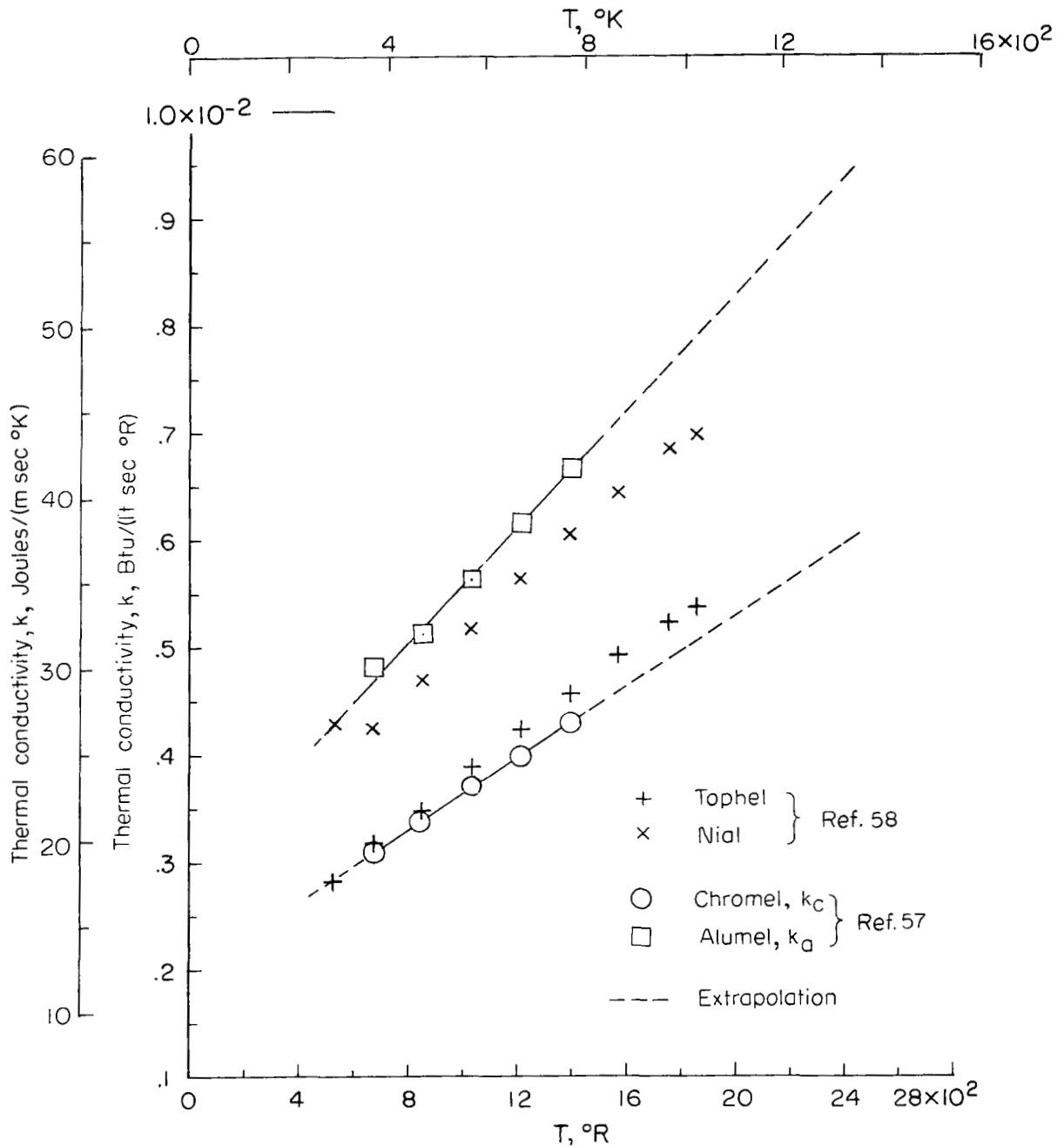


Figure 24.- Thermal conductivity of chromel and alumel thermocouple wire and comparison with other "type K" wires.

# APPENDIX B

## MEASUREMENTS OF HEMISPHERICAL EMISSIVITY FOR

## CHROMEL AND ALUMEL WIRES

By William D. Harvey, Lemuel E. Forrest,
and Frank L. Clark

The use of thermocouple probes for surveying hypersonic flow fields over test models or tunnel wall boundary layers poses problems of compromise among such factors as ability to withstand high-temperature and high-velocity conditions, conduction and radiation errors, recovery characteristics, and often the time response of a probe. Usually, a thermocouple material can be selected and a probe designed and constructed to properly account for most of these factors. However, radiant-heat-transfer losses from a thermocouple probe become especially important at elevated temperatures, and corrections due to radiation must be accurately calculated.

Usually, sufficient data are available on the normal emissivity for individual base metal thermocouple wires at low temperatures (see, for example, refs. 60 and 61). However, limited definitive data are available on total hemispherical emissivity for selected thermocouple wires at high temperatures with the exception of some results presented in references 61, 62, and 63. The indiscriminate substitution of the normal emissivity for total hemispherical emissivity in heat-transfer problems could lead to serious errors (paper no. 31, ref. 61).

The purpose of this appendix is to present data on the total hemispherical emissivity for chromel and alumel thermocouple wires over a wide temperature range. These results have been utilized to calculate the radiation and conduction corrections by the method of appendix A for all data presented herein.

The effective hemispherical emissivity $\epsilon$ of an exposed thermocouple wire of length $L$ and diameter $d$ was experimentally determined by electrically heating the wire in an evacuated chamber and calculating the emissivity by use of equation (A5) or equation (A6) of appendix A.

## Apparatus and Procedure

All chromel and alumel wires used in the present tests to determine the emissivity were 0.508 millimeter (0.020 in.) in diameter. In order to minimize conduction losses a large overall length-to-diameter ratio of $L/d = 525$ was used. A schematic of the wires and circuit used is shown in figure 25. A block diagram is included in this figure indicating the equipment used and method of data readout. Figure 25(a) shows the alumel
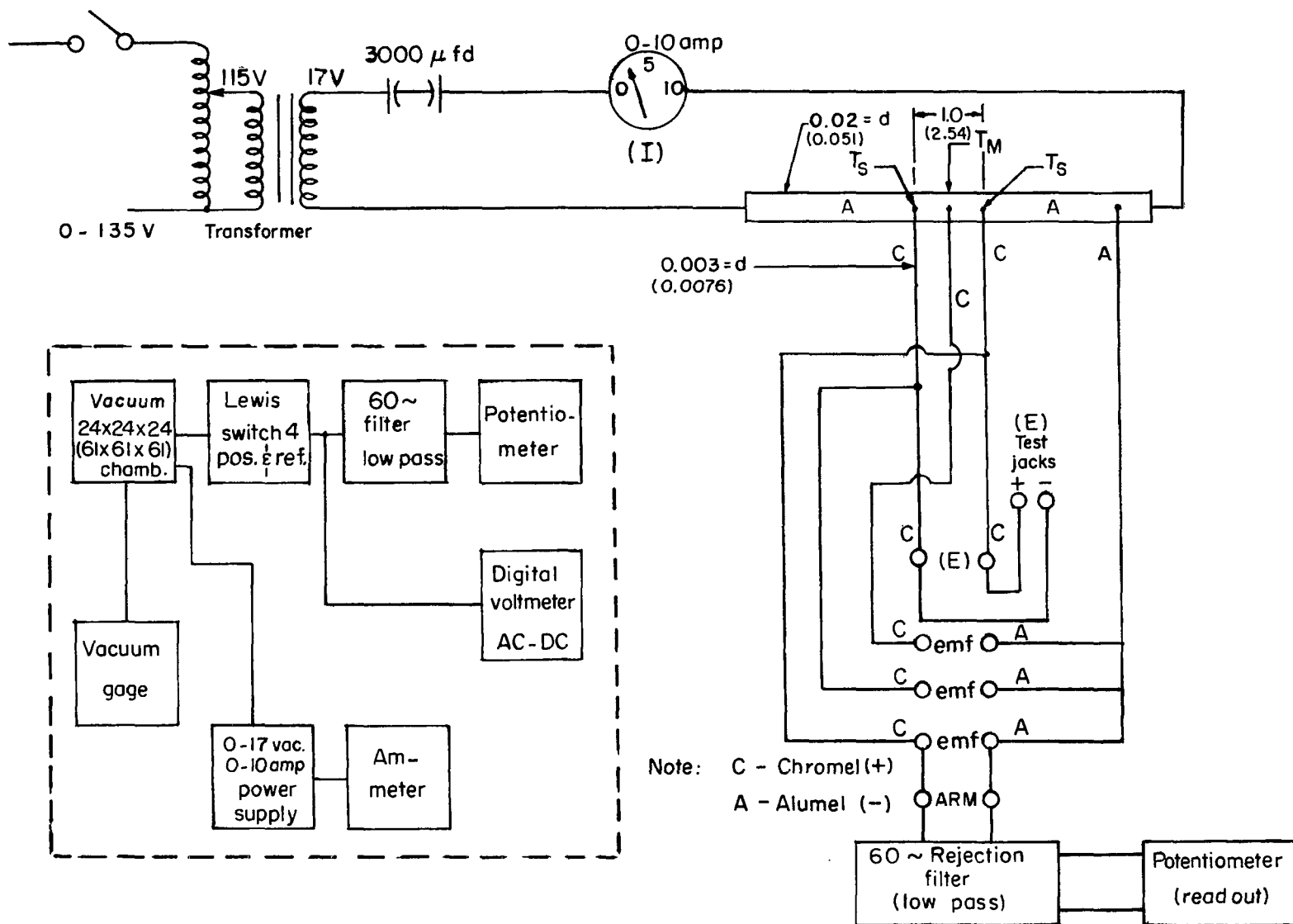
(a) Heating circuit and readout apparatus.

Figure 25.- Emissivity apparatus circuit. Dimensions are in inches (parenthetically in centimeters).
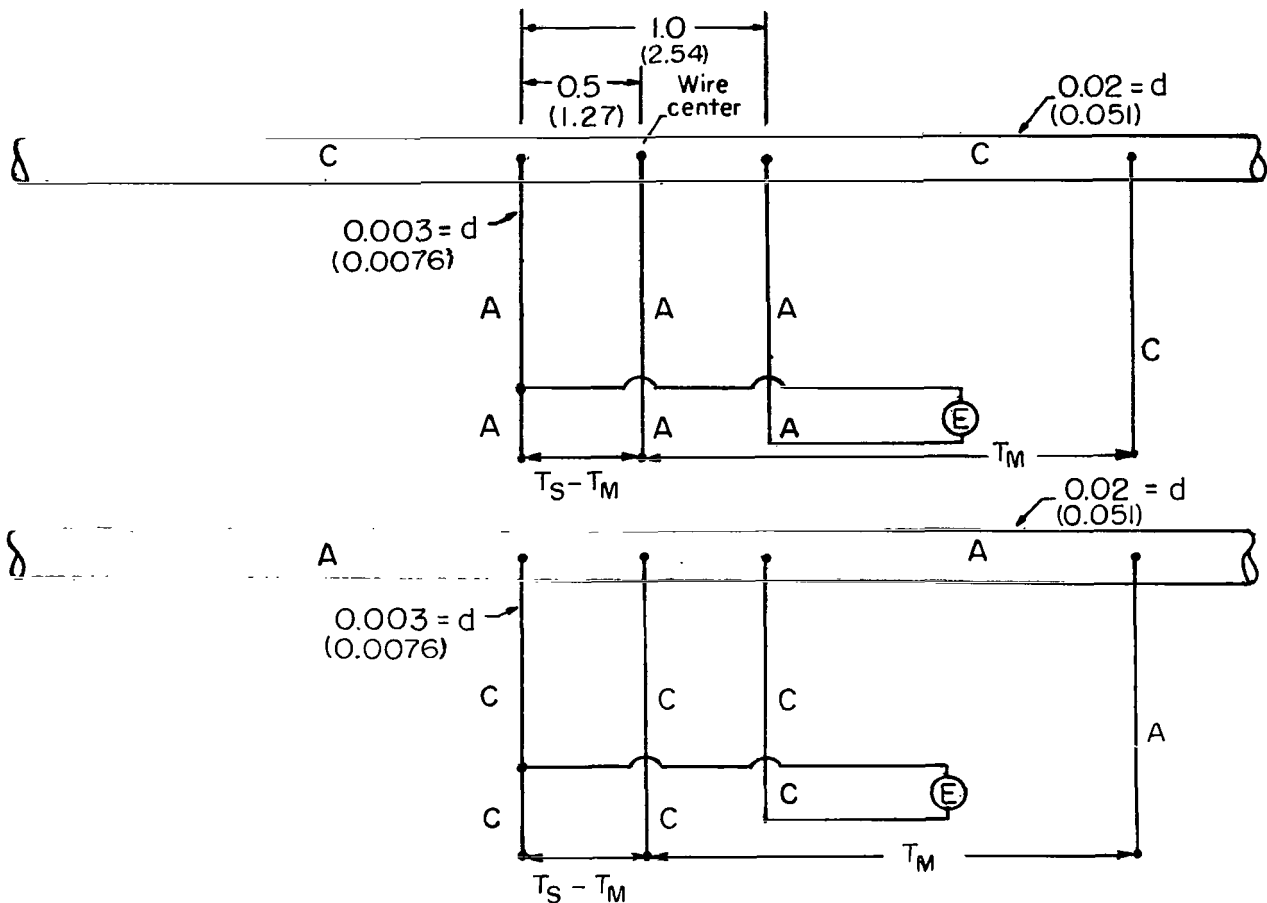
(b) Individual chromel or alumel wires. All dimensions in inches (parenthetically in centimeters).

Figure 25.- Concluded.

wire in place while figure 25(b) indicates the individual circuit (less the heating circuit and readout equipment) for the chromel and alumel wires.

All junctions of the chromel-alumel wires were formed by resistance butt welding. There was no "bead" formed when the junction was butt welded. The test wire was freely suspended between supporting posts 0.27 meter (10.5 in.) apart. Chromel and alumel wires of 0.0762-millimeter (0.003-in.) diameter were attached 1.27 centimeters (0.5 in.) on either side of the test-section center wire to allow evaluation of heat conduction effects from equations (A5) to (A7) where $N_{Nu,t} = 0$, $dT_M/dt = 0$, and $B_A = 0$ for these tests. The results indicated that heat conduction effects could be neglected in the present emissivity measurements.

The testing was done in a 0.61-meter (2-ft) square, steel, vacuum chamber which was evacuated to pressures of about 1.333 $N/m^2$ (10 microns of mercury) maximum.

The test wire was electrically heated and measurements were taken of the voltage drop $E$ across the central 2.54-centimeter (1-in.) test portion. A 60-cycle alternating current was used to heat the wire and this current $I$ was measured with a calibrated ammeter.

The thermal electromotive force of the junction at the center of the test section relative to the ambient temperature was measured with a manually balanced precision potentiometer. The potentiometer was isolated from the 60-cycle current by a low-pass filter. A back-to-back arrangement of electrolytic capacitors was used to prevent short circuiting of the thermal electromotive force by the secondary winding of the power transformer. Effectiveness of the circuit was verified by observing that no direct-current potential difference existed across a shunt in series with the transformer windings.

## Tests and Results

In tunnel tests, the survey temperature probes are exposed continuously to the test gas flow and over a period of time become "aged," that is, changes in the surface condition of the thermocouple wires occur. It has been found and discussed in reference 58, for example, that both chromel and alumel wires are subject to oxidation in air above about 1144 K (2060° R) but are still more resistant to oxidation than other commonly used conventional base-metal thermocouples. However, as found in the present test program to measure emissivity and as mentioned in reference 58, reducing conditions (that is, a test environment which has not been purged with high purity nitrogen prior to evacuation) have adverse effects and the chromel wire goes through a change in a surface condition called "green rot." Under this oxidizing condition, the chromel wire is oxidized to a much greater extent than the alumel wire.

It was observed in the present tests that the chromel wire did darken with increasing exposure time and temperature level when the test chamber was not purged with a high purity nitrogen gas. The alumel wire did not darken as much as the chromel wire. The present results referred to as "oxidized" have been obtained by subjecting the wires to various indicated temperature levels for fairly long time intervals under a nonpurged vacuum system. A new wire could be kept "bright" by purging the vacuum chamber with high purity nitrogen gas prior to each test. The nitrogen gas used for purging contained less than 5 parts per million of oxygen and is the same gas used in the tunnel (ref. 30).

The total hemispherical emissivity for bright and oxidized chromel and alumel wires is shown in figure 26 for successive runs on each wire. The present data are compared with available values for normal emissivity (ref. 64). The present results indicate increasing emissivity with temperature for both the chromel and alumel wires and the magnitude of emissivity is considerably greater for the oxidized wires than for the bright wires. The present data are generally somewhat different from previous values for normal emissivity.
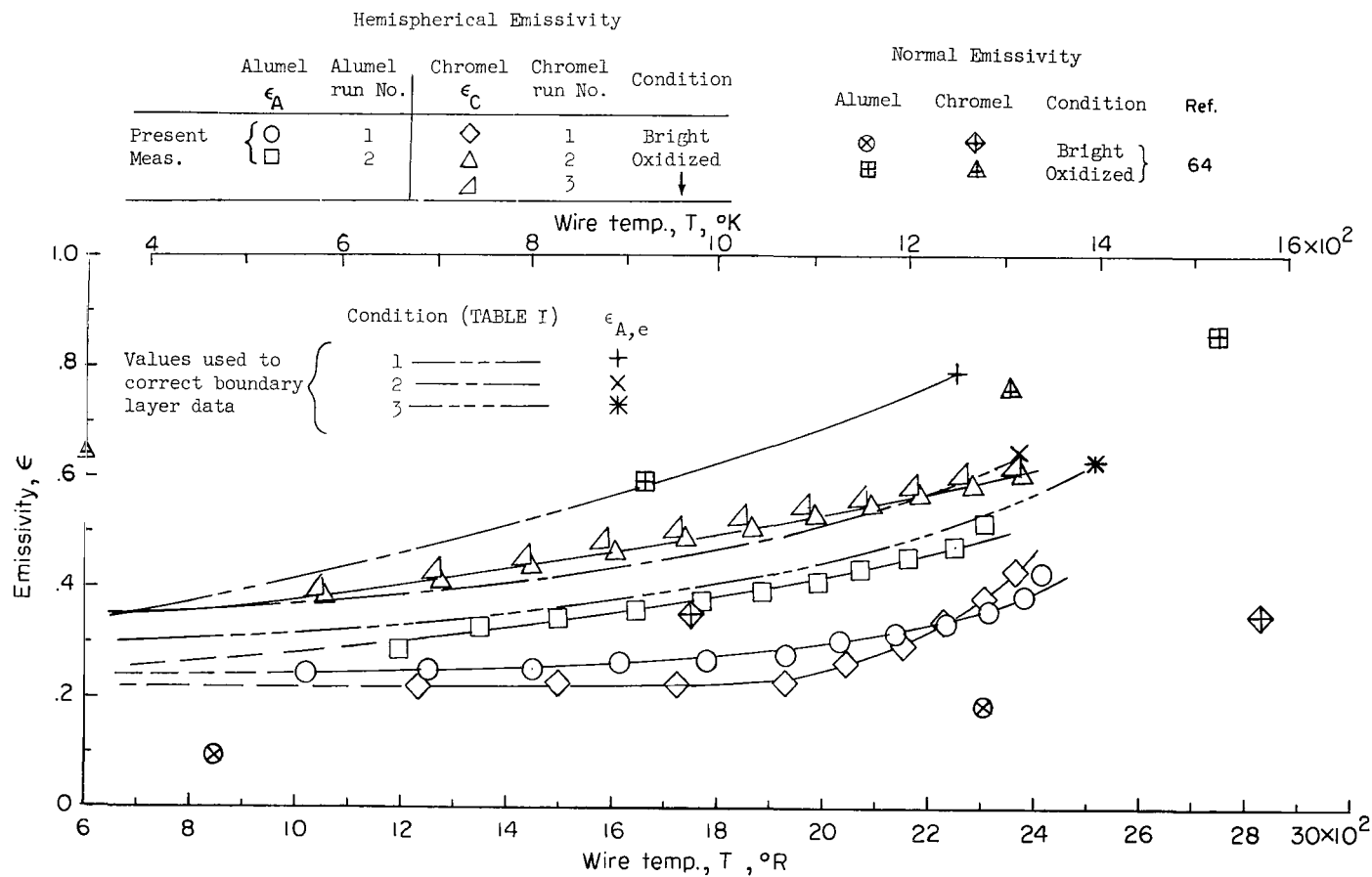
Figure 26.- Emissivity for bright and for oxidized chromel and alumel wires.

The results shown in figure 26 have been utilized in the data-reduction procedure to correct the total-temperature probe for radiation losses according to the method of appendix A. The difference $\left(\epsilon_C - \epsilon_A\right)$ has been assumed invariant with wire exposure for the oxidized condition and the present results indicate that this assumption is valid.

The dashed line curves in figure 26 were used for the values of $\epsilon_A$ required in the data-reduction procedure of appendix A. These curves are extrapolations to lower temperatures of the emissivity $\epsilon_{A,e}$ at the edge of the boundary layer as determined from equation (A5) with the required condition that $T_t = T_{t,e}$ at $y = \delta$.

# REFERENCES

1. Kline, S. J.; Morkovin, M. V.; Sovran, G.; and Cockrell, D. J.; eds.: Computation of Turbulent Boundary Layers — 1968 AFOSR-IFP-Standard Conference. Vol. I — Methods, Predictions, Evaluation and Flow Structure. Stanford Univ., c.1969.

2. Cebeci, Tuncer; Smith, A. M. O.; and Wang, L. C.: A Finite-Difference Method for Calculating Compressible Laminar and Turbulent Boundary Layers. Pt. I. Rep. No. DAC-67131, McDonnell Douglas Aircraft Co., Inc., Mar. 1969.

3. Bradshaw, P.; and Ferriss, D. H.: Calculation of Boundary-Layer Development Using the Turbulent Energy Equation. II — Compressible Flow on Adiabatic Walls. NPL Aero Rep. 1217, Brit. A.R.C., Nov. 24, 1966.

4. Herring, H. James; and Mellor, George L.: A Method of Calculating Compressible Turbulent Boundary Layers. NASA CR-1144, 1968.

5. Bushnell, Dennis M.; and Beckwith, Ivan E.: Calculation of Nonequilibrium Hypersonic Turbulent Boundary Layers and Comparisons With Experimental Data. AIAA J., vol. 8, no. 8, Aug. 1970, pp. 1462-1469.

6. Beckwith, Ivan E.: Recent Advances in Research on Compressible Turbulent Boundary Layers. Analytic Methods in Aircraft Aerodynamics, NASA SP-228, 1970, pp. 355-416.

7. Coles, D. E.: The Turbulent Boundary Layer in a Compressible Fluid. R-403-PR (Contract No. AF 49(638)-700), RAND Corp., Sept. 1962. (Available from DDC as AD 285 651.)

8. Baronti, Paolo O.; and Libby, Paul A.: Velocity Profiles in Turbulent Compressible Boundary Layers. AIAA J., vol. 4, no. 2, Feb. 1966, pp. 193-202.

9. Matting, Fred W.; Chapman, Dean R.; Nyholm, Jack R.; and Thomas, Andrew G.: Turbulent Skin Friction at High Mach Numbers and Reynolds Numbers in Air and Helium. NASA TR R-82, 1961.

10. Adcock, Jerry B.; Peterson, John B., Jr.; and McRee, Donald I.: Experimental Investigation of a Turbulent Boundary Layer at Mach 6, High Reynolds Numbers, and Zero Heat Transfer. NASA TN D-2907, 1965.

11. Fischer, Michael C.; Maddalon, Dal V.; Weinstein, Leonard M.; and Wagner, Richard D., Jr.: Boundary-Layer Surveys on a Nozzle Wall at $M_\infty \approx 20$ Including Hot-Wire Fluctuation Measurements. AIAA Pap. No. 70-746, June-July 1970.

12. Perry, J. H.; and East, R. A.: Experimental Measurements of Cold Wall Turbulent Hypersonic Boundary Layers. A.A.S.U. Rep. No. 275, Univ. of Southampton, Feb. 1968.

13. Kemp, Joseph H., Jr.; and Owen, F. K.: Nozzle Wall Boundary Layers at Mach Numbers 20 to 47. AIAA Paper No. 71-161, Jan. 1971.

14. Scaggs, Norman E.: Boundary Layer Profile Measurements in Hypersonic Nozzles. ARL 66-0141, U.S. Air Force, July 1966.

15. Shall, Paul Joseph, Jr.: A Boundary Layer Study on Hypersonic Nozzles. M.S. Thesis, U.S. Air Force Inst. Technol., Mar. 1968. (Available from DDC as AD 833 236.)

16. Kemp, Joseph H., Jr.; and Sreekanth, A. K.: Preliminary Results From an Experimental Investigation of Nozzle Wall Boundary Layers at Mach Numbers Ranging From 27 to 47. AIAA Pap. No. 69-686, June 1969.

17. Burke, Andrew F.: Turbulent Boundary Layers on Highly Cooled Surfaces at High Mach Numbers. Proceedings of Symposium on Aerothermoelasticity. ASD Tech. Rep. 61-645, U.S. Air Force, 1961, pp. 704-741.

18. Wallace, J. E.: Hypersonic Turbulent Boundary-Layer Studies at Cold Wall Conditions. Proceedings of the 1967 Heat Transfer and Fluid Mechanics Institute, Paul A. Libby, Daniel B. Olfe, and Charles W. Van Atta, eds., Stanford Univ. Press, c.1967, pp. 427-451.

19. Wallace, J. E.: Hypersonic Turbulent Boundary Layer Measurements Using an Electron Beam. CAL Rep. No. AN-2112-Y-1 (Contract No. NSR33-009-029), Cornell Aeronaut. Lab., Inc., Aug. 1968.

20. Banner, L. T.; and Williams, M. J.: Boundary Layer Measurements in the A.R.L. Hypersonic Tunnel Conical Nozzle. Note ARL/Aero. 215, Aust. Def. Sci. Serv., July 1963.

21. Hill, F. K.: Turbulent Boundary Layer Measurements at Mach Numbers From 8 to 10. Phys. Fluids, vol. 2, no. 6, Nov.-Dec. 1959, pp. 668-680.

22. Neal, Luther, Jr.: A Study of the Pressure, Heat Transfer, and Skin Friction on Sharp and Blunt Flat Plates at Mach 6.8. NASA TN D-3312, 1966.

23. Danberg, James E.: Characteristics of the Turbulent Boundary Layer With Heat and Mass Transfer: Data Tabulation. NOLTR-67-6, U.S. Navy, Jan. 23, 1967. (Available from DDC as AD 650 272.)

24. Samuels, Richard D.; Peterson, John B., Jr.; and Adcock, Jerry B.: Experimental Investigation of the Turbulent Boundary Layer at a Mach Number of 6 With Heat Transfer at High Reynolds Numbers. NASA TN D-3858, 1967.

25. Lobb, R. Kenneth; Winkler, Eva M.; and Persh, Jerome: Experimental Investigation of Turbulent Boundary Layers in Hypersonic Flow. J. Aeronaut. Sci., vol. 22, no. 1, Jan. 1955, pp. 1-10.

26. Bertram, Mitchel H.; and Neal, Luther, Jr.: Recent Experiments in Hypersonic Turbulent Boundary Layers. Presented at the AGARD Specialists' Meeting on Recent Developments in Boundary-Layer Research (Naples, Italy), May 10-14, 1965.

27. Watson, Ralph D.; and Cary, A. M., Jr.: The Transformation of Hypersonic Turbulent Boundary Layers to Incompressible Form. AIAA J. (Tech. Notes), vol. 6, no. 6, June 1967, pp. 1202-1203.

28. Jones, Robert A.; and Feller, William V.: Preliminary Surveys of the Wall Boundary Layer in a Mach 6 Axisymmetric Tunnel. NASA TN D-5620, 1970.

29. Wagner, R. D., Jr.; Maddalon, D. V.; Weinstein, L. M.; and Henderson, A., Jr.: Influence of Measured Free-Stream Disturbances on Hypersonic Boundary-Layer Transition. Paper presented at the AIAA Second Fluid Plasma Dynamics Conference (San Francisco, Calif.), June 1969.

30. Clark, Frank L.; Ellison, James C.; and Johnson, Charles B.: Recent Work in Flow Evaluation and Techniques of Operations for the Langley Hypersonic Nitrogen Facility. NASA paper presented at Fifth Hypervelocity Techniques Symposium (Denver, Colo.), Mar. 28-30, 1967.

31. Clark, Frank L.; and Johnson, Charles B.: Real-Gas Hypersonic-Nozzle Flow Parameters for Nitrogen in Thermodynamic Equilibrium. NASA TN D-2019, 1963.

32. Ahtye, Warren F.; and Peng, Tzy-Cheng: Approximations for the Thermodynamic and Transport Properties of High-Temperature Nitrogen With Shock-Tube Applications. NASA TN D-1303, 1962.

33. McCroskey, William J.: An Experimental Model for the Sharp Leading Edge Problem in Rarefied Hypersonic Flow. ARL 66-0101, U.S. Air Force, June 1966. (Available from DDC as AD 641 996.)

34. Morkovin, M. V.; and Bradfield, W. S.: Probe Interference in Measurements in Supersonic Laminar Boundary Layers. J. Aeronaut. Sci. (Readers' Forum), vol. 21, no. 11, Nov. 1954, p. 785.

35. Bradfield, W. S.: Research on Laminar and Turbulent Boundary Layers at Super- sonic Speeds — Final Summary Report. Res. Rep. No. 131 (AFOSR TR-57-64, AD No. 136 559), Inst. Technol., Dep. Aeronaut. Eng., Univ. of Minnesota, Dec. 1957.

36. Arney, G. D., Jr.; and Bailey, A. B.: Addendum to an Investigation of the Equilibrium Pressure Along Unequally Heated Tubes. AEDC-TDR-62-188, U.S. Air Force, Oct. 1962.

37. Sherman, F. S.: New Experiments on Impact-Pressure Interpretation in Supersonic and Subsonic Rarefied Air Streams. NACA TN 2995, 1953.

38. Kosterin, S. I.; Yushchenkova, N. I.; Belova, N. T.; and Kamaev, B. D.: An Investiga- tion Into the Effect of the Rarefaction of a Supersonic Stream on the Readings of a Total-Head Probe. Int. Chem. Eng., vol. 3, no. 2, Apr. 1963, pp. 251-255.

39. Enkenhus, K. R.: Pressure Probes at Very Low Density. Rep. No. 43, Univ. of Toronto, Institute of Aerophysics, UTIA Rep. 43, Jan. 1957.

40. White, Richard B.: Hypersonic Viscous-Interaction and Rarefaction Effects on Impact Probes. AIAA Stud. J., vol. 5, no. 2, Apr. 1967, pp. 46-49.

41. Daum, F. L.; Shang, J. S.; and Elliott, G. A.: Impact Pressure Behavior in Rarefied Hypersonic Flow. AIAA J., vol. 3, no. 8, Aug. 1965, pp. 1546-1548.

42. Pollard, M. G.: Interpretation of Impact Pressures in Rarefied Gas Flows. Rarefied Gas Dynamics, Vol. I, Leon Trilling and Harold Y. Wachman, eds., Academic Press, Inc., 1969, pp. 811-834.

43. Chang, J. H.; and Fenn, J. B.: Viscous Effects on Impact Pressure Measure- ments in Low Density Flows at High Mach Numbers. Project SQUID Tech. Rep. RP-115-PU, Purdue Univ., 1968.

44. Emmons, Howard W., ed.: Fundamentals of Gas Dynamics. Princeton Univ. Press, 1958.

45. Harvey, William D.; Bushnell, Dennis M.; and Beckwith, Ivan E.: Fluctuating Prop- erties of Turbulent Boundary Layers for Mach Numbers up to 9. NASA TN D-5496, 1969.

46. Chomiak, J.: On the Limit Accuracy of Measurement of the Mean Total Pressure in a Pulsating Flow. Fluid Dyn. Trans., vol. 4, 1969, pp. 703-706.

47. Bushnell, Dennis M.; Johnson, Charles B.; Harvey, William D.; and Feller, William V.: Comparison of Prediction Methods and Studies of Relaxation in Hypersonic Turbu- lent Nozzle-Wall Boundary Layers. NASA TN D-5433, 1969.

48. Johnson, Charles B.; Boney, Lillian R.; Ellison, James C.; and Erickson, Wayne D.: Real-Bas Effects on Hypersonic Nozzle Contours With a Method of Calculation. NASA TN D-1622, 1963.

49. Edenfield, E. E.: Contoured Nozzle Design and Evaluation for Hotshot Wind Tunnels. AIAA Pap. No. 68-369, Apr. 1968.

50. Bertram, Mitchel H.; and Blackstock, Thomas A.: Some Simple Solutions to the Problem of Predicting Boundary-Layer Self-Induced Pressures. NASA TN D-798, 1961.

51. Behrens, Wilhelm: Viscous Interaction Effects on a Static Pressure Probe at $M = 6$. AIAA J., vol. 1, no. 12, Dec. 1963, pp. 2864-2866.

52. Harris, Julius Elmore: Numerical Solution of the Compressible Laminar, Transitional, and Turbulent Boundary Layer Equations With Comparisons to Experimental Data. Ph. D. Thesis, Virginia Polytech. Inst., May 1970.

53. Cebeci, Tuncer; Smith, A. M. O.; and Mosinskis, G.: Calculation of Compressible Adiabatic Turbulent Boundary Layers. AIAA Pap. No. 69-687, June 1969.

54. Back, L. H.; Cuffel, R. F.; and Massier, P. F.: Laminarization of a Turbulent Boundary Layer in Nozzle Flow — Boundary Layer and Heat Transfer Measurements with Wall Cooling. Pap. No. 69-HT-56, Amer. Soc. Mech. Eng., Aug. 1969.

55. Johnson, Charles B.; and Bushnell, Dennis M.: Power-Law Velocity-Profile-Exponent Variations With Reynolds Number, Wall Cooling, and Mach Number in a Turbulent Boundary Layer. NASA TN D-5753, 1970.

56. Klebanoff, P. S.: Characteristics of Turbulence in a Boundary Layer With Zero Pressure Gradient. NACA Rep. 1247, 1955. (Supersedes NACA TN 3178.)

57. Chromel-Alumel Thermocouple Alloys. Catalog M-61 C-A 5M S.P. 9-62, Hoskins Manufacturing Co., c.1961.

58. Caldwell, F. R.: Thermocouple Materials. NBS Monogr. 40, Nat. Bur. Stand., Mar. 1962.

59. Yanta, William J.: A Hot-Wire Stagnation Temperature Probe. NOLTR 68-60, U.S. Navy, June 18, 1968.

60. Glawe, George E.; and Shepard, Charles E.: Some Effects of Exposure to Exhaust-Gas Streams on Emittance and Thermoelectric Power of Bare-Wire Platinum Rhodium — Platinum Thermocouples. NACA TN 3253, 1954.

61. Richmond, Joseph C., ed.: Measurement of Thermal Radiation Properties of Solids. NASA SP-31, 1963.

62. McQuillan, M. K.: Some Observations on the Behaviour of Platinum-Platinum/ Rhodium Thermocouples at High Temperatures. J. Sci. Instrum., vol. 26, Oct. 1949, pp. 329-331.

63. Scadron, Marvin D.; and Warshawsky, Isidore: Experimental Determination of Time Constants and Nusselt Numbers for Bare-Wire Thermocouples in High-Velocity Air Streams and Analytic Approximation of Conduction and Radiation Errors. NACA TN 2599, 1952.

64. Hodgman, Charles D.; Weast, Robert C.; and Selby, Samuel M.; eds.: Handbook of Chemistry and Physics. Thirty-eighth ed., Chem. Rubber Pub. Co., 1956-1957.

*"The aeronautical and space activities of the United States shall be conducted so as to contribute . . . to the expansion of human knowledge of phenomena in the atmosphere and space. The Administration shall provide for the widest practicable and appropriate dissemination of information concerning its activities and the results thereof."*

— NATIONAL AERONAUTICS AND SPACE ACT OF 1958

# NASA SCIENTIFIC AND TECHNICAL PUBLICATIONS

**TECHNICAL REPORTS**: Scientific and technical information considered important, complete, and a lasting contribution to existing knowledge.

**TECHNICAL NOTES**: Information less broad in scope but nevertheless of importance as a contribution to existing knowledge.

**TECHNICAL MEMORANDUMS**: Information receiving limited distribution because of preliminary data, security classification, or other reasons.

**CONTRACTOR REPORTS**: Scientific and technical information generated under a NASA contract or grant and considered an important contribution to existing knowledge.

**TECHNICAL TRANSLATIONS**: Information published in a foreign language considered to merit NASA distribution in English.

**SPECIAL PUBLICATIONS**: Information derived from or of value to NASA activities. Publications include conference proceedings, monographs, data compilations, handbooks, sourcebooks, and special bibliographies.

**TECHNOLOGY UTILIZATION PUBLICATIONS**: Information on technology used by NASA that may be of particular interest in commercial and other non-aerospace applications. Publications include Tech Briefs, Technology Utilization Reports and Technology Surveys.

*Details on the availability of these publications may be obtained from:*

## SCIENTIFIC AND TECHNICAL INFORMATION OFFICE

# NATIONAL AERONAUTICS AND SPACE ADMINISTRATION
Washington, D.C. 20546